A Eurasian Pattern of Northern Hemisphere Wintertime Sea Level Pressure Variability

Brian V. Smoliak

A thesis submitted in partial fulfillment of
the requirements for the degree of

Master of Science

University of Washington

2009

Program Authorized to Offer Degree: Atmospheric Sciences

University of Washington
Graduate School

This is to certify that I have examined this copy of a master's thesis by

Brian V. Smoliak

and have found that it is complete and satisfactory in all respects,
and that any and all revisions required by the final
examining committee have been made.

Committee Members:

_____
John M. Wallace

_____
Dennis L. Hartmann

_____
Gerard H. Roe

Date: _____

University of Washington

Abstract

A Eurasian Pattern of Northern Hemisphere
Wintertime Sea Level Pressure Variability

Brian V. Smoliak

Chair of the Supervisory Committee:
Professor John M. Wallace
Atmospheric Sciences

The dominant pattern of Eurasian monthly-mean wintertime (DJFM) sea level pressure (SLP) variability is characterized by a single, broad center of action over northwestern Russia that extends eastward to the Pacific coastline. Results of empirical orthogonal function (EOF) analysis, rotated EOF analysis, and empirical orthogonal teleconnection (EOT) analysis define the pattern as the third leading pattern of Northern Hemisphere (NH) wintertime SLP variability, explaining approximately 10% of hemispheric SLP variance. The robust Eurasian pattern is exemplified by EOT3 of NH SLP. This preferred circulation pattern is examined based on 50 years of monthly-mean wintertime fields from the NCEP-NCAR reanalyses and additional datasets.

Linear regression and compositing techniques are used in conjunction with the standardized expansion coefficient time series associated with EOT3 of SLP to investigate its signature in other climatological fields, how the pattern relates to climatological mean features, and the impacts of variability associated with the pattern on timescales of days to months. The pattern's positive polarity is associated with a westward expansion of the Siberian High, anomalously cold temperatures over northern Eurasia, and decreased storminess across the continent. The pattern's negative polarity is characterized by a contracted and weakened Siberian High, with enhanced zonal flow prevailing over most of Eurasia poleward of the Himalayas. This is accompanied by warm surface air temperature anomalies across the

northern tier of the continent and increased precipitation over western Siberia.

The Eurasian pattern is most extensive during wintertime, but exhibits two peaks in the fraction of SLP variance it explains, one in autumn and one in spring. During autumn, it is the leading pattern of NH SLP variability.

Wintertime pentad-mean data are utilized to document the variability of the pattern on shorter timescales. The appearance of a Rossby wave-breaking signature in composites of strong positive events indicate an association with blocking of the upper tropospheric zonal flow over northwest Russia. Positive skewness is also found to be a characteristic of the Eurasian pattern, evidence of a preference for stronger positive anomalies than negative anomalies over its center of action.

TABLE OF CONTENTS

LIST OF FIGURES

LIST OF TABLES

ACKNOWLEDGMENTS

The pages herein represent the portion of my educational journey stretching from matriculation at the University of Washington to the decision to continue toward a Ph.D. in atmospheric sciences. As I come to another branch in the trail, I would be remiss not pause to acknowledge the individuals that marked my path thus far.

I cannot properly express my gratitude and respect for my advisor, Mike Wallace. His candor and gusto serve as an example for young scientists like myself, inspiring thoughtful analysis and effective communication. His guidance and suggestions proved most helpful in writing this thesis. I look forward to his supervision and collaboration as my studies continue. Thanks also to the rest of my committee, Gerard Roe and Dennis Hartmann. The insights that arose out of conversations with them served to greatly improve my ability to communicate as a scientist and carry out independent research.

Support from my family is a steadfast quality in life. My parents, Ron and Marthy, are largely to thank for instilling in me the work ethic that has helped me to achieve my ambition. Through their own quiet determination and persistence, I have learned to overcome frustration and persevere in the face of uncertainty. My brothers, Kevan and Jason, are two of the best friends I've ever had. I cannot count the number of times some combination of their humor and kindness have soothed my nerves. My Grandma B is and will always be a beacon for me, shining light on my successes and warmth on my worries. Her love of science influenced me from an early age, impressing upon me wonder and awe for the heavens above. Thanks must also go to my aunt Carol for her letters and words of empathy as I've progressed through graduate school.

Without friends, life would be a lonely endeavor. I am indebted to mine for sharing their time and energy throughout these past few years. Grads '06 are a fantastic bunch of people. Thanks to Angie, David, Dan, and Anthony for helping me to keep life in perspective, particularly when it's been frustrating or difficult. My peers in Mike's research group, Kevin, Justin, Joe, Rei, Katrina, Panos, and Masayo were always helpful and friendly. Such an environment is invaluable for a burgeoning student.

Though I'm not certain of much, I am supremely confident that my experience in graduate school would not have been the same without the presence of Kevin, Justin, and Sara. The positive feedback their friendship provided at critical moments allowed me to flourish and come into my own as an atmospheric scientist. To pay it forward is the greatest respect I can thank them with.

As I prepare to continue on with my studies, I'm left with an unexpected feeling of nostalgia for the time I spent working on my thesis. Somehow traveling is more satisfying than arriving, suggesting the journey is more important than the destination. With that in mind, I look forward to the next steps along this new path and to those with whom I will share them.

Chapter 1

INTRODUCTION

Northern Hemisphere (NH) wintertime climate variability is often characterized by spatial patterns of sea-level pressure (SLP) or geopotential height that represent preferred circulation regimes. These patterns of variability are often referred to as teleconnections, a term first used by Ångström (1935), due to their representation of contemporaneous, long-range connectivity in climatological fields. The existence, three dimensional structure, and regional impacts of teleconnections are intimately related to atmospheric dynamics; they have been linked to the movement of jets, barotropic instability, as well as wave propagation (Wallace and Gutzler, 1981; Simmons et al., 1983; Hsu and Lin, 1992; Hoskins and Ambrizzi, 1993). Teleconnection represent preferred regimes amongst the variety of circulation patterns displayed by the atmosphere from one month to the next, providing insight into the dominant modes of atmospheric variability.

The study of recurrent large-scale circulation patterns has progressed from its origins in heuristic investigations of station data during the late nineteenth century to contemporary, objective studies of globally gridded data. The latter have produced a variety of patterns that explain the large scale fluctuations of the atmosphere, such as El Niño / Southern Oscillation (ENSO), the Northern Annular Mode (NAM), and the Pacific North American (PNA). These patterns are most prominent over the oceans.

Less attention has been paid to variability over the continents, notably Eurasia. A survey of the literature provides some examples of patterns with action over the Eurasian supercontinent. However, these patterns have tended to be defined at heights in the middle troposphere. As such, the characterization of Eurasian SLP variability lacks a clear definition. To better capture and describe NH wintertime climate variability, this thesis investigates a third, Eurasian pattern of NH SLP variability. By extending previous work, the results presented here provide a more detailed perspective on the structure and influence

of atmospheric variability over the Earth's largest landmass.

1.1 Techniques

Historical reviews of large-scale atmospheric variability often point to folklore as the earliest mention of long distance relationships in weather and climate (Stephenson et al., 2003). Seafaring explorers and fishermen were among the first to describe the contrasting character of winter climate anomalies between Greenland and Scandinavia, a general impact of the North Atlantic Oscillation (NAO) pattern (van Loon and Rogers, 1978).

Early scientific studies of teleconnections relied on investigators' intuition and ability to identify meaningful relationships within available data. Teisserenc de Bort (1883) is one example of such a study. Using temperature and pressure data from Europe and Asia extending back to the middle 1800s, Teisserenc de Bort grouped winters into five categories according to fluctuations in the position and strength of two prominent anticyclones, the Azores High and the Siberian High, and to a lesser extent, the Icelandic Low. Together, these features comprised his "*centres d'action*."

Later, Hildebrandsson (1897) extended this concept, analyzing time series of SLP at stations around the NH. He noted inverse relationships between Iceland and the Azores, as well as Siberia and Alaska. In contrast, he characterized the relationship between the Azores and Siberia as concordant, emphasizing the remarkable similarity of their respective time series.

The first use of the statistical method of correlation within the field of atmospheric sciences has been attributed to Sir Gilbert Walker (Walker, 1997). Using lag correlations to predict the behavior of the Indian monsoon (1909), Walker remarked at the correspondence between flooding of the Nile and monsoon rains in Northwestern India, connecting the progression of winds over the eastern Mediterranean with those that developed later over India (1910). Walker was careful to address the limitations of his empirically derived statistics, noting that there was only a "tolerably close correspondence between the abundance of the Nile flood and the monsoon rains of northwest India." Shortly after Walker's pioneering application of correlation, the German meteorologist Felix Exner published the first one point correlation map of SLP using 10 years of data from 50 locations in the Northern Hemisphere

(1913). Aspects of the Arctic Oscillation pattern (Thompson and Wallace, 1998) are evident in the map, with an area of positive correlation over the polar cap and a longitudinally elongated area of negative correlation coefficients over the Mediterranean. He later updated the map using more stations and a longer data set, producing a map strikingly similar to the familiar NAO pattern (Exner, 1924).

Organizing correlations in global SLP variations into distinct groupings that he referred to as "oscillations," Walker (1924) coined the terms "North Atlantic Oscillation," "North Pacific Oscillation," and "Southern Oscillation." Later, he developed indices of these patterns using linear combinations of temperature and pressure time series at various locations that exhibit strong mutual correlations (Walker and Bliss, 1932). Wallace (2000) noted that Walker and Bliss' method is akin to empirical orthogonal function (EOF) analysis, and only subjective with respect to the stations that they chose to include in each index.

Continuing the same vein of investigation, subsequent investigators constructed indices of these patterns using the difference in SLP (Defant, 1924; Bjerknes, 1964; Wright, 1975) or surface air temperature (van Loon and Rogers, 1978) time series at stations in the patterns' opposing centers of action.

To the extent that the collection of aforementioned studies was performed using a subjective choice of stations, they may be considered subjective. Their goals were largely phenomenological, concerned with discussing observed phenomena with whatever empirical facts presented themselves at the time. Nevertheless, the physical intuition of these early atmospheric scientists was keen, and many of their results have stood the test of time.

Teleconnectivity

In their paper concerning NH midlatitude teleconnections, Wallace and Gutzler (1981) established a new statistic, "teleconnectivity," using one point correlation maps of SLP and 500 hPa geopotential height data. For a given base point, teleconnectivity is defined as absolute value of the largest negative temporal correlation between the base point and all other grid points. The authors noted that all their one point correlation maps were characterized by large positive correlation coefficients near the base grid point, but some displayed dipole

or wave-like horizontal structures with centers of statistically significant negative correlation coefficients adjacent to the positive area surrounding the base point. This observation formed the basis for using anti-correlation in the definition of teleconnectivity. By nature, large negative correlation coefficients occur at distance from base grid points and as such, describe the strength of long distance relationships.

Teleconnectivity maps have been used by subsequent authors (Esbensen, 1984; Mo and White, 1985; Barnston and van den Dool, 1993) to summarize one point correlation maps for all grid points in a manner similar to that of Wallace and Gutzler (1981). Other authors have drawn attention to limitations of the statistic. Branstator (2002) defined a circumglobal teleconnection pattern confined to the jet stream waveguide using DJF 300 hPa stream function data. He emphasized the fact that conventional teleconnectivity does not highlight their pattern because it focuses only on the magnitude of the teleconnection, and offered an alternative method based also on the remoteness of the teleconnection. Tsonis et al. (2008) pointed out that while teleconnectivity is effective at highlighting distant teleconnections, it does not effectively measure connectivity at other spatial scales, such as the nearby positive correlations.

Empirical orthogonal function EOF analysis

EOF analysis is the first in a series of objective techniques described here that have been applied for the purpose of finding structure in two-dimensional fields. The analysis yields a set of mutually orthogonal functions which account for a maximal fraction of variance in time and space. This greatly reduces the number of variables needed to describe the data. For example, applying the method to a series of SLP anomaly maps yields a smaller set of patterns that contain the predominant spatial structures common to all the input maps.

Arising from an impetus toward statistical prediction, EOF analysis was introduced to the atmospheric sciences by Lorenz (1956). Grimmer (1963) used eigenvectors to objectively analyze surface temperature over Europe. Noting its utility in describing the structure of the covariances in meteorological fields, Freiberger and Grenander (1965) suggested eigenanalysis be applied for the purpose of diagnosing large scale atmospheric variability. Mitchell

et al. (1966) recognized this potential as well, and recommended that EOF analysis be used to obtain an optimum set of climatological indices. Kutzbach (1967) employed this approach using three fields: SLP, surface temperature, and precipitation over North America. Kutzbach (1970) performed EOF analysis on 70 years of NH SLP anomalies to study climate fluctuations and circulation changes. Kidson (1975) used EOF analysis to determine whether the method could reproduce the dominant features of monthly mean SLP data. He applied the technique in two different ways, once to data with the annual cycle included and once using data with the annual cycle removed. Trenberth and Paolino (1980) obtained the leading three EOFs of annual-mean SLP anomalies. They also performed EOF analyses on seasonal-mean SLP anomalies for all seasons. The seasonal means were formed out of monthly mean SLP anomalies and the annual means were formed by averaging the four seasonal means. Wallace and Gutzler (1981) used EOF analysis in their study of mid-latitude teleconnections to investigate whether the patterns defined using teleconnectivity would appear among the leading EOFs of 500 hPa geopotential height. Trenberth and Shin (1984) performed EOF analysis on NH SLP data in search of quasi-biennial oscillations. Gutzler et al. (1988) applied EOF analysis to the wintertime-mean, NH 850 hPa temperature field. Thompson and Wallace (1998, 2000) used EOF analysis as the basis for their investigation of the leading pattern of NH SLP variability, the Northern Annular Mode (NAM). Eichelberger and Hartmann (2007) utilized the leading EOF of zonal mean zonal wind to investigate zonal asymmetries in the NAM.

EOF analysis has become a prominent technique in the atmospheric sciences. The spatial patterns represented by EOFs are often interpreted as teleconnection patterns with dynamical origins, particularly the leading mode. Notwithstanding its strengths, authors have discussed shortcomings of the method related to sampling fluctuations (North et al., 1982), domain sensitivity, faithfulness to underlying physical mechanisms (Richman, 1986), and a proper null hypothesis to assist in determining statistical significance (Dommenget, 2007). Most investigators are aware of and have been cautious about interpreting the higher order modes. This has led to the development of extended and alternative techniques that address some of these deficiencies.

Rotated EOF analysis

The primacy of the variance maximizing constraint in EOF analysis can lead to the selection of orthogonal functions on the basis of geometrical constraints rather than well defined physical motivations. Historically, this prompted investigators to "rotate" or linearly transform a subset of their EOFs subject to a subjective condition that produced a more meaningful solution. This procedure was first described by Thurstone (1932), and later expanded into a set of five rules delineating "simple structure" (Thurstone, 1947). Kaiser (1958) discusses rotation in the context of psychological research, acknowledging the need for more objective criterion for the rotation of eigenvectors. His varimax criterion remains a widely used method of rotation today.

Applied to studies of large-scale climate variability, rotation allows one to sacrifice one or both of the orthogonality constraints imposed by conventional EOF analysis to achieve a more physically interpretable result, often in the form of regionalized manifestations of the input eigenvectors.

Horel (1981) applied rotated principal component analysis (RPCA, another term for rotated EOF analysis) to Northern Hemisphere (NH) wintertime 500 hPa geopotential height data for 15 winters. Barnston and Livezey (1986) performed RPCA on 700 hPa geopotential height data for individual calendar months over a 35-year period. Gutzler, Rosen, and Salstein (1988) extended their EOF analysis of the wintertime mean 850 hPa temperature field performing a varimax rotation as well. Kushnir and Wallace (1989) employed RPCA to examine structure in three datasets comprising bands of low frequency variability in 500 hPa geopotential height. Kawamura (1994) used rotated EOF analysis to seek structures in global sea surface temperature (SST) data on interannual and interdecadal timescales.

In cases where the physical mechanisms underlying modes of variability do not produce mutually orthogonal patterns, rotated EOF analysis offers the possibility of recovering those structures, particularly if the structures of the inherent modes are consistent with the simplicity condition required by the REOF analysis. For this reason, rotated EOF analysis is an appropriate tool for investigating teleconnection patterns.

Sectoral EOF analysis

Subdomain stability was among the critiques of EOF analysis presented by Richman (1986). He argued that in order for a EOF to be considered a mode of variability, it must remain stable regardless of whether the entire NH is the domain or a smaller portion of the hemisphere were used. In other words, an EOF may be considered significant if the same mode is found in different analysis domains.

A popular approach to isolating patterns of variability in separate regions of the NH is to apply conventional EOF analysis to sub-sectors of the hemisphere. Hurrell (1995) defined the NAO as the first singular vector yielded from an SVD analysis of SLP and sea-surface temperature (SST) fields from a domain bounding the North Atlantic. Rennert (2007) applied this approach dividing the hemisphere along $90E$ and $90W$, obtaining the NAO and PNA as the leading pattern of wintertime 500 hPa geopotential height variability in the Atlantic and Pacific sectors, respectively. Very similar patterns appear as EOF1 and EOF2 of the same analysis applied to a domain comprising the extratropical NH ($90N - 20N$). Wettstein (2007) employed a similar approach, analyzing results of conventional EOF analyses of upper level eddy statistics for similarly defined Atlantic and Pacific sectors. Eichelberger and Hartmann (2007) used sectoral EOF analysis to contrast differences in the structure of zonal-mean zonal wind variability in the Atlantic and Pacific Ocean basins.

The use of sectoral EOF analysis is consistent with the interpretation of teleconnections as regionally-dependent, geographically fixed phenomena (Blackmon et al., 1984). When paired with an EOF analysis performed on an essentially unbounded domain such as the NH, sectoral EOF analysis can offer confirmatory results or suggest problems related to sub-domain stability.

Empirical orthogonal teleconnection (EOT) analysis

First described by van den Dool et al. (2000), empirical orthogonal teleconnection (EOT) analysis is a novel formulation of techniques used previously in the atmospheric sciences. EOT works in a stepwise fashion, finding successive grid points in a spatial field whose time

series explain the largest fraction of the temporal variance at all points. After a point is identified, the variance that it explains is removed from the original data matrix by linear regression and the search for the next most important point begins. The procedure can be applied until all of the original variance has been explained. EOTs are similar to EOFs in that they represent an objective method of selecting patterns that explain the maximum amount of variance in a data set. Due to the method of regressing each mode out of the original data, the time series associated with successive modes are mutually orthogonal. Each EOT is associated with a map analogous to the one point correlation maps shown by Wallace and Gutzler (1981) and a time index defined by the time series of original or reduced data at the base grid point.

EOTs have been discussed by various authors, generally in comparison to other techniques. Jolliffe (2002) likens the method to an uncentered version of principal component analysis due to its use of nonstandard definitions of standard deviation and correlation[1], and interprets the first EOT as a compromise between the first EOF obtained from the covariance and correlation matrices. Hannachi et al. (2007) argue that the EOT technique is not as simple as other objective methods, but acknowledge its ability to produce more physically interpretable patterns.

Franzke (2002) used EOT to investigate low frequency atmospheric variability. They applied the method to 300 hPa stream function data obtained from a simplified GCM, exploring its response to the relative zonal position of a single storm track. Franzke and Feldstein (2005) modified the EOT procedure slightly in their analysis of the continuum of NH teleconnection patterns. Instead of associating each EOT with the time series of original or reduced data at its base point, they defined an index by projecting the EOT map onto daily 300 hPa stream function data. van der Schrier et al. (2006) investigated patterns of summertime moisture variability across Europe by applying EOT analysis to Palmer Drought Severity Index data over the twentieth century.

---

[1]van den Dool et al. (2000) do not remove the time mean before calculating standard deviation or correlation.

Other methods

Other methods designed to find spatial patterns of climate variability have been developed, but are not performed for this thesis nor discussed in detail. Hannachi et al. (2006) described another method of obtaining simple structures in climatological data. Their simplified empirical orthogonal functions (SEOF) are designed to resolve difficulties associated with rotation. The SEOF method achieves simplicity by reducing some loadings to exactly zero while requiring that the patterns be orthogonal and maximize explained variance. The strength of the reduction can be tuned. Hannachi (2007) described a method for finding so-called trend EOFs, structures associated with trends in climate data. Dommenget (2007) introduced "distinct EOFs" (DEOFs), which like rotated EOFs, are determined iteratively through a process that maximizes the difference in explained variance between the DEOF and a stochastic null hypothesis. Another novel method, optimally interpolated patterns (OIPs), uses a spectral-based approach to yield mutually orthogonal patterns in climate data (Hannachi, 2008). The method optimizes interpolation error variance, which is obtained by integrating the inverse of the variable's cross-spectrum over the spectral domain. OIPs, or interpolated EOFs, rank patterns on the basis of long term variability. In other words, the leading patterns, those with the largest error interpolation variance, are associated with fluctuations of the lowest frequencies.

1.2 Prior results

The various methods utilized to investigate large-scale climate variability have produced a variety of teleconnection patterns. Here we focus on studies that presented a pattern over the Eurasian continent. Teisserenc de Bort (1883) was among the first to reference Eurasian variability in the literature. The Siberian High was included in his "*centres d'action*," and was a prominent contributor to European wintertime climate in his discussion of various types of winters. For example, the cold and dry Type-A winter was typified by a broad Siberian High extended westward into eastern Europe, and a Azores High displaced slightly westward. Teisserenc de Bort hypothesized that land surface conditions like Eurasian snow cover might contribute to these shifts.

Subsequent authors referenced the Siberian High (Hildebrandsson, 1897) and Eurasia in general (Exner, 1924), but interest soon focused on the large ocean basins and their "oscillations" (Walker, 1924; Walker and Bliss, 1932). Fukuoka (1951) used a method analogous to EOF analysis to analyze January 1941 SLP over the Far East motivated by long-range forecasting. His first component is dominated by opposing SLP anomalies over the continent and ocean, which may be interpreted as a measure of the strength of the East Asian Winter Monsoon. The third EOF of January SLP anomalies obtained by Kutzbach (1970) contained two primary centers of action, a positive center over northwest Russia and a negative center over Iceland. Kutzbach associated the negative phase of the pattern with blocking along the west coasts of North America and Europe. Kidson (1975) performed EOF analysis on SLP data with and without the influence of the annual cycle. The analysis of monthly mean SLP data produced two EOFs with action over Eurasia. EOF3 was characterized by a single isotropic anomaly centered near St. Petersburg, Russia. EOF4 was a dipole between the eastern and western Arctic, with the former center, over northern Siberia, dominating. The analysis performed on monthly mean SLP anomalies yielded several EOFs with centers over Eurasia. EOF2 was characterized by a single, zonally elongated, positive anomaly over the entire northern tier of Eurasia, centered south of Novaya Zemlya. EOF5 was also dominated by a single center of action, but much smaller and more isotropic, and was centered farther to the west over Scandinavia. EOF4 and EOF6 took on the appear of zonally oriented wave trains, approximately in quadrature with one another. Kidson showed that PC2 of the latter analysis was well correlated with PC3 and PC4 of the analysis with the annual cycle included. EOF3 of the annual and winter analyses by Trenberth and Paolino (1980) demonstrated a familiar center of action over western Eurasia. However both patterns were also characterized by centers of action over the mean position of the Icelandic and Aleutian Lows, making them difficult to interpret.

Wallace and Gutzler (1981) defined their Eurasian pattern (EU) as a linear combination of 500 hPa geopotential height data for three points: one over Scandinavia, one over Siberia, and the third over Japan. They noted that Eurasia has generally high teleconnectivity at the 500 hPa level, but lacks clear maxima that provide a basis for identifying patterns in their scheme. Although a weak center is evident at $70E$ in their analysis of SLP telecon-

nectivity, their interpretation of the teleconnectivity results for SLP is limited to the seesaw oscillations of the North Atlantic and Pacific.

The map associated with the fourth rotated principal component that emerged from RPCA analysis of Horel (1981) is centered north of the Siberian coast in the Arctic Ocean and has secondary centers over the Tibetan Plateau and Scandinavia. Whereas the leading three rotated PCs are characterized by strongly regional teleconnection patterns comprised of centers arranged in meridional seesaws or arching wave trains, the fourth is dominated by a single center of action. Barnston and Livezey (1986) identified patterns of low frequency variability on the basis of observing similar structures in the results of rotated EOF analysis applied to sets of SLP anomalies from individual calendar months. Among the nine wintertime patterns described in their study, three possessed strong centers over Eurasia. The first, the Northern Asian, is dominated by a single center of action extending along the Arctic coastline, similar to the pattern described by the fourth rotated principal component of Horel (1981). The other two patterns over Eurasia identified by Barnston and Livezey (1986), Eurasian type-1 and type-2, are essentially orthogonal east-west wave trains extending across the Eurasian continent. The type-1 Eurasian pattern corresponded well with the Eurasian pattern identified by Wallace and Gutzler (1981), and is now generally referred to as the Scandinavian pattern (Wibig, 1999; Qian, Corte-Real, and Xu, 2000; Scherrer, Croci-Maspoli, Schwierz, and Appenzeller, 2006; Bueh and Nakamura, 2007).

Dole and Gordon (1983) described characteristics of the low-frequency variability, but offered little interpretation of the features over Eurasia, focusing rather on patterns over the large ocean basins. The authors identified areas of strong low-frequency persistence in the NH wintertime 500 hPa circulation by selecting cases of persistent anomalies at individual grid points defined on the basis of magnitude and duration of anomalies. Three areas of the NH were selected for description: the North Atlantic (ATL), the North Pacific (PAC), and the Northern Soviet Union (NSU). The authors found that persistent anomalies in all three regions had grossly similar persistence characteristics, with similar numbers of positive and negative persistence cases with durations of 10 days. The authors performed regional analyses on the ATL and PAC regions, but not the NSU region. A subsequent paper (Dole, 1986) extended previous work by ascertaining the horizontal and vertical structure of typical, per-

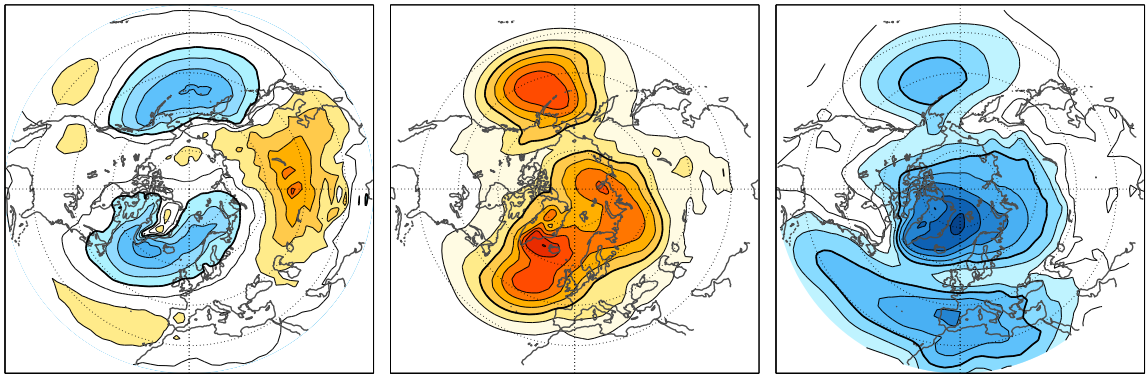

Fig. 1.1: (Left) DJFM mean SLP based on monthly-mean data. Contour interval is 4 hPa; contours less than 1012 and greater than 1020 shaded; bold reference contour is 1012 hPa. (Center) Variance of monthly-mean DJFM SLP. Contour interval is 10 hPa^2; bold reference contour is 30 hPa^2. (Right) Domain SLP variance explained by the one-point covariance maps for individual grid points. Contour interval is 2%; bold reference contour is 10%.

sistent positive and negative anomalies observed in each region. Interestingly, Dole (1986) associated the primary patterns in the ATL and PAC regions with the Eastern Atlantic and Pacific North American (PNA) patterns of Wallace and Gutzler (1981), but found no analog for the NSU region anomalies. However, he did find that anomalies in the NSU region have a pronounced impact on the Siberian High (left panel, Fig. 1.1), the nearest climatological mean feature.

The leading EOF of wintertime 850 hPa temperature is characterized by centers of action over western Canada and north central Eurasia (Gutzler et al., 1988). EOF2 from the same analysis was characterized by a dipole between eastern Siberia and western Canada. Gutzler and coauthors noted a correspondence between the centers in EOF1 and centers in two of the teleconnections described by (Wallace and Gutzler, 1981), the PNA and the EU. The varimax rotation performed by Gutzler et al. (1988) yielded several patterns with distinct action over Eurasia. Their REOF2 was represented by a single zonally elongated center stretching from east central Asia to western Canada. REOF3 was a dipole between central Eurasia and the area between Greenland and Svalbard.

Thompson and Wallace (2000) showed that the leading mode of NH SLP variability,

the NAM, does extend onto Eurasia; later they showed that the NAM has a considerable influence on regional climate across Eurasia (Thompson and Wallace, 2001), both in terms of cold minimum daily temperatures and blocking days over northwest Russia.

In a recent study, Panagiotopoulos et al. (2005) examined trends and teleconnections of the Siberian High. They found that none of the established teleconnection patterns were related to the Siberian High in a statistically significant manner, nor could any reproduce the observed variability and trends in the climatological feature.

1.3 Summary and Objectives

While patterns over Eurasia at upper levels have been identified and discussed, dominant patterns of low frequency variability in monthly-mean SLP have received less attention. Given the considerable interannual SLP variance observed across northern Eurasia (middle panel, Fig. 1.1), as well as the ability of points there to compete for hemispheric variance explained (right panel, Fig. 1.1), further investigation of its variability is warranted.

This thesis utilizes four objective methods of analysis toward the goal of an optimal definition of a single pattern of Eurasian climate variability. Each uses linear functions to maximize variance explained in a SLP data set. First, conventional empirical orthogonal function (EOF) analysis is performed on SLP anomalies $20N - 90N$. This yields a third EOF with a primary center of action over Eurasia and secondary centers over the western Arctic and North Atlantic. Rotated EOF analysis is performed to extend the results of the conventional EOF analysis. The EOF method is also applied to three equally sized sectors of the Northern Hemisphere to corroborate results of the EOF and REOF analyses. Fourth, the EOT method is applied to the same SLP anomalies to complement the series of EOF based analyses (van den Dool et al., 2000).

Each of the techniques used in this study are described in detail in Chapter 2. Data sources are also discussed. Chapter 3 presents results of the aforementioned analyses and interprets them collectively as a single pattern of Eurasian SLP variability. Chapter 4 describes the three-dimensional structure of the Eurasian pattern, inferred from regressing other climatological fields onto its time series. It also illustrates how its signature varies throughout the year. Chapter 5 attempts to describe the influence of the Eurasian pattern

on day-to-day weather. It does so using composites to illustrate how climatological fields are perturbed by the pattern in its opposing phases. Regional climate impacts are also quantified, relating shifts in the time series associated with the Eurasian pattern to meteorological variability on the scale of days to weeks. Chapter 6 explores the time evolution of the pattern on the basis of composites formed from an EOT analysis of five day mean wintertime SLP anomalies. Chapter 7 concludes with a discussion of all the preceding results.

Chapter 2

DATA AND METHODS

2.1 Data sources

The primary source of data used in this thesis are monthly mean and daily mean fields from the NCEP-NCAR reanalysis product (Kalnay and Coauthors, 1996). The data set is created by assimilating global, historical climate observations into a numerical weather prediction model, forecasting a series of fields six hours later, optimally matching the forecast with the next set of observations, and interpolating the output to a 2.5° latitude by 2.5° longitude grid. Compared to operational analyses from weather forecast models, reanalysis products have the advantage of being globally gridded and dynamically consistent in the sense that one model is used to forecast over the entire time period. The NOAA Earth Systems Research Laboratory (ESRL, formerly Climate Diagnostics Center) provides 6 hour, daily mean, and monthly mean values of numerous reanalysis fields. The analyses presented in Chapter 3 are based exclusively on monthly mean SLP data at latitudes north of $20N$ for winter months (DJFM) through the period December 1958 – March 2008. The same time period is adopted for subsequent analyses.

A fourth-order Butterworth filter with a cutoff frequency near 1/6 days^{-1} was applied to daily mean NCEP-NCAR 300 hPa geopotential height data to generate a low-pass filtered height field for use in Chapter 5. A corresponding 6-day high-pass filtered height field was obtained by subtracting the low-pass field from the unfiltered daily means.

Five day mean data were constructed from daily mean SLP data for use in Chapter 6. For all 50 winters, 24 pentads were formed. Collectively, these 24 pentads span the first 120 days of each winter (December – March), including February 29 in leap years.

Monthly means of other climatological fields are used in Chapter 4. These include: geopotential height, air temperature, u and v wind, and vertical velocity. With the exception of vertical velocity, 17 vertical levels are available for each field. The $1000 - 500$ hPa

thickness is also used in Chapter 4.

The ECMWF Reanalysis product (Uppala and coauthors, 2005) was used to verify results obtained using the NCEP-NCAR data set. Additionally, the analyses described in Chapter 3 were performed on the Early 20th Century Reanalysis product obtained from Gilbert Compo at NOAA ESRL. The ESRL product spans the time period 1908 – 1958.

For a given variable, X, monthly mean anomalies, X', were obtained by subtracting the respective long term monthly mean, $\overline{X}$ from each month of the time series X at each grid point. When performing EOF, REOF, and EOT analysis, the data were area weighted by multiplying each point by the cosine of its latitude.

The sea ice extent data used in Chapter 4 were obtained from the NCEP optimal interpolation (OI) product (Reynolds et al., 2002). The mean wintertime sea ice extent line is defined by the 15% concentration contour obtained through averaging monthly mean sea ice concentration data for DJFM 1981 - 2006.

Snow extent data were obtained from the Rutgers University Global Snow Lab. Both gridded data and area of snow extent data are used in Chapter 5

High resolution gridded monthly mean surface air temperature and precipitation data used in Chapters 4 and 5 are from the CRU TS 2.1 dataset obtained from the Climate Research Unit (CRU) at the University of East Anglia (Mitchell and Jones, 2005). Each set of data are for land only and set on a 0.5° latitude by 0.5° longitude grid.

2.2 Methodology

Empirical orthogonal function (EOF) analysis

A tool of the mathematician and the applied scientist, empirical orthogonal function (EOF) analysis aims at the efficient representation of variance contained in a 2D data set. In the context of the present study, this is determined via the isolation of structures within the data that explain the maximal fraction of variance in time and space. The analysis produces spatial patterns, referred to as EOFs or eigenvectors, and their respective time-varying indices, called principal components (PCs). EOFs are mutually orthogonal in space and the corresponding PCs are mutually orthogonal in time. This linear independence is an advan-

tage for many applications, among them statistical prediction.

The eigenanalysis performed here begins with the formation of the SLP covariance matrix, $[S_x]$.[1] Depending on how the dispersion matrix is calculated, each value in the matrix represents the temporal or spatial covariance between corresponding spatial or temporal points. In this case, X represents SLP anomalies and $[S_x]$ is constructed to contain the covariance over N time points at M spatial grid points.

$$[X'][X']^T(N)^{-1} = [S_x] \tag{2.1}$$

Following from Wilks (2006), the mathematical formation of eigenvectors begins with the diagonalization of S_x, satisfying:

$$[S_x]\mathbf{e} = \lambda\mathbf{e} \tag{2.2}$$

or,

$$([S_x] - \lambda[I])\mathbf{e} = \mathbf{0} \tag{2.3}$$

A solution of this form follows from the symmetric property of the $M \times M$ covariance matrix, and yields M pairs of eigenvalues, λ, and orthogonal eigenvectors, $\mathbf{e}$. Equation 2.2 may be expressed equivalently as:

$$[S_x] = [E][\Lambda][E]^T \tag{2.4}$$

Here, the matrix $[E]$ holds eigenvectors in each of its M rows and $[\Lambda]$ is a diagonal matrix with eigenvalues along its nonzero elements. Eigenvalues express the amount of variance explained by their corresponding eigenvector, and may be ranked accordingly. The fraction of total variance explained by each eigenvector may be determined by dividing each eigenvalue by their sum.

$$R_k^2 = \frac{\lambda_k}{\sum_{k=1}^{M} \lambda_k} \times 100\% \tag{2.5}$$

[1]Equations presented hereafter utilize matrix notation, where a quantity in brackets, $[x]$, is a matrix, the T superscript refers to the matrix's transpose, N is the length of the time series, M is the number of spatial grid points, and $[I]$ is the identity matrix.

The complete set of eigenvalues accounts for all the variance in the original data, X'. In other words, the sum of the eigenvalues is equal to the sum of the covariance.

$$\sum_k \lambda_k = \sum_m S_m \tag{2.6}$$

Principal components (PCs), the time series which represent eigenvector fluctuations, can be obtained by regressing the original data onto the eigenvectors.

$$[U] = [E]^T[X'] \tag{2.7}$$

The matrix $[U]$ contains M components of length N. Similar to their eigenvector counterparts, the PCs are orthogonal to one another.

$$\mathbf{u}_i^T \mathbf{u}_j = \begin{cases} 1 & \text{if } i = j \\ 0 & \text{if } i \neq j \end{cases} \tag{2.8}$$

We standardize each PC to have unit variance. This enables us to regress the SLP field onto the normalized PC to form a map of SLP anomalies corresponding to a one standard deviation fluctuation in the PC. Such a map is often preferred to displaying the actual EOF, both for its physical units and attendant interpretability.

Rotated EOF analysis

Rotation of eigenvectors proceeds by linearly transforming a subset of eigenvectors.

$$[E_r] = [E][T] \tag{2.9}$$

In equation 2.9, $[E]$ is the subset matrix of selected original eigenvectors, $[E_r]$ contains the rotated eigenvectors, and $[T]$ is the transformation matrix. We seek a solution with orthogonal principal components, and therefore subject the transformation matrix to the condition,

$$[T][T]^T = [I] \tag{2.10}$$

A subset comprised of the first 25 eigenvectors were selected for rotation in this case. Amongst the numerous selection rules available (see Preisendorfer et al. (1981) or Jolliffe (2002)), the first lower bound Guttmann criterion (Guttmann, 1954) was used to guide

truncation. Horel (1981) used a similar approach in a rotated principal component analysis of NH 500 hPa height data. The first Guttmann criterion recommends truncating at no less than the first eigenvector that explains less than one unit of variance, which in this case is 15 eigenvectors. Ultimately, 25 eigenvectors were selected for rotation on the basis of obtaining a stable solution regardless of how many eigenvectors were rotated.

We used the commonly applied varimax rotation (Kaiser, 1958), which maximizes the simplicity condition

$$V = \sum_{j=1}^{r} \left(\left[m \sum_{i=1}^{m} (e_{ij}^2/h_i^2) - \left(\sum_{i=1}^{m} (e_{ij}^2/h_i^2) \right)^2 \right] /m^2 \right) \tag{2.11}$$

where m is the number of loadings, r is the number of eigenvectors selected for rotation, e are the eigenvector loadings, and h^2 are the eigenvector communalities (2.12).

$$h_i^2 = \sum_{j=1}^{r} \frac{\mathrm{var}(\mathbf{e}_i \mathbf{u}_j)}{\mathrm{var}(X_i)} \tag{2.12}$$

where X are SLP time series at each grid point, i.

(2.11) is referred to as the *normal* varimax criterion, because the eigenvector loadings are scaled by their communalities, a quantity that may be interpreted as the variance of the squared multiple correlation between the truncated eigenvectors and the variable (the proportion of variance at a grid point explained by all the eigenvectors, see Eq. 2.12). In other words, the communality is associated with the sum of the squares of the loadings at a particular grid point. Rescaling each eigenvector in accordance with its explained variance removes the bias toward the leading eigenvectors. After rotation, the eigenvectors are re-weighted by the square root of their respective communality (2.11).

Simplicity is achieved by maximizing V (i.e., the variance of the squares of the loadings), pushing the loadings towards 0 and 1. In terms of the maps, rotation increases interpretability by tending to regionalize patterns, flattening secondary centers with loadings near 0, and bolstering primary centers with loadings closer to ± 1.

The normal varimax rotation produces an orthogonal transformation matrix which may be used to derive the rotated eigenvectors, principal components, and eigenvalues. However, to ensure that the rotated principal components are orthogonal, we must employ a

new eigenvector scaling,

$$||\mathbf{e}|| = \lambda^{-1/2} \tag{2.13}$$

where the length of each eigenvector is scaled by the square root of its corresponding eigenvalue. When rotated, the scaled eigenvectors produce oblique rotated eigenvectors with orthogonal principal components. This procedure also stabilizes the solution obtained with respect to how many eigenvectors are rotated. This occurs because the leading eigenvalues are large, and weight the leading eigenvectors accordingly.

$$[E_r]^T[E_r] = \left([E][\Lambda]^{-1/2}[T]\right)^T [E][\Lambda]^{-1/2}[T] \tag{2.14}$$

$$= [T]^T[\Lambda]^{-1/2}[E]^T[E][\Lambda]^{-1/2}[T] \tag{2.15}$$

$$= [T]^T[\Lambda]^{-1}[I][T] \tag{2.16}$$

$$= [\Lambda]^{-1} \tag{2.17}$$

and,

$$\begin{aligned}(N)^{-1}[U_r][U_r]^T &= (N)^{-1}[E][\Lambda]^{-1/2}[T][X'] \left([E][\Lambda]^{-1/2}[T][X']\right)^T \\ &= (N)^{-1}[X'][X']^T[E]^T[E][\Lambda]^{-1}[T]^T[T] \\ &= \left([E][\Lambda][E]^T\right)[I][\Lambda]^{-1}[E][E]^T \\ &= [I] \end{aligned} \tag{2.18}$$

Here we give up one of the orthogonality properties inherent in the conventional EOF analysis. However, this is not viewed as a disadvantage, because we do not necessarily expect orthogonal patterns in the SLP field, but prefer uncorrelated principal components.

Sectoral EOF analysis

Conventional EOF analysis was performed for three evenly spaced sectors of the NH SLP data described earlier in this chapter. The Atlantic sector spans 90W to 30E, or central North America to eastern Europe. The Eurasian sector extends from 30E to 150W, comprising the northern tier of the supercontinent. The Pacific sector is defined by the remainder of the hemisphere, or 150E to 90W.

Empirical orthogonal teleconnection (EOT) analysis

Following van den Dool et al. (2000), the EOT procedure can be expressed mathematically as follows. After determining sb_1, the point in space that explains the maximum possible variance at all other points s, its associated one-point correlation map is defined as the first EOT. The time series associated with EOT1 is simply the original time series for its base point.

After finding EOT1, the data are split into a portion whose variance is explained, X_e and a residual, X_r. Both are calculated for all s and t.

$$X_e(s,t) = \alpha_1(t)e_1(s) \tag{2.19}$$

$$X_r(s,t) = X(s,t) - X_e(s,t) \tag{2.20}$$

where,

$$\alpha_1(t) = X(\mathrm{s}b_1, t) \tag{2.21}$$

$$e_1(s) = \rho^*_{s,sb_1}\left(\sigma^*_s \sigma^*_{\mathrm{s}b_1}\right) \tag{2.22}$$

The standard deviation and correlations are calculated without the removal of the time mean (indicated by an asterisk), resulting in a regression through the origin (Brownslee, 1965). Jolliffe (2002) argues that this may make the resulting patterns difficult to interpret, to the extent that "regression" and "correlation" are no longer defined in the usual manner. However, by construction the mean of the monthly anomalies used here is zero, bypassing the nuance altogether.

After dividing the data into explained and residual portions, the procedure may be repeated using the once-reduced data. The point in space that explains the most variance at all other points in X_r becomes the base point for EOT2. The time series connected with EOT2 is represented by the series at its base point in the once reduced data. After removing the variance explained by EOT2 from the data set, the process is repeated again, and so on until all of the domain variance in the original data is explained. X_e grows at the expense of X_r, reordering the variance in the original data as EOT modes. The total variance in

the data is expressed by (2.23),

$$\text{DVAR} = \frac{1}{nm} \sum_{t=1}^{n} \sum_{s=1}^{m} X(s,t)^2 \tag{2.23}$$

where n is the number of points in time and m is the number of points in space. The amount of variance explained by a particular EOT is related to the fraction of its explained variance to the total domain variance (2.24).

$$\text{V}AR_{exp} = \left(\frac{1}{nm} \sum_{t=1}^{n} \sum_{s=1}^{m} X_e(s,t)^2 / \text{DVAR} \right) \times 100\% \tag{2.24}$$

The space-time relationship presented is not the only orientation available. It may be reversed from the outset to obtain the point in time whose map explains the most spatial variance. Examples of this inverted procedure are shown in van den Dool et al. (2000).

Chapter 3

OBTAINING A ROBUST PATTERN OF EURASIAN VARIABILITY

This chapter seeks to identify a robust pattern of wintertime climate variability over Eurasia through objective methods. Although Eurasia has received attention in the literature, few studies have identified patterns of climate variability intrinsic to the region, and none have established the existence of a dominant pattern of Eurasian sea level pressure (SLP) variability.

3.1 Empirical Orthogonal Function (EOF) Analysis

The first three patterns associated with the eigenanalysis of the SLP covariance matrix are shown in Fig. 3.1. They explain 22.7%, 12.5%, 9.9% of the domain DJFM variance, respectively. EOF1 has been used as the definition of the so-called Arctic Oscillation (AO) or Northern Annular Mode (NAM) (Thompson and Wallace, 1998). EOF2 is dominated by a single center of positive anomalies over the North Pacific Ocean. Its features resemble the primary center associated with the Pacific North American (PNA) pattern in the 500 hPa height field; hence, this surface pattern has been referred to as PNA-like (Quadrelli and Wallace, 2004). Quadrelli and Wallace (2004) offered a linear framework characterized by a two-dimensional phase space defined by the first two principal components of SLP. While Quadrelli and Wallace (2004) emphasize that their framework accounts for many of the varied patterns of NH wintertime climate variability, they acknowledge that features associated with the higher modes may still be dynamically important. For example, EOF3 is associated with a broad area of correlation at the surface and an extensive wave-train spanning Eurasia at upper levels (not shown). Overland and Wang (2005) illustrate how Arctic variability is not well captured by the first two patterns of hemispheric variability, and may also be linked to the behavior of the third pattern. These results motivate further investigation of EOF3.

Analysis of the EOF3 is encumbered by several shortcomings, requiring an alternative approach to define the pattern. Although the pattern is dominated by a single region of positive anomalies centered around $65N, 65E$, several secondary centers also exist. Their reality and significance are questionable. Furthermore, while the third eigenvalue is separated from the second (Fig. 3.2), its separation from the fourth is equivocal. This casts uncertainty on whether or not EOF3 is in line with the rule-of-thumb proposed by North et al. (1982), associated with the statistical significance of individual eigenvectors.

EOFs are noted for their efficiency in representing variability in a data matrix thanks to the orthonormality constraint imposed by EOF analysis. However, this strength can become a weakness if it selects patterns on the basis of geometrical considerations rather than according to the underlying dynamics. This is not a concern for the leading eigenvector, but subsequent patterns may become degenerate in terms of their physical interpretability. This challenge can be overcome by relaxing one or both of the orthogonality constraints required of the eigenvectors through rotation.

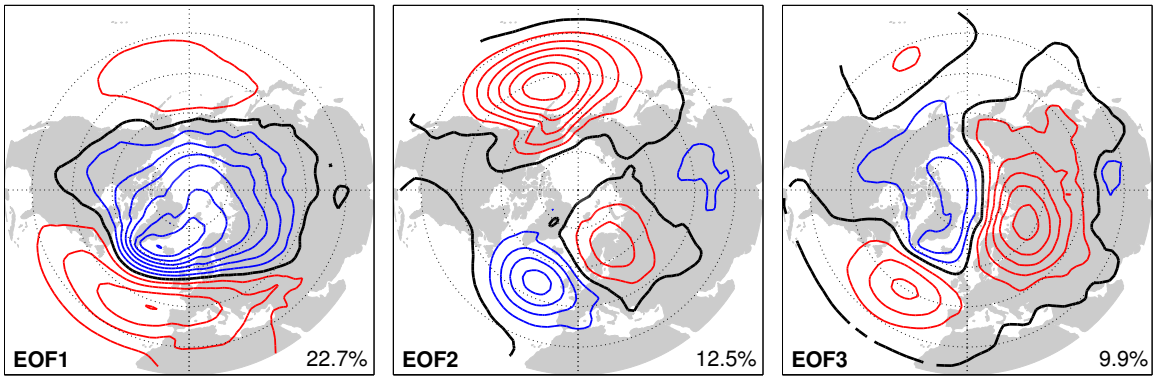

Fig. 3.1: First three eigenvectors (EOFs) derived from eigenanalysis of SLP covariance matrix. Regression of SLP data, X', onto the respective time series (here principal components) is displayed. Contour interval is 1 hPa. The fraction of domain variance explained by each pattern is shown at the bottom right of each panel. Positive contours are shown in red, negative in blue, and the zero contour in thick black.

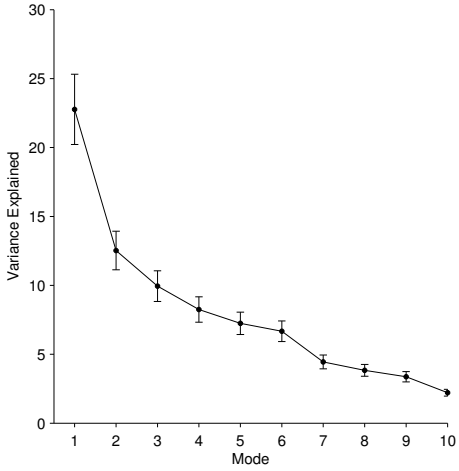

Fig. 3.2: Eigenvalues 1 - 10 and one standard deviation confidence intervals (North et al., 1982) associated with eigenanalysis of SLP covariance matrix. See North et al. (1982) for a discussion of the error calculation.

3.2 Rotated EOF (REOF) Analysis

The first three rotated eigenvectors from the varimax rotation of the first 25 PCs are shown in Fig. 3.3. They explain 17.9%, 10.2%, and 10.1% of the domain DJFM variance, respectively. All three can be described as qualitatively similar, regionalized versions of the respective leading EOFs. For example, the region of positive anomalies over the Pacific in EOF1 (Fig. 3.1) is suppressed in REOF1. Similarly, REOF3 exhibits a localization of the pattern represented in EOF3. The Pacific secondary center is all but absent, the other secondary centers are less prominent, and the dominant center of action is increased in amplitude by 1 hPa. The third rotated pattern shown here bears a strong resemblance to the pattern shown by Hannachi et al. (2006), who rotated the first 20 eigenvectors from a conventional EOF analysis.

As discussed in Chapter 2, these REOF patterns are not mutually orthogonal, but their respective rotated principal component time series are orthogonal.

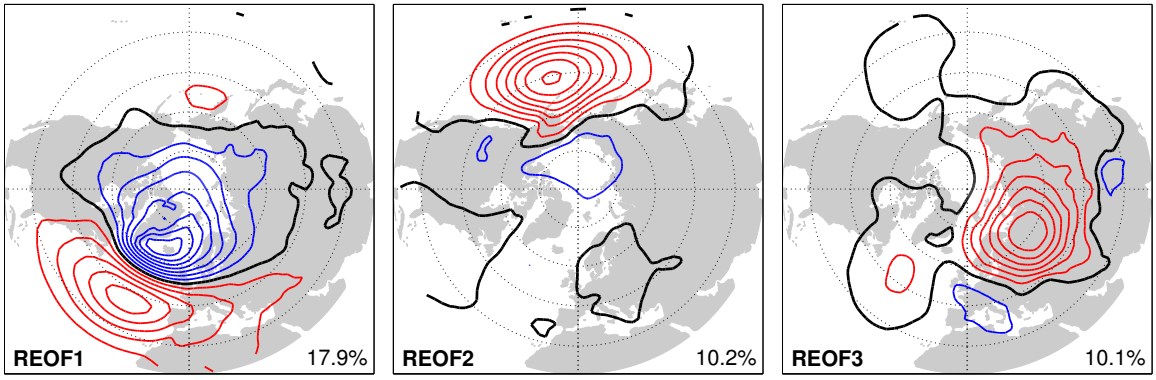

Fig. 3.3: First three rotated eigenvectors (REOF) associated with varimax rotation of first 25 principal components of original eigenanalysis. Display is as in Fig. 3.1.

3.3 Sectoral EOF (sEOF) Analysis

Results from the conventional and rotated EOF analyses exhibit centers of action over the NH ocean basins and the Eurasian supercontinent. This suggests the use of a sector approach to confirm the ascendancy of each pattern in its respective sector of the hemisphere.

Results of three sectoral EOF analyses are shown in Fig. 3.4. Each pattern explains over a third of the DJFM variance within its own domain. The regression patterns associated with the leading eigenvector for each sector are displayed along with their respective fraction of domain variance explained. The patterns appear qualitatively similar to those observed in the EOF and REOF analyses. In particular, the dominant features in the first three EOFs are well reproduced in their corresponding sectoral EOFs. Outside the sectors, differences arise in the weak centers observed in the original EOF analysis. The region of positive anomalies in the Pacific portion of EOF1 is weakened in both the rotated and sector EOF analyses. Similarly, the secondary centers over the Atlantic in EOF2 are less prominent in these latter analyses.

The sectoral approach is useful in corroborating patterns that appear to have prominence in discrete regions of the hemisphere. The choice of sectors used in this analysis was motivated by the shapes of the three the primary patterns of wintertime climate variability identified by the conventional EOF analysis. However, an inherent limitation of the sectoral

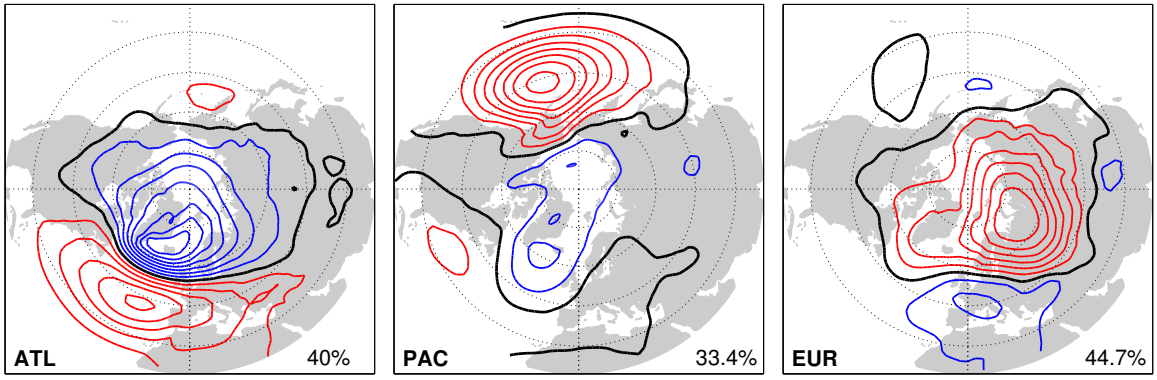

Fig. 3.4: Leading eigenvector associated with eigenanalysis of SLP covariance matrix for three sectors spanning the NH domain above 20°N. ATL sector extends from $90W$ to $30E$, EUR sector from $30E$ to $150E$, and PAC sector from $150E$ to $90W$. Display is as in Fig. 3.1.

approach is that the definition of domain boundaries is somewhat arbitrary. The subsets selected here were largely defined on the basis of geographical considerations. Various domain definitions were tested to determine the sensitivity of the results to the choice of sectoral boundaries. It was determined that the pattern obtained in the Eurasian sector is relatively insensitive to slight changes in the boundaries. Results of the sensitivity analysis are shown in Appendix A.

3.4 Empirical Orthogonal Teleconnection (EOT) Analysis

Fig. 3.5 shows the regression patterns associated with the first three EOTs of DJFM SLP′. EOT1 explains 18.5% of the domain DJFM variance, EOT2 explains 10.9%, and EOT3 explains 9.8%. Each is qualitatively consistent with the first three 700 hPa height EOTs shown by van den Dool et al. (2000), though not necessarily surface manifestations of exactly the same patterns. EOT1 resembles the familiar NAO pattern. Its base point is located at $75N$, $2.5W$, in the Greenland Sea between Greenland and Svalbard. Visual inspection suggests that it bears a strong resemblance to the leading modes found in the three previous subsections. EOT1 is highly correlated with these other patterns, possessing spatial correlation coefficients in excess of 0.95 (see Appendix B). The relationship between the time series associated with EOT1 and the other leading modes is also consistent with this

interpretation.

The base point associated with EOT2 is centered at $47.5N$, $160W$ in the North Pacific Ocean, just south of the Alaska Peninsula. Its regression pattern also resembles the results of previous analyses in this chapter. This is particularly true of the main center of action surrounding the base point. Secondary centers are less apparent, but there is some suggestion of a weak negative relationship with the main center and the North Atlantic.

EOT3 is unambiguously Eurasian in character. Based at $65N$, $67.5E$, the pattern is dominated by a large area of positive anomalies, extending to the Pacific coastline to the east, to the crest of the Himalayas to the south, over the Eastern Hemisphere portion of the Arctic Ocean to the north, and into much of eastern Europe to the west. Its size is similar to that of EOT2, and possesses a similar number of weak secondary centers.

Each of the EOTs explains a unique portion of the variance of the DJFM SLP field. This is reflected in Fig. 3.6, which shows the fraction of variance of the SLP field explained by individual grid points after 0, 1, 2, and 3 EOTs have been determined. After the variance associated with EOT1 has been explained, grid points that previously explained over 15% of the domain variance (upper left panel, Fig. 3.6) now explain less than 8% (upper right panel, Fig. 3.6). A similar reduction in variance explained is evident after EOT2 and EOT3 are determined (lower panels, Fig. 3.6). Another way of visualizing the effect of removing

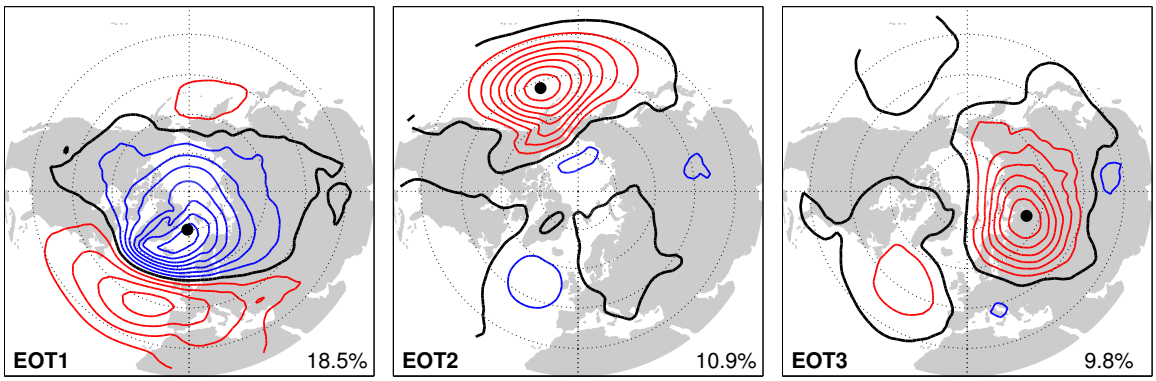

Fig. 3.5: First three spatial patterns (EOT) associated with the Empirical Orthogonal Teleconnection analysis of monthly SLP anomalies. Display is as in Fig 3.1.

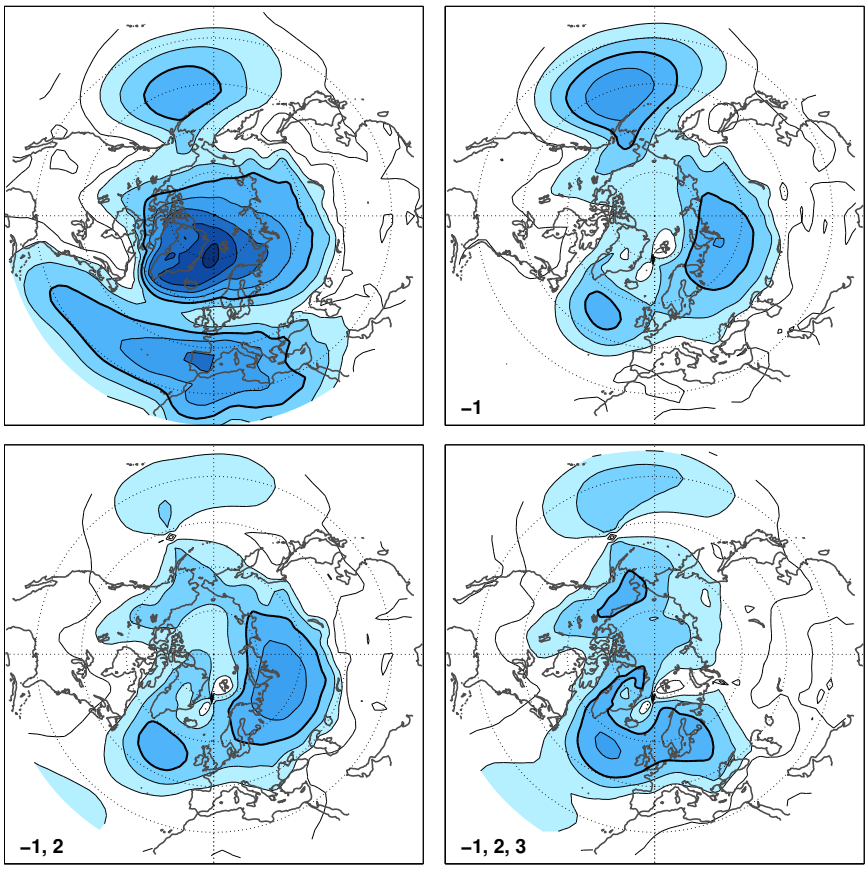

Fig. 3.6: (Top left) Fraction of domain variance explained by single grid points in X. (Top right, Bottom left, Bottom right) Fraction of variance explained in X_r after one, two, and three EOTs have been removed. Contour interval is 2%. Bold reference contour is 10%.

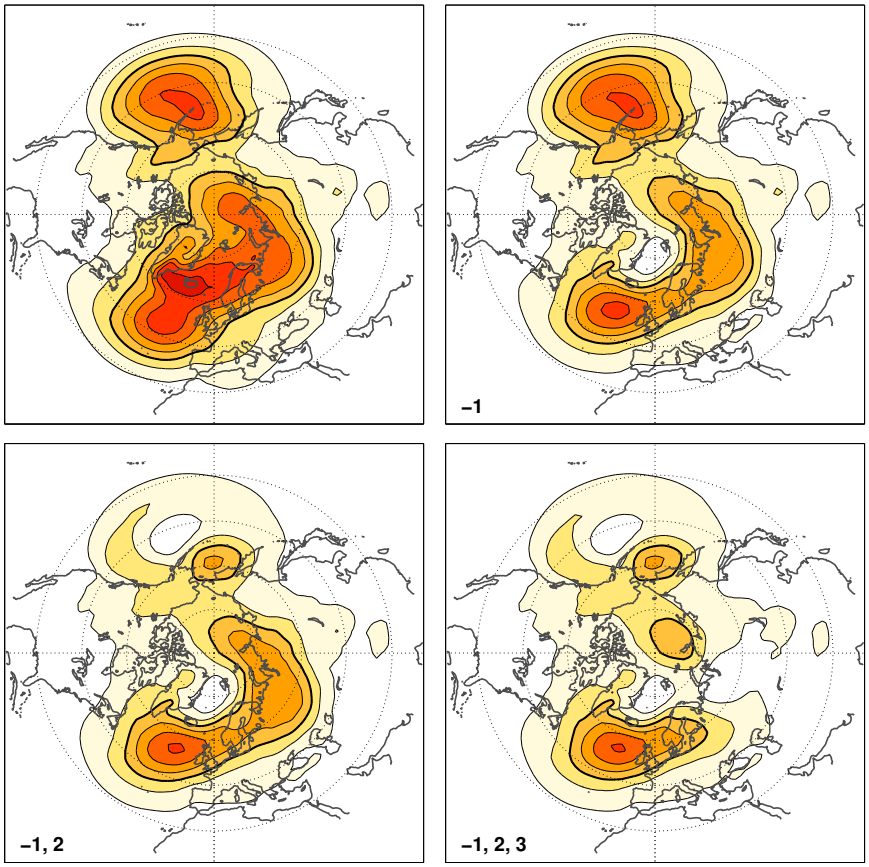

Fig. 3.7: (Top left) Variance of DJFM SLP represented in X. (Top right, Bottom left, Bottom right) Variance of X_r after one, two, and three EOTs have been removed. Contour interval is 10 hPa^2. Bold reference contour is 30 hPa^2.

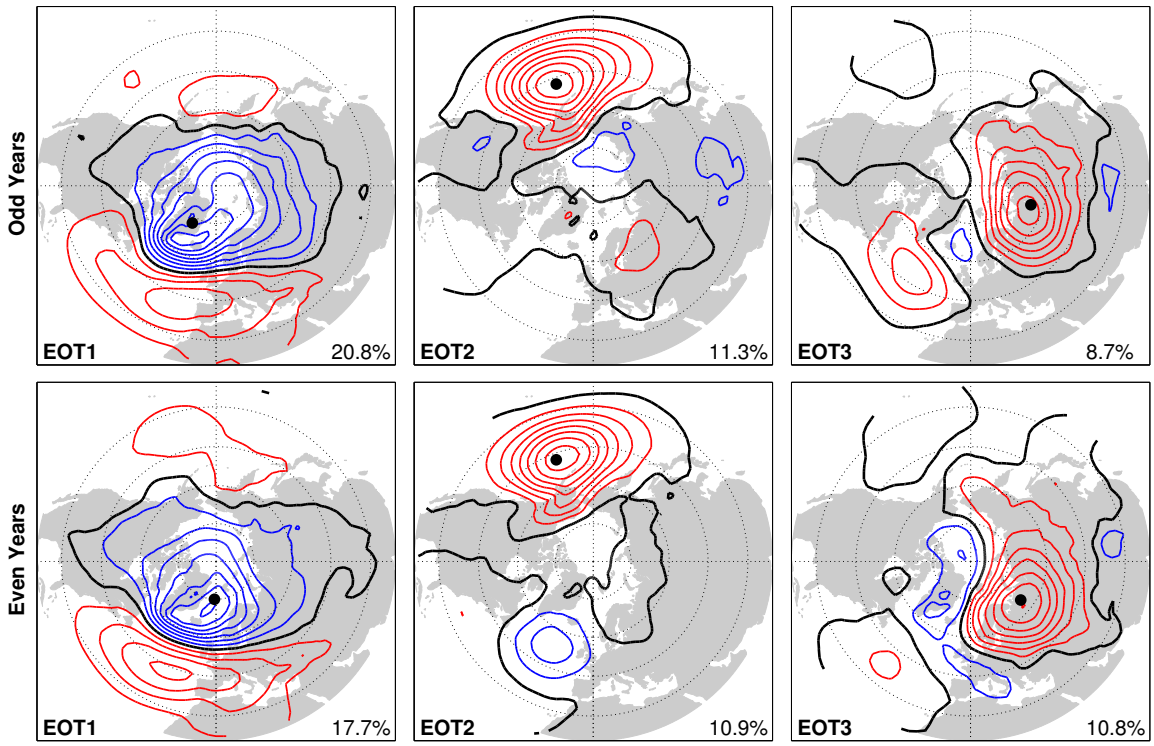

Fig. 3.8: First three spatial patterns (EOT) associated with the Empirical Orthogonal Teleconnection analysis of monthly SLP anomalies from odd and even years of NCEP-NCAR reanalysis data 1958 - 2008. Display is as in Fig 3.1.

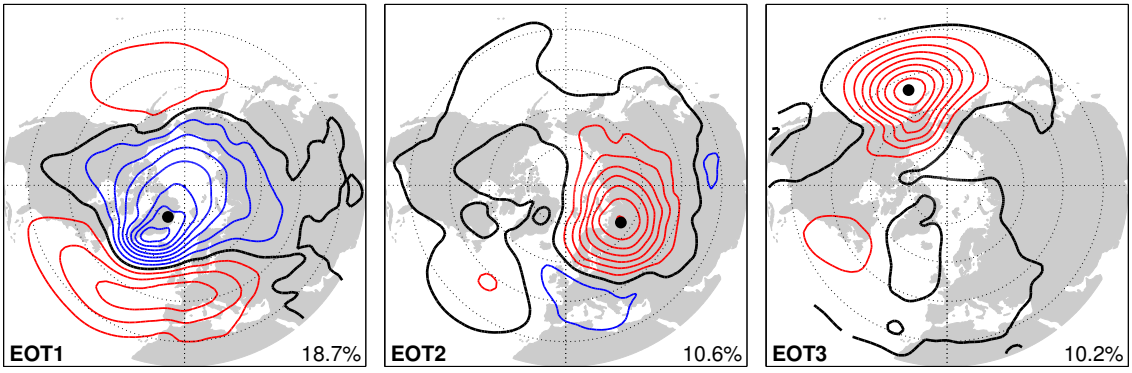

Fig. 3.9: First three spatial patterns (EOT) associated with the Empirical Orthogonal Teleconnection analysis of monthly SLP anomalies from early 20th century reanalysis. Display is as in Fig 3.1.

the influence of EOTs from the total SLP field is shown in Fig. 3.7. It displays variance of the total SLP field (upper left panel) and the variance of the residual SLP field after 1, 2, and 3 EOTs have been determined. After the variance associated with EOT1 has been explained, the maximum of variance in the Atlantic is shifted farther south (upper right panel, Fig. 3.7). The amplitude of the area of variance in the Pacific is decreased after the first two EOTs are removed (lower left panel, Fig 3.7), leaving only a few locations with variance over 10 hPa^2. After all three leading EOTs are regressed out of the original data, residual centers of variance remain over the central North Atlantic, Scandinavia, the central Pacific, and Alaska. Higher EOT modes account for these areas of variance (see Appendix C).

Fig. 3.8 shows the results of EOT analysis applied to two subsets of the original SLP data set, one comprised of odd years and another composed of even years. The similarity between EOTs derived from the two datasets is further evidence of the patterns' robustness. Another verification analysis is shown in Fig. 3.9, which shows the leading three EOTs from an analysis of SLP anomalies derived from the ESRL Early 20th Century Reanalysis product described in Chapter 2. The years included in the ESRL product are 1908 – 1958. EOT1 is characterized by the familiar NAO pattern and explains an amount of variance comparable to EOT1 obtained using the NCEP-NCAR data. In Fig. 3.9, the Eurasian pattern is promoted to EOT2. It explains a larger fraction of variance and has a regression pattern with greater amplitude than EOT3 from the NCEP-NCAR data (right panel, Fig. 3.5). EOT3 from the ESRL Reanalysis (right panel, Fig. 3.9) resembles EOT2 of the NCEP-NCAR analysis, but has a slightly more isotropic primary center of action. The consistency between the patterns shown in Fig. 3.5 and Fig. 3.9 suggest the leading three patterns of NH wintertime SLP variability were robust throughout the twentieth century.

3.5 Summary and Discussion

The series of analyses presented in Chapter 1 illustrate an consistent picture of the dominant three patterns of NH wintertime SLP variability. Setting forth from an EOF analysis of wintertime hemispheric SLP anomalies, complementary objective procedures reproduce patterns previously described in the literature, the AO and PNA. Furthermore, these same

methods suggest the existence of a robust Eurasian, emphasizing the primary center of action in EOF3 Fig. 3.1. Time series and patterns associated with results relevant to Eurasia are summarized in Fig. 3.10.

An area of positive anomalies centered near the axis of the Ural mountains is common to EOF3 of the hemispheric SLP field (Fig. 3.10a), REOF3 of the hemispheric SLP field (Fig. 3.10b), EOF1 of the Eurasian ($30E - 150E$) SLP field (Fig. 3.10c), and EOT3 of the hemispheric SLP field (Fig. 3.10d). The similarity between the EOF3, REOF3, and EOT3 maps is shown quantitatively in Table 3.1 using pattern correlation coefficient, calculated by converting each map into a vector of values and proceeding in the usual fashion of calculating an area-weighted correlation coefficient with reference to its own spatial mean. EOF1 of the Eurasian sector is not considered here, as its loadings are less important outside its own sector.

REOF3 and EOT3 bear the closest resemblance by this measure. This is not surprising, given the domain sensitivity of EOFs (Horel, 1981; Richman, 1986; Dommenget, 2007) and relaxation of spatial orthogonality in the REOF and EOT analyses. Of the three patterns, EOT3 has the highest spatial correlation coefficients with the others.

The time series shown in Fig. 3.10 have general similarities as well. The latter three are characterized by more and larger positive values in the first half of the record and more negative values in the second. Although the time series do not exhibit large trends, they are consistent with a general decrease in SLP across Eurasia during the last 50 years, particularly over NW Russia (Fig. 3.11). The area shows larger negative trends compared with the trends determined by Quadrelli and Wallace (2004) using NCEP-NCAR Reanalysis data 1958–1999. These new negative trends are consistent with the decreased pressure of the wintertime Siberian High discussed by Panagiotopoulos et al. (2005) as well as the negative trend in the index of the Eurasian pattern shown in Fig. 3.10.

The correspondence between the four time series shown in Fig. 3.10 is also documented in terms of their temporal correlation coefficients, displayed in Table 3.2.

The statistics shown in Tables 3.1 and 3.2 support the judgment that EOT3 best represents the dominant mode of Eurasian wintertime SLP variability. It explains a similar fraction of domain variance as the other Eurasian patterns found by the other methods. It

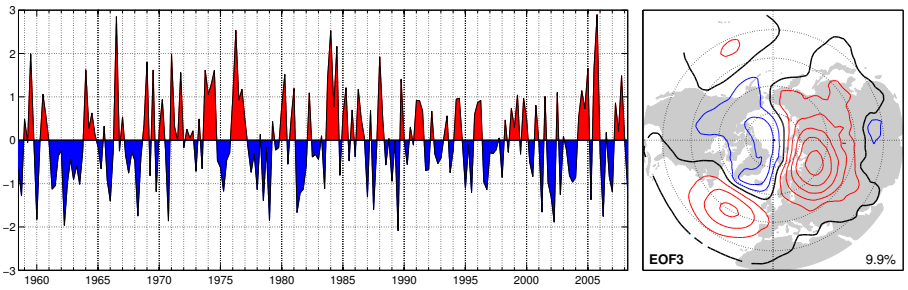

(a)

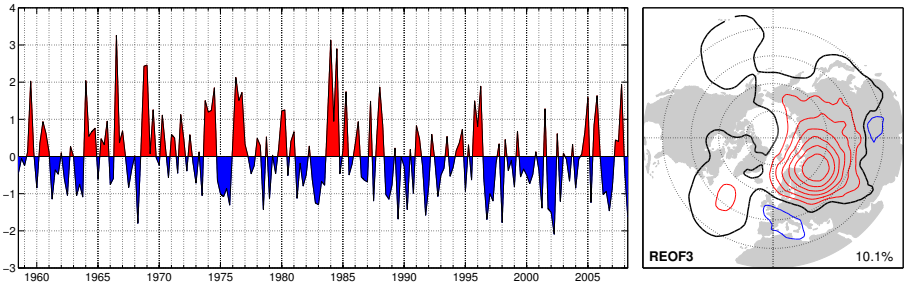

(b)

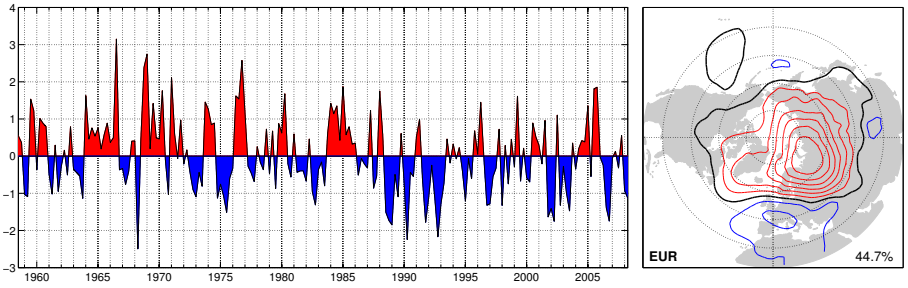

(c)

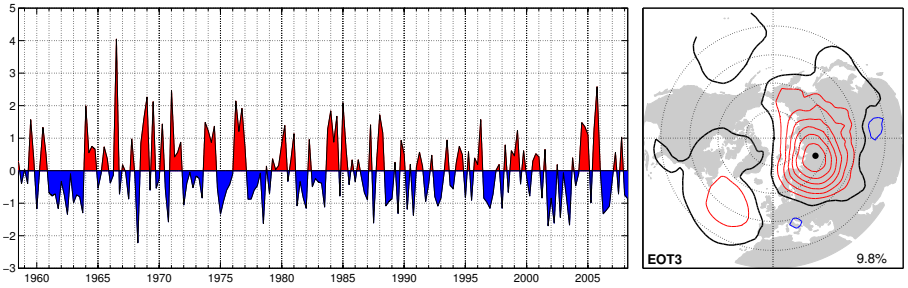

(d)

Fig. 3.10: Normalized time series and regression patterns associated with (a) EOF3, (b) REOF3, (c) EOF1e, and (d) EOT3. Contours as in previously displayed maps. Analyses based on monthly mean DJFM SLP anomalies from NCEP-NCAR reanalysis 1958-2008.

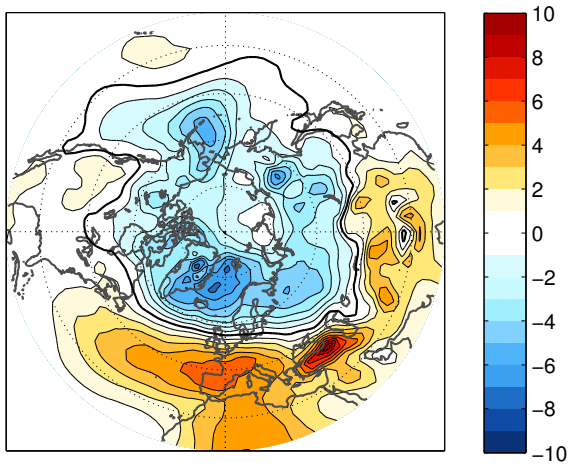

Fig. 3.11: Wintertime (DJFM) SLP trends 1958–2008 (per 50 years) calculated from NCEP-NCAR Reanalysis data. Contour interval 1 hPa; Bold zero contour.

is simpler than the conventional EOF3, but maintains the general shape and extent of the Eurasian center of action in that pattern.

The results presented in this chapter also serve to illustrate the strengths and weaknesses of the methods used to obtain them. EOF analysis produces an efficient representation of the structures that explain the maximum amount of variance in the original SLP data, but has the disadvantage of yielding unphysical patterns shown in the poorly separated, higher order modes. This is particularly true if the patterns observed in nature are not themselves orthogonal. Investigators seeking to analyze the first two EOFs benefit from the fact that the NAO and PNA are quasi-orthogonal. Identification of higher order EOFs with known patterns of climate variability is more problematic.

Rotated principal component analysis has been used to postulate the existence of other regional patterns of climate variability (Horel, 1981; Barnston and Livezey, 1986). When the input eigenvectors are scaled properly, the analysis produces regionally focused patterns with orthogonal rotated principal components. The question of how many eigenvectors to rotate presents a challenge that may be overcome through the use of selection rules and experience. Although rigorous truncation criteria have been developed, the final number of eigenvectors to be rotated is to some extent arbitrary. Furthermore, even though scaling

Table 3.1: Spatial correlation coefficients between respective area-weighted loading patterns of EOF3, REOF3, and EOT3.

	EOF3	**REOF3**	**EOT3**
EOF3	1.00	0.75	0.78
REOF3	0.75	1.00	0.94
EOT3	0.78	0.94	1.00

Table 3.2: Temporal correlation coefficients between respective expansion coefficient time series associated with EOF3, Eurasian sector EOF1 (EOF1e), REOF3, and EOT3.

	EOF3	**EOF1e**	**REOF3**	**EOT3**
EOF3	1.00	0.66	0.81	0.84
EOF1e	0.66	1.00	0.80	0.84
REOF3	0.81	0.80	1.00	0.84
EOT3	0.84	0.84	0.84	1.00

eigenvectors by the square root of their eigenvalues helps to stabilize solutions with respect to the number of input eigenvectors, higher order rotated eigenvectors do not necessarily converge to such invariant solutions (Hannachi et al., 2006).

Performing EOF analysis on subsets of the larger domain can reveal patterns that are separated in space and confirm the regionalized results of rotated EOF analysis. However, nature does not always divide itself so readily. While the divide between the AO and the PNA can be demonstrated by splitting the hemisphere in two across $90W$ and $90E$ (Rennert, 2007), fitting more than two discrete patterns onto the hemisphere in an orthogonal manner proves to be a challenge. Over Eurasia, this proves to be a problem where the NAO and the Eurasian pattern characterized by EOT3 overlap. For example, a portion of the variance over the Baltic Sea is explained by the NAO while another is explained by EOT3. The partial obliqueness of these patterns, as well as the near orthogonality of the first Atlantic and Pacific modes can be demonstrated by examining the correlation coefficients between the principal components associated with the leading EOFs from the sector analysis (Table 3.3).

The Eurasian and Pacific modes are also essentially orthogonal. While sectoral EOF analysis can provide support for other results, it is difficult to justify as the sole means of analysis.

Tables 3.4 through 3.6 show the relationship between pairs of EOFs and REOFs, EOFs and EOTs, and REOFs and EOTS, in terms of the fraction of variance shared by both

Table 3.3: Temporal correlation coefficient for time series associated with the leading EOFs from the sector analysis.

	EOF1a	**EOF1e**	**EOF1p**
EOF1a	1.00	0.42	0.17
EOF1e	0.42	1.00	0.09
EOF1p	0.17	0.09	1.00

Table 3.4: Temporal variance of SLP EOFs explained by SLP REOFs.

	EOF1	**EOF2**	**EOF3**	**EOF4**	**EOF5**	**EOF6**
REOF1	0.67	0.01	0.13	0.09	0.03	0.00
REOF2	0.05	0.55	0.00	0.00	0.24	0.00
REOF3	0.12	0.00	0.66	0.00	0.01	0.01
REOF4	0.00	0.00	0.02	0.04	0.46	0.14
REOF5	0.03	0.24	0.02	0.39	0.00	0.28
REOF6	0.01	0.06	0.03	0.28	0.10	0.27

Table 3.5: Temporal variance of SLP EOTs explained by SLP EOFs.

	EOT1	**EOT2**	**EOT3**	**EOT4**	**EOT5**	**EOT6**
EOF1	0.77	0.01	0.09	0.01	0.01	0.02
EOF2	0.01	0.74	0.01	0.14	0.02	0.01
EOF3	0.04	0.01	0.71	0.01	0.05	0.02
EOF4	0.03	0.01	0.05	0.01	0.50	0.25
EOF5	0.01	0.14	0.01	0.52	0.02	0.18
EOF6	0.02	0.01	0.01	0.22	0.24	0.32

Table 3.6: Temporal variance of SLP EOTs explained by SLP REOFs.

	EOT1	**EOT2**	**EOT3**	**EOT4**	**EOT5**	**EOT6**
REOF1	0.66	0.00	0.01	0.04	0.01	0.00
REOF2	0.01	0.76	0.00	0.01	0.00	0.05
REOF3	0.02	0.00	0.71	0.00	0.03	0.00
REOF4	0.00	0.01	0.01	0.87	0.01	0.00
REOF5	0.03	0.00	0.01	0.01	0.76	0.00
REOF6	0.01	0.06	0.00	0.00	0.01	0.85

modes. A modest relationship is evident between the first three EOFs and REOFs, indicated by r^2 values greater than 0.5. Beyond the third mode, it is unclear whether specific EOFs and REOFs correspond to one another (Table 3.4). The relationship between the first three EOFs and EOTs is stronger than for EOFs and REOFs (Table 3.5). The close correspondence of REOFs and EOTs is shown in Table 3.6, which documents r^2 values greater than 0.66 between the first six modes. This result provides further evidence that other reproducible patterns exist.

EOT analysis has been demonstrated to be the best representation of the third pattern of NH wintertime climate variability. It unambiguously extracts the three leading patterns shown, plus an additional four or five that are shown in Appendix C. Whereas the morphology of patterns depicted by REOF analysis can change when the number of input eigenvectors is varied, the EOTs are completely determined by the data. EOT also competes with EOF and REOF analysis in terms of explaining comparable fractions of domain variance in the third mode. Table 3.7 shows variance explained and cumulative variance explained for the leading three EOFs, REOFs, and EOTs. The EOF method clearly explains the most cumulative variance. The leading three REOFs and EOTs explain a similar amount of cumulative variance.

The importance of interpreting higher order modes carefully is illustrated by some confusion in the literature. For example, Hannachi et al. (2006) mistakenly liken their REOF3 to the Eurasian type-1 pattern of Barnston and Livezey (1986), also known as the Scandi-

Table 3.7: Individual and cumulative variance explained by EOF, REOF, and EOT modes 1-3.

	EOF		**REOF**		**EOT**	
#	Indiv.	Cumul.	Indiv.	Cumul.	Indiv.	Cumul.
1	22.8	22.8	17.9	16.4	18.5	18.5
2	12.5	35.3	10.2	28.1	10.9	29.4
3	9.9	45.2	10.1	38.2	9.8	39.2

navian Pattern (SCA) (Bueh and Nakamura, 2007). While REOF3 does resemble SCA, the current analysis puts REOF3 in context, showing that it corresponds better with EOT3. In fact, the Scandinavian Pattern is likely related to DJFM EOT5 (Appendix C). Clearly, there is some value in being able to interpret patterns beyond those that pass the North et al. (1982) test. Some investigators have attempted to do so relying on a single method (Hannachi et al., 2006). In this chapter we have attempted to synthesize the results derived from four different methods, building on evidence from one analysis with complementary results from others. We have used the Eurasian pattern of variability suggested by EOF3 of DJFM SLP as an example. Although this pattern has been referenced previously in the literature (Overland and Wang, 2005; Hannachi et al., 2006; Dommenget, 2007; Hannachi et al., 2007), it has not been thoroughly investigated.

In subsequent chapters, EOT3 will be used to represent the robust Eurasian pattern in the SLP field identified in this chapter.

Chapter 4

THE STRUCTURE OF THE EURASIAN PATTERN

4.1 Introduction

The existence of a Eurasian pattern of NH wintertime SLP variability has been established via the techniques described in Chapter 1. Using EOT3 and its corresponding time series as the optimal definition of the dominant Eurasian pattern, this chapter seeks to describe the structure of its signature throughout the depth of the troposphere and lower stratosphere. Linear regression will be the primary tool utilized in service of this goal, making use of geopotential height, temperature, and wind data from the NCEP Reanalyses.

The robustness of the signature of this pattern will be demonstrated by showing that a similar pattern can be recovered by performing EOT analysis on fields other than SLP and then regressing the SLP field on the expansion coefficients of the pattern that matches the Eurasian mode.

The seasonality of the leading modes of NH SLP variability will be explored by performing EOT analysis on consecutive three-month groups of SLP data.

4.2 Surface Fields

EOT3 of NH SLP (Fig. 3.5) is the dominant pattern of wintertime climate variability over Eurasia. It is characterized by a single center of action centered at $65N$, $67.5E$, just south and east of the island of Novaya Zemlya. Weak secondary centers are present over the North Atlantic Ocean and the crest of the Himalayas.

Figure 4.1 shows the patterns obtained by regressing surface air temperature (SAT) and 1000-500 hPa thickness onto the time series associated with EOT3. The regression patterns show the fluctuations in those fields associated with a one standard deviation anomaly in the standardized expansion coefficient time series.

The SAT field associated with the positive polarity of the EOT3, with abnormally high SLP over central Russia, is characterized by cold anomalies over most of Eurasia north of the Himalayas and warm anomalies off the Arctic coast in the Barents and Kara seas. The zonally elongated band of cold anomalies lies just to the north of the topographic barrier created by the Altai, Sayan, and Tien Shan mountain ranges of Northern Eurasia (green line, left panel, Fig. 4.1). As the northerly flow impinges on the mountains, it is deflected westward toward the Caucasus. To the east of the Himalayas, the negative temperature anomalies spill southward into China. The cold and warm anomalies are consistent with anomalous northerly and southerly surface winds, respectively (center panel, Fig. 4.1).

The warm anomalies over the Arctic are enhanced where the anomalous westerly flow encounters the mean sea ice edge (blue line, left panel, Fig. 4.1).

In general, EOT3 is associated with a dipole pattern in SAT with one center located over the Eurasian continent and the other over the Arctic ocean. In this sense, the pattern projects strongly on the cold ocean-warm land (COWL) pattern described by Wallace et al. (1995) and Thompson et al. (2009). The COWL pattern is related to dynamical contributions to fluctuations in hemispheric-mean temperature, due to the difference in heat capacity

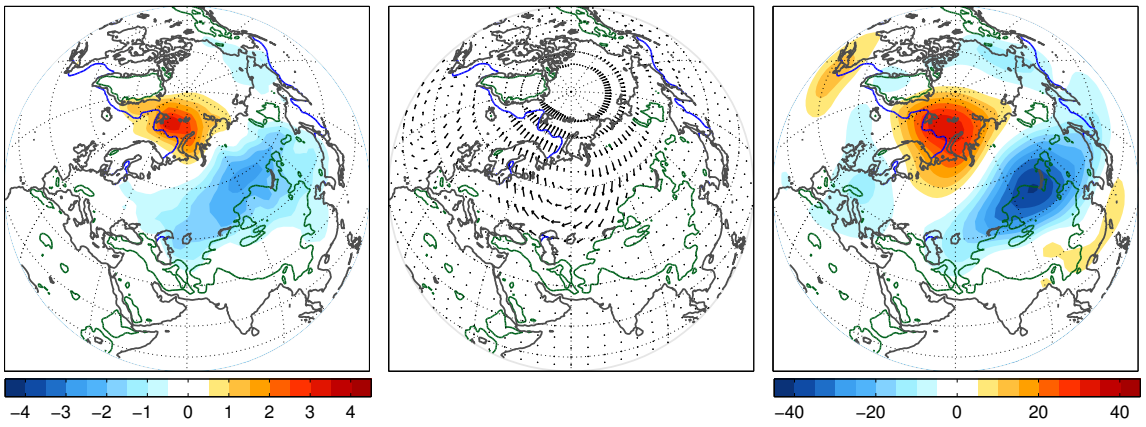

Fig. 4.1: Regression maps for (left panel, °C) SAT, (center panel) surface winds, and (right panel, m) $1000-500$ hPa thickness based on the time series associated with EOT3, DJFM $1958-2008$. In left panel, 1000 m contour line is plotted in green and mean DJFM sea ice extent is plotted in blue. Color scales are in units of °C and m, respectively, per standard deviation of the EOT3 time series.

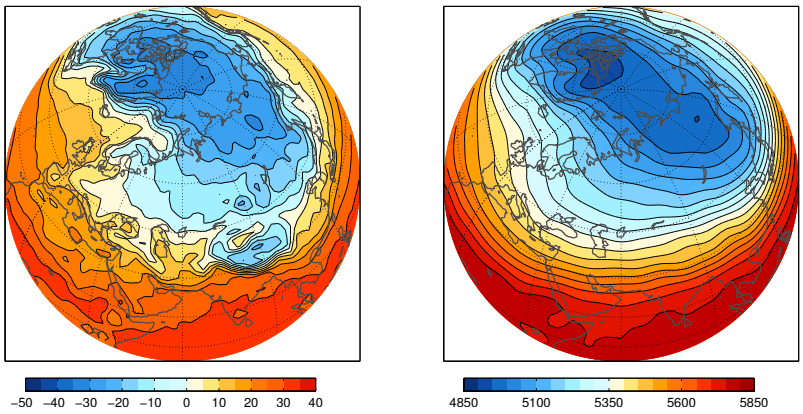

Fig. 4.2: Climatological wintertime (DJFM) SAT (left panel) and 1000 − 500 hPa thickness.

of land and ocean. Having much less thermal inertia, the land equilibrates with changes in overlying air masses more quickly than the ocean. During periods of strongly zonal flow, the land tends to be anomalously warm compared to the ocean, boosting the hemispheric mean temperature. Wallace et al. (1995) defined the COWL pattern as the regression of T^*, the spatially varying surface air temperature produced by subtracting the hemispheric mean temperature from all grid points at all times, onto the hemispheric mean temperature time series. Thompson et al. (2009) adapt the earlier methodology to the SLP field, regressing it onto a land minus ocean temperature difference time series, $T_{NHLand-NHSST}$. This produces a SLP pattern that contributes most strongly to opposite phase SAT anomalies over land and ocean. Of the first 10 EOTs, EOT3 has the strongest temporal correlation ($r = -0.44$) between itself and $T_{NHLand-NHSST}$. EOT1 and EOT2 have correlations on the order $r = 0.3$, and also contribute toward explaining dynamical contributions to global mean temperature. This suggests that while no single pattern dominates, EOT3 may play an important role in modulating the hemispheric mean temperature.

A pattern similar to the SAT regression is observed in the regression map of 1000-500 hPa thickness onto EOT3 (right panel, Fig. 4.1). This indicates the influence of EOT3 on temperature throughout the lower troposphere. The primary centers of action in the thickness regression map shown in the right panel of Fig. 4.1 may be understood in terms of the advection of the climatological temperature and thickness gradients (Fig. 4.2) by

the anomalous flow. In both areas of large anomalies, the climatological gradients of SAT and thickness (not shown) are aligned perpendicular to the anomalous wind (center panel, Fig. 4.1).

4.3 Upper Level Fields

Figure 4.3 shows regression maps of SLP and three upper level geopotential height fields onto the time series associated with EOT3. As height increases, the signature associated with EOT3 of SLP becomes more wavelike. The pattern at 700 hPa (left panel, Fig. 4.3) is most congruent with the EOT3 basis pattern defined by the SLP analysis. Most of its amplitude is contained in the primary center of action, centered $2-3$ degrees of latitude northward of the surface maximum. Relative to the primary center, the secondary centers at upper levels over the Tibetan plateau and North Atlantic are slightly stronger than the corresponding anomalies at the surface. Weak negative secondary centers are also observed over central Europe and the Beaufort Sea.

At 300 hPa (center panel, Fig. 4.3), near the tropopause, geopotential height anomalies are larger, approaching 90 m in the primary center of action over northwestern Russia. The primary anomaly center shifts slightly northward between the surface and 700 hPa; above 700 hPa, it remains centered over the southern end of Novaya Zemlya. The secondary centers increase both in amplitude and areal extent, with the North Atlantic and Tibetan centers becoming the most prominent.

The 50 hPa (right panel, Fig. 4.3) regression pattern illustrates the local response of the stratosphere to EOT3. Centers of action at 50 hPa are weaker than at the tropopause level. In contrast to the leading mode of hemispheric variability, the NAM, EOT3 does not project strongly onto the leading mode of variability of the stratospheric circulation (Thompson and Wallace, 1998; Thompson et al., 2000), suggesting that it has a minimal influence on the strength of the polar vortex.

Figure 4.4 shows the signature of EOT3 in zonal wind at the 300 hPa level. When EOT3 is in its positive polarity, the westerly flow across the northern tier of Eurasia is slowed. These anomalies have only a small influence on the strength of the jet, which typically exhibits peak velocities in excess of 60 ms^{-1}.

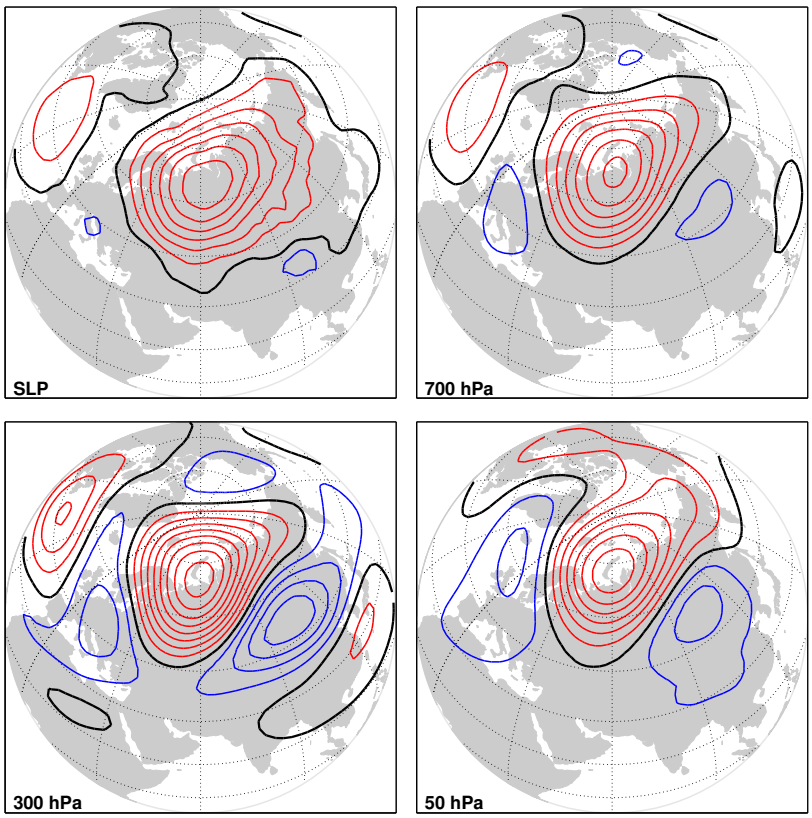

Fig. 4.3: Regression maps for geopotential height for (left panel) 700 hPa, (center panel) 300 hPa, and (right panel) 50 hPa based on the time series associated with EOT3 of monthly-mean SLP data, DJFM 1958 - 2008. Contour interval is 10 m per standard deviation of the EOT3 time series for all three panels. Zero line is indicated in bold black.

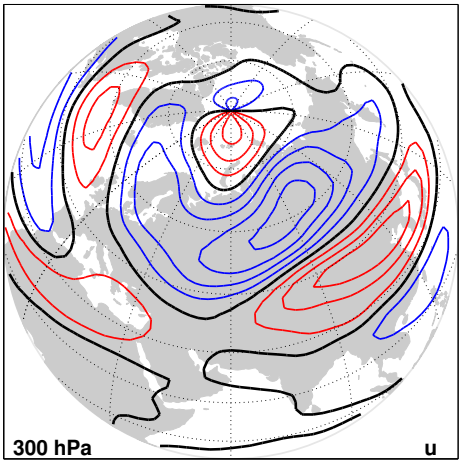

Fig. 4.4: Regression map for u winds at 300 hPa based on the time series associated with EOT3, DJFM 1958 - 2008. Contour interval is 1 ms^{-1} per standard deviation of the EOT3 time series, respectively. Zero line is indicated in bold black.

The vertical structure of the signature associated with EOT3 can be described in terms of the superposition of a deep equivalent barotropic component extending from the surface to the lower stratosphere and a shallow baroclinic component confined to the lower troposphere. A NW-SE cross section through the pattern is shown in Fig. 4.5. The equivalent barotropic structure is evident in the nearly vertical stacking of geopotential height anomalies in the mid to upper troposphere and approximately parallel orientation of the temperature gradient to the height gradient. This is similar to other large scale patterns of climate variability, including the AO/NAM (Thompson and Wallace, 1998, 2000) and Western Pacific / North Pacific Oscillation (WP/NPO) (Linkin and Nigam, 2008). In contrast to the aforementioned patterns, the baroclinic component of EOT3 is particularly striking, with the strongest temperature anomalies at the Earth's surface located well to the north of the corresponding features in the geopotential height field.

Hsu and Wallace (1985) emphasized the contrast between patterns of geopotential height fluctuations at the surface and mid-troposphere over the continents as represented by one point correlation maps of SLP and 500 hPa geopotential height. Whereas the patterns at the two levels tend to be similar over the ocean basins and periphery of the continents, the

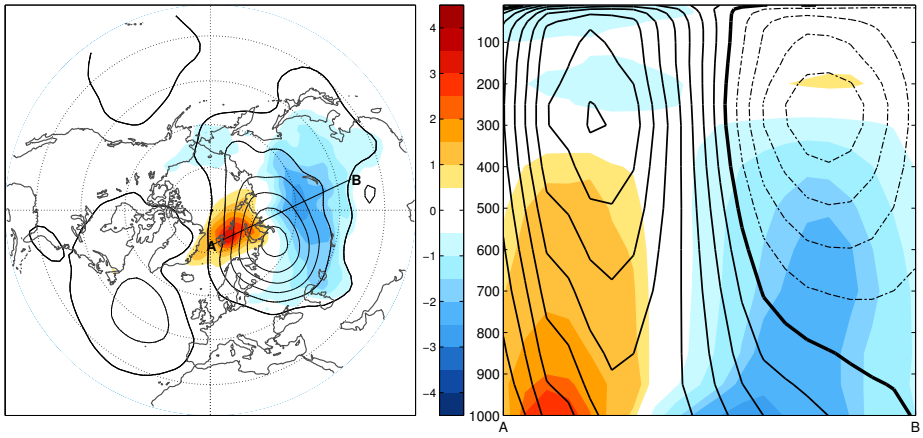

Fig. 4.5: EOT3 geopotential height (contours) and temperature (shading) regressions along transect indicated in left panel, months DJFM, 1958 - 2008. Positive (negative) contours are solid (dash-dot), every 10 m per standard deviation anomaly of the EOT3 time series. Bold contour indicates the zero line. Shading convention is the same, except for units of °C.

authors drew attention to the dissimilarity in the continental interiors, particularly around the major NH mountain ranges, the Himalayas and Rockies. The character of EOT3 is broadly consistent with the results of Hsu and Wallace. The western portion of the pattern, closest to the North Atlantic Ocean, varies little with height; its eastern portion, nearest the Tibetan plateau, exhibits a pronounced transition from weak positive anomalies at surface to strong negative anomalies at upper levels. Furthermore, the spatial scale of the surface center of action is larger than that of the centers observed aloft, a common feature of the baroclinic patterns described by Hsu and Wallace.[1] Another aspect of their results reflected here is the position of the center of the positive SLP anomalies relative to the negative SAT anomalies over the continent, exhibiting a quadrature relationship in the meridional direction.

[1]Hsu and Wallace (1985) used the term "baroclinic structure" to refer to patterns with distinctly different patterns at the surface and upper levels. This is not to be confused with baroclinic instability.

4.4 Comparison with EOTs of other fields

Although our EOT analysis is based on the SLP field, further investigation suggests that similar patterns can be recovered from EOT analysis of other fields. Figure 4.6 shows the first three EOTs of 500 hPa geopotential height, $1000-500$ hPa thickness, and SAT. EOT3 of 500 hPa geopotential height and $1000-500$ hPa thickness bear a marked similarity to the regression maps for those fields regressed on EOT3 of SLP. Spatial correlation between the patterns support this impression ($r = 0.93$ and 0.76, respectively). For the thickness field, the EOT method emphasizes the main center of action, whereas regression on EOT3 of SLP divides the amplitude more evenly between the two poles of the dipole. Temporal correlations also attest to the relationship between the EOTs shown in Fig. 4.6 and EOT3 of SLP time series ($r = 0.88$ and 0.53, respectively). Other results (not shown) confirm this relationship at geopotential heights up to 200 hPa.

Table 4.1 shows a measure of the strength of the relationship between EOT modes at the surface and EOT modes at 500 hPa. The explained variances shown in the table are calculated by squaring the correlation between the time series associated with the respective surface and upper level EOTs. Each of the first six EOTs of SLP has a corresponding EOT of 500 hPa geopotential height that it shares a large fraction of variance with. This indicates that the patterns of variability depicted by EOTs may be consider to have a robust three-dimensional structure throughout the lower troposphere.

In the EOTs of SAT (Fig. 4.6c), a pattern of Eurasian variability appears as EOT1. In contrast to the previous cases in which the EOT maps resemble regressions of those fields on their SLP counterparts, the SAT EOTs appear to break up the centers of action seen in the SAT regression on EOT3 of SLP into separate centers over the interior of Eurasia and Svalbard. This is likely due to the EOT methodology's use of one-point correlation maps to define EOT modes. Apparently SAT over the Barents Sea is only weakly negatively correlated with SAT over the Eurasian supercontinent. Furthermore, enough of the variability in the Barents Sea region is explained by nearby grid points to warrant its emergence as a separate mode. There is a moderate temporal correlation between EOT2 of SAT and EOTs 1 and 3 of SLP ($r = -0.44$ and -0.39, respectively). EOT1 of SAT, however, is more

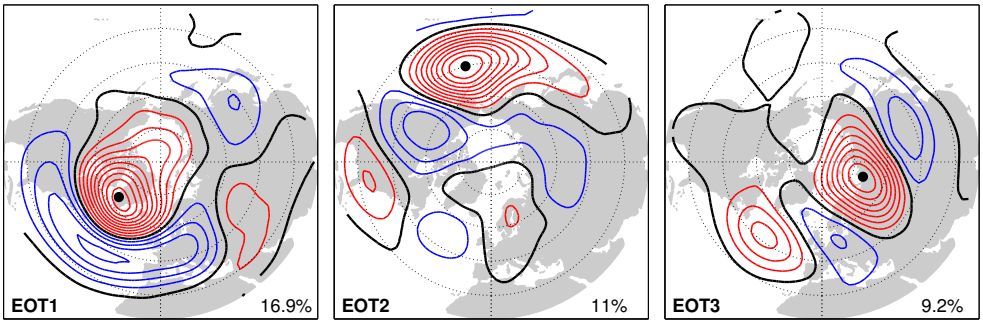

(a) 500 hPa Geopotential Height; Contour interval 10 hPa.

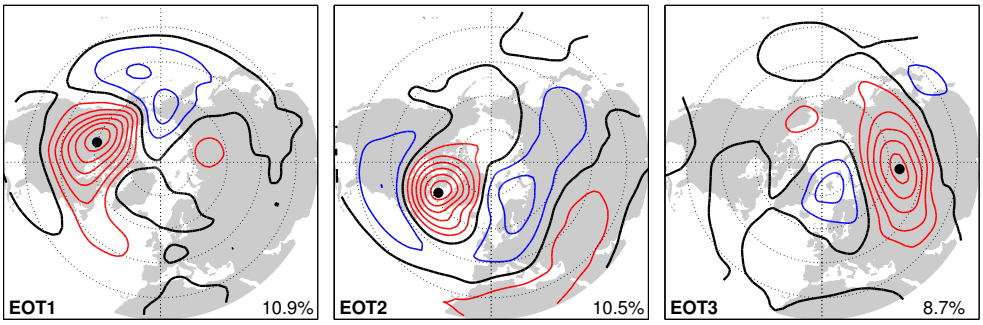

(b) 1000-500 hPa Thickness; Contour interval 10 m.

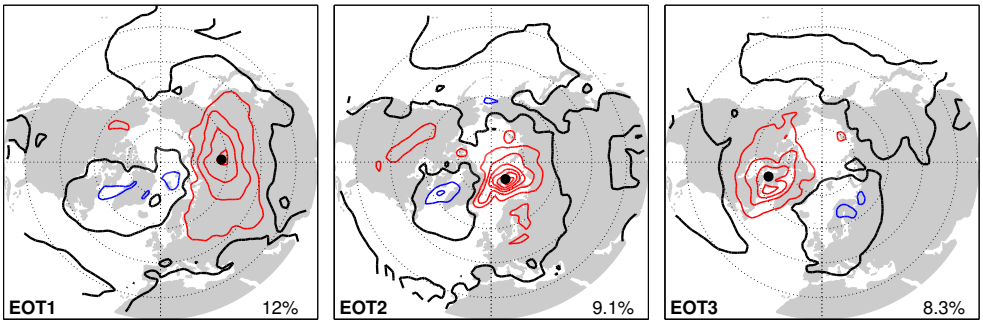

(c) Surface Air Temperature; Contour interval 1°C.

Fig. 4.6: First three EOTs of three fields based on monthly mean DJFM anomalies from NCEP-NCAR reanalyses 1958-2008.

Table 4.1: Temporal variance of 500 hPa geopotential height EOTs explained by SLP EOTs.

Z↓ / SLP→	**EOT1**	**EOT2**	**EOT3**	**EOT4**	**EOT5**	**EOT6**
EOT1	0.70	0.00	0.00	0.06	0.00	0.01
EOT2	0.00	0.93	0.00	0.00	0.00	0.00
EOT3	0.00	0.00	0.78	0.01	0.00	0.01
EOT4	0.05	0.00	0.01	0.66	0.01	0.02
EOT5	0.02	0.00	0.03	0.02	0.00	0.78
EOT6	0.00	0.00	0.00	0.02	0.72	0.01

strongly correlated with EOT3 of SLP ($r = -0.57$).

EOT3 of 500 hPa heights, EOT3 of thickness, and EOT1 of SAT resemble the regression maps produced by projecting each field onto the standardized expansion coefficient time series of EOT3 of SLP. This strong correspondence reinforces the notion of a preferred pattern of Eurasian variability set forth in Chapter 3. In the case of 500 hPa geopotential height and $1000-500$ hPa thickness, the signature associated with the Eurasian pattern appears as the third EOT pattern of hemispheric variability. The broad SAT anomaly associated with the signature of the Eurasian pattern in SAT is evident in the leading mode of hemispheric SAT variability. Together, these EOTs depict aspects of the same variability as EOT3 of SLP. Hence, similar patterns emerge as EOTs when the analysis is performed on a variety of different fields.

Figure 4.7 shows three of the aforementioned EOTs, EOT3 of $1000-500$ hPa thickness, EOT1 of SAT, and EOT2 of SAT, as well as the SLP pattern that corresponds to each. The latter is obtained by regressing SLP anomalies onto the standardized expansion coefficient time series for each of the respective EOTs. The SLP pattern associated with EOT3 of the thickness field projects strongly onto EOT3 of SLP. This is consistent with the thickness anomalies expected from the temperature advection by the anomalous geostrophic circulation implied by EOT3 of SLP.

The SLP patterns associated with EOT1 and EOT2 of SAT shown in the lower center

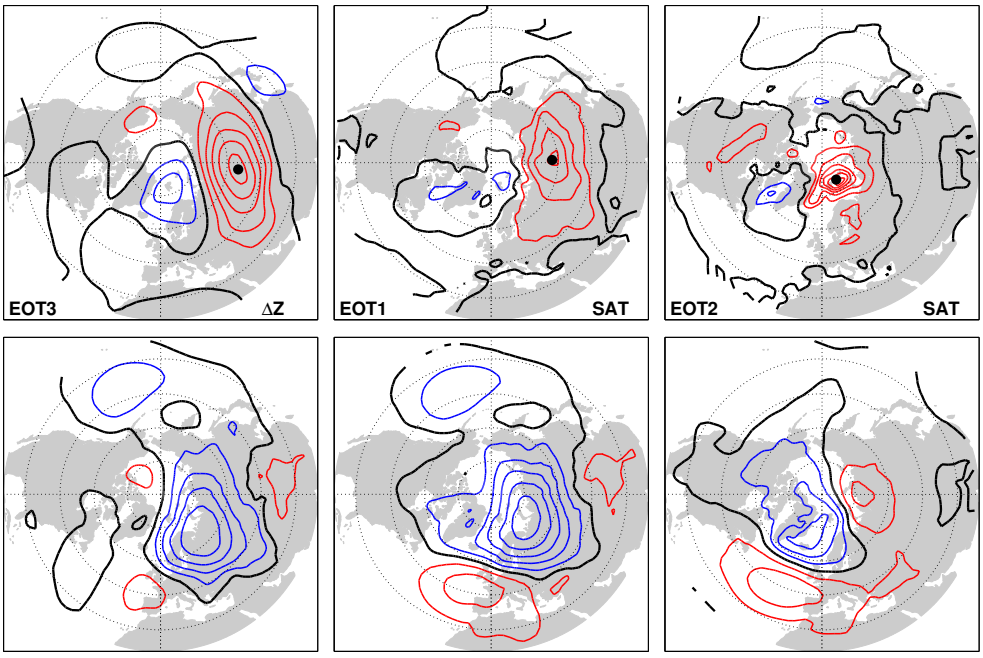

Fig. 4.7: EOT and corresponding SLP pattern obtained by regressing SLP anomalies onto the standardized expansion coefficient time series of the respective EOT, shown for EOT3 of 1000-500 hPa thickness, EOT1 of SAT, and EOT2 of SAT. Contour interval (upper panels) as in Fig. 4.6 and (lower panels) 1 hPa.

and lower right panels of Fig. 4.7 provide further evidence in support of our interpretation that the various patterns are dynamically consistent. Given the similarity of EOT1 of SAT and EOT3 of $1000 - 500$ hPa thickness, it is not surprising that the SLP patterns bear a strong resemblance to one another. When SAT over the continent is anomalously high, the SLP is lower than normal. This implies anomalous southerly winds over central Eurasia down the climatological temperature gradient, justifying the high SAT. The SLP pattern associated with EOT2 of SAT has components that resemble both EOT1 and EOT3 of SLP. The dipole over the North Atlantic is reminiscent of the NAO and the pressure gradient that lies between Scandinavia and Svalbard is oriented in the same direction as the corresponding portion of the Eurasian pattern. When SAT is unusually high over Svalbard, a strong southerly component of the anomalous flow advects warmer air northward over this region.

4.5 EOT analysis applied to other seasons

Now that the wintertime structure of EOT3 has been documented, it is worth asking whether its signature varies in character throughout the year. To answer this question, EOT analysis was applied to twelve groups of data consisting of three monthly-mean anomalies centered on each calendar month. For example, the January analysis is comprised of data for the months DJF. Results are presented in Fig. 4.8. In selecting which EOT to show, I chose the one with the base point closest to the base point of EOT3 of DJFM SLP.

Patterns resembling the DJFM pattern are prominent throughout the cold season and extremely weak and localized in the summer. The amount of variance explained by a Eurasian pattern follows a progression which reaches a maximum in late autumn (November, 12.8%) and another in early spring (March, 10.1%). The structure of the pattern varies throughout the year, falling into three categories. During the warm season, from May to August, the pattern is characterized by a small, isotropic SLP anomaly over Northeastern Scandinavia. During winter, from December to February, the pattern acquires the familiar morphology described throughout this thesis: a broad, zonally elongated SLP anomaly centered over northwestern Russia and extending out to the east. During autumn, the pattern

changes from the summertime signature, growing in amplitude and area, but maintaining the isotropic characteristic of the summertime anomaly. The springtime pattern is more restricted to the region west of $90°E$.

Figure 4.8 suggests that the wintertime pattern described earlier is present during other seasons, particularly the months in the interval from early autumn to late spring. The 300 hPa regression maps shown in Fig. 4.9 offer an upper tropospheric perspective on the seasonality of the patterns. The pattern has only a weak, localized upper level signature during summer, but exhibits a distinct wave train extending from the North Atlantic over the Eurasian continent starting in early autumn. This feature increases in breadth and amplitude toward midwinter and shifts westward in late winter and spring.

4.6 Summary

Here we have examined the three dimensional signature of the leading pattern of Eurasian wintertime SLP variability exemplified by EOT3 of SLP. Regression maps of surface and upper air fields indicate that the pattern is mainly confined to the troposphere and lower stratosphere. EOT3 of SLP is comprised of a broad anomaly stretching from northwestern Russia to the Pacific coastline. It has a wavelike upper level signature. The pattern is situated over the Eurasian supercontinent well to the north of the jet stream. EOT3 does not project strongly onto the stratospheric polar vortex; it influences the flow only locally over northern Eurasia. Although the geopotential height fluctuations are strongest near the tropopause level, the strongest temperature anomalies associated with the Eurasian pattern appear near the surface, over the continent and the eastern Arctic seas. The distinction between the geopotential height and temperature patterns highlights the baroclinic structure of the EOT3 pattern, in comparison to EOTs 1 and 2, in which the equivalent barotropic component is more dominant. EOT3 is unique for its position over the continent and its strong influence on SAT. The Eurasian pattern was shown to have a notable relationship with global mean temperature, likely due to the same physical mechanism associated with the COWL pattern.

EOT analysis applied to other fields yields patterns similar to those in the aforementioned regression maps, and the SLP patterns associated with the leading EOTs of SAT

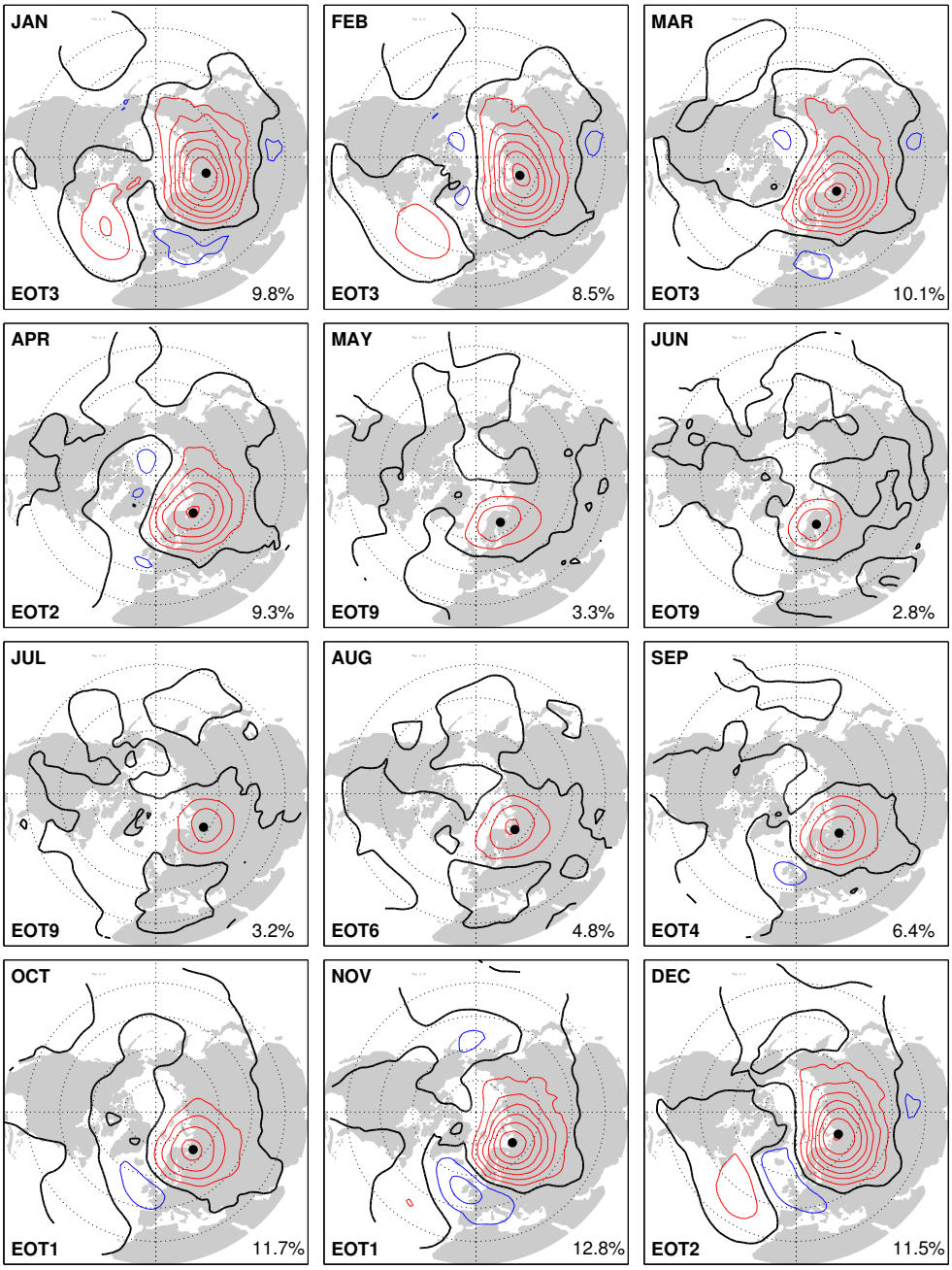

Fig. 4.8: Eurasian pattern as exemplified in EOT analysis of consecutive groups of three calendar month data throughout the year. For example, the DEC analysis is performed using monthly mean anomalies from NDJ. The EOT rank corresponding to the pattern is shown in the lower left corner of each panel. Fraction of domain variance explained is displayed in the lower right corner of each panel.

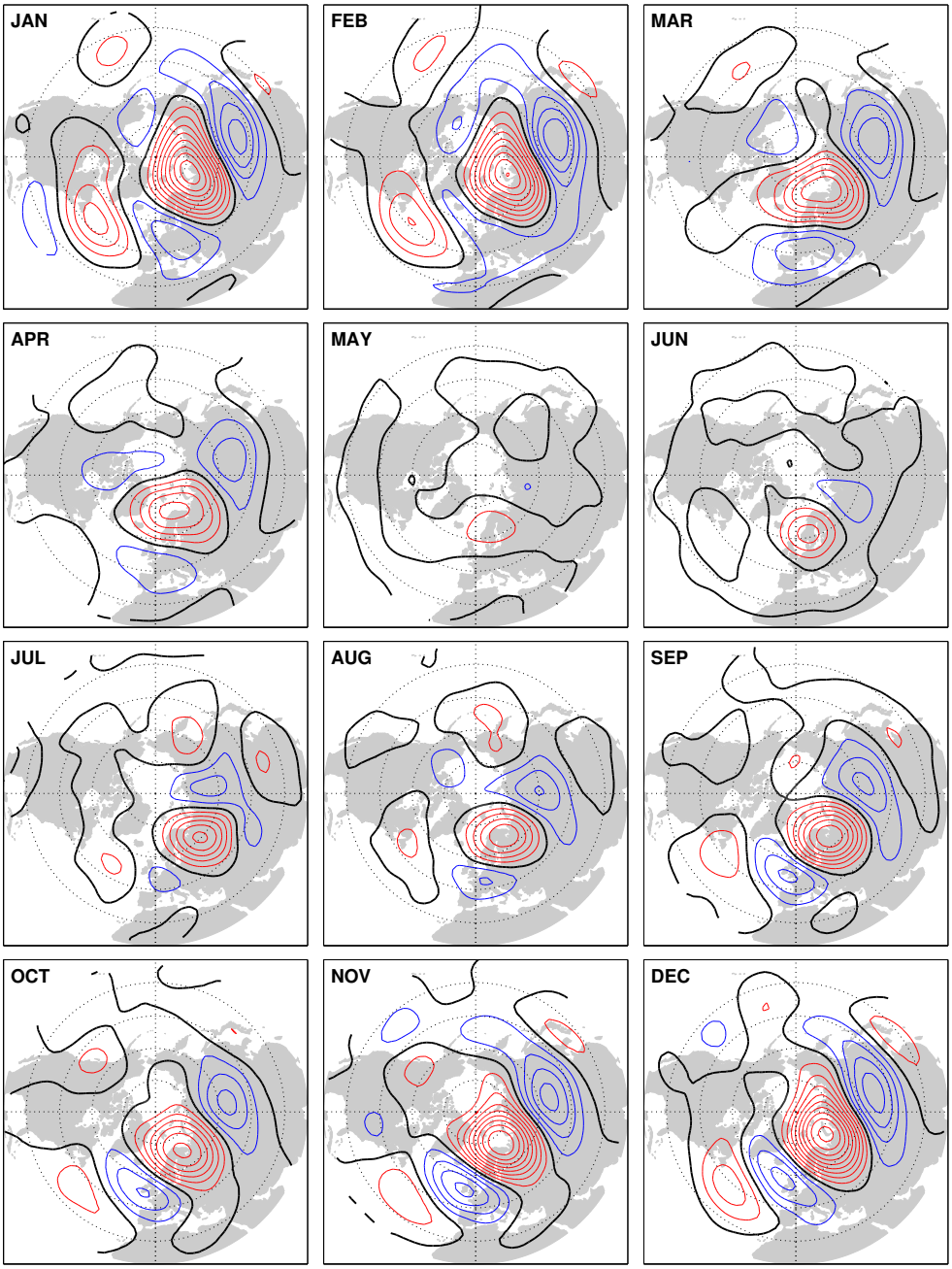

Fig. 4.9: Same as in Fig 4.8, but regressions of 300 hPa field onto the corresponding standardized expansion coefficient time series.

and $1000 - 500$ hPa thickness resemble EOT3 of SLP. The close correspondence between these attest to the robustness of the patterns associated with EOT3 of SLP.

The structure of the Eurasian pattern presented in Chapter 3 should not be considered as static. Its form varies throughout the year, displaying its canonical signature only during winter, the season of focus in this thesis. In summer, the pattern is greatly reduced in area and amplitude, explaining less than 5% of domain variance. These results imply that the pattern is not operative during the warm season, or at least diminished in significance compared to other patterns of climate variability. During autumn and spring, the pattern takes on a more transitory appearance, gaining and losing similarity to the wintertime structure. The variance explained by the pattern and its rank relative to other patterns also modulate throughout the year. Fraction of variance explained exhibits two maxima during the year, one in early spring and another in late autumn. During autumn the Eurasian pattern described here is the dominant pattern of hemispheric variability. In spring it competes with the NAO for most variance explained.

Chapter 5

THE INFLUENCE OF THE EURASIAN PATTERN ON WINTERTIME CLIMATE

Now that the existence and structure of the Eurasian pattern have been established, we will explore its influence on surface climate and investigate whether the pattern has impacts on time scales shorter than a month. Whereas linear regression was the primary tool used in Chapter 4, in Chapter 5 we will employ the technique known as compositing. In this method the data are divided into categories, allowing comparison of their respective means and other statistics. Compositing has been used in previous studies to identify the impacts of phenomena such as El Niño/Southern Oscillation (Ropelewski and Halpert, 1987), the Quasi-Biennial Oscillation (Holton and Tan, 1980), and the Arctic Oscillation (Thompson and Wallace, 2001). In each case, the authors partitioned data into groups according to an index related to the feature of interest. For example, by isolating El Niño years and La Niña years (i.e., high ENSO index vs. low ENSO index), Ropelewski and Halpert (1987) could identify the influence of ENSO on mean precipitation globally.

Our basis for compositing will be the standardized expansion coefficient time series of EOT3. First we divide the 200 months of the time series into four quartiles ranked by the value of the index. Next we select the top and bottom quartiles and label them EOT3+ and EOT3-, respectively. Once the categories have been defined, we can calculate means and other statistics such as variance to form a series of composites. This chapter presents composites for several surface and upper air fields, illustrating the influence of EOT3 on Eurasian wintertime climate.

Results presented in Chapter 4 suggested that the Eurasian pattern has a particularly strong influence on SAT over the supercontinent; specific attention will be given to confirming that result in monthly-mean reanalysis data and daily station data. Continuing the latter, more synoptic perspective, the influence of EOT3 on variability across time scales

will also be investigated. Daily-mean geopotential height data filtered into high-pass and low-pass components will be analyzed to illustrate the reduction in high frequency variance over northern Eurasia during the positive phase of EOT3, consistent with previous results from the literature (Dole, 1986).

5.1 Composites

Figure 5.1 shows composite mean anomalies and mean SLP for EOT3+ and EOT3-. The positive polarity of EOT3 is characterized by anomalously high pressure over northern Eurasia (upper left panel, Fig. 5.1), and a corresponding extension of the Siberian High to the north and west (lower left panel, Fig. 5.1). The Icelandic Low is largely confined to North Atlantic Ocean. The negative polarity of EOT3 is marked by negative SLP anomalies over much of the northern part of the continent. The full composite mean (lower right panel, Fig. 5.1) illustrates this extension of the Icelandic Low into the Barents Sea. Under EOT3-, the Siberian High is diminished in size and its central pressure is reduced slightly.

The anomalies under the opposing polarities of EOT3 lie along the pressure gradient between the climatological Icelandic Low and Siberian High. The movement of this gradient likely contributes to the pronounced SLP variance observed there in winter (center panel, Fig. 1.1).

At 500 hPa the influence of the Eurasian pattern is related to the strength of the zonal flow. In the positive polarity of EOT3, positive geopotential height anomalies fill the climatological mean trough observed over northwestern Russia (upper left panel, Fig. 5.2). In the composite mean, this is evidenced by the spreading of height contours and the appearance of a ridge centered just south of Novaya Zemlya. Negative height anomalies over Mongolia slightly alter the direction of flow entering the climatological mean trough over Japan. Under EOT3-, negative height anomalies over the Russian Arctic deepen the climatological trough there to the point of having the lowest 500 hPa heights in the NH polar vortex.

The composites in Fig. 5.2 show a weakening and strengthening of the upper level flow under EOT3+ and EOT3-, respectively. This is indicated by the spreading of geopotential height contours over western Eurasia in the EOT3+ composite and a deepening of the climatological mean trough over the Russian Arctic in the EOT3- composite.

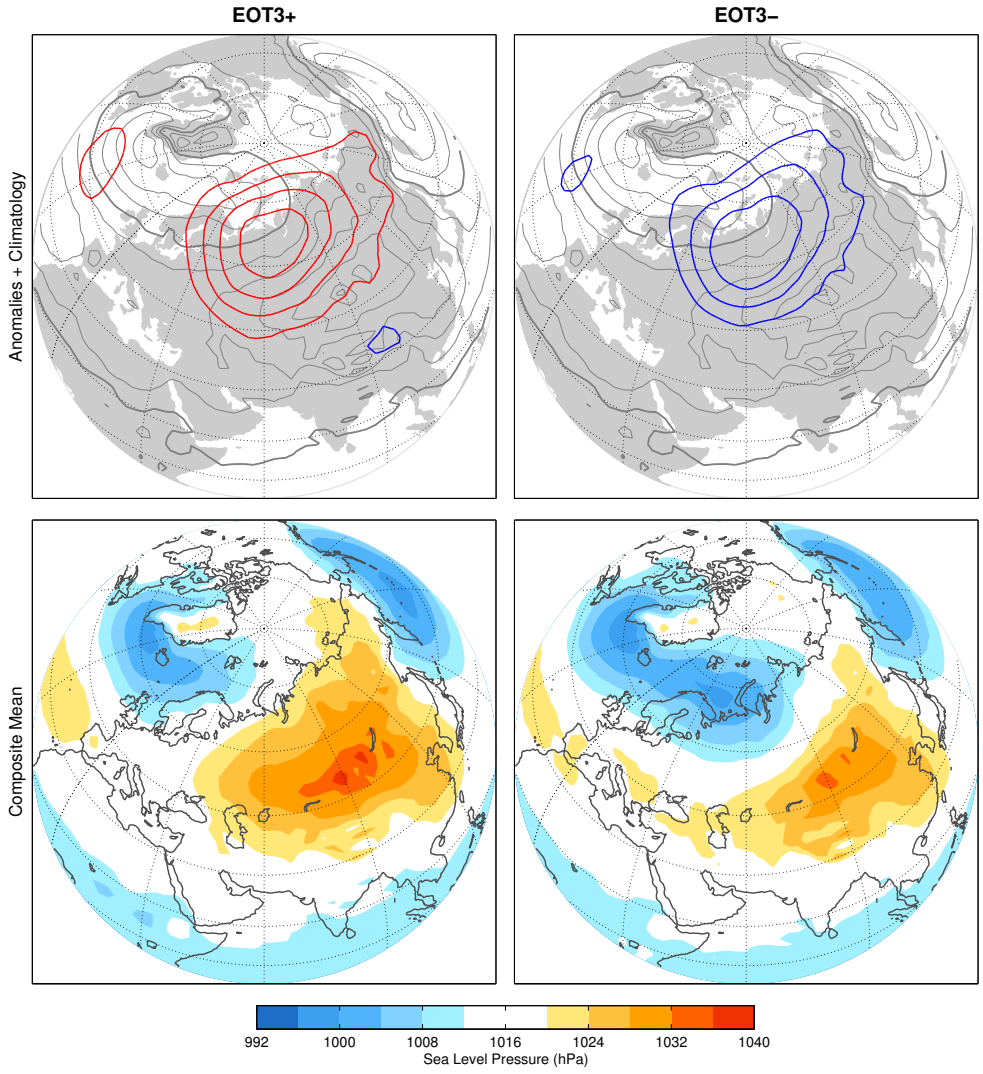

Fig. 5.1: Composite mean of 50 DJFM SLP anomalies under (upper left panel) EOT3+ and (upper right panel) EOT3-; Contour interval 2 hPa. Climatological DJFM SLP shown in black contours; Contour interval 4 hPa, bold reference contour 1012 hPa. Composite mean of DJFM SLP under (lower left panel) EOT3+ and (lower right panel) EOT3-.

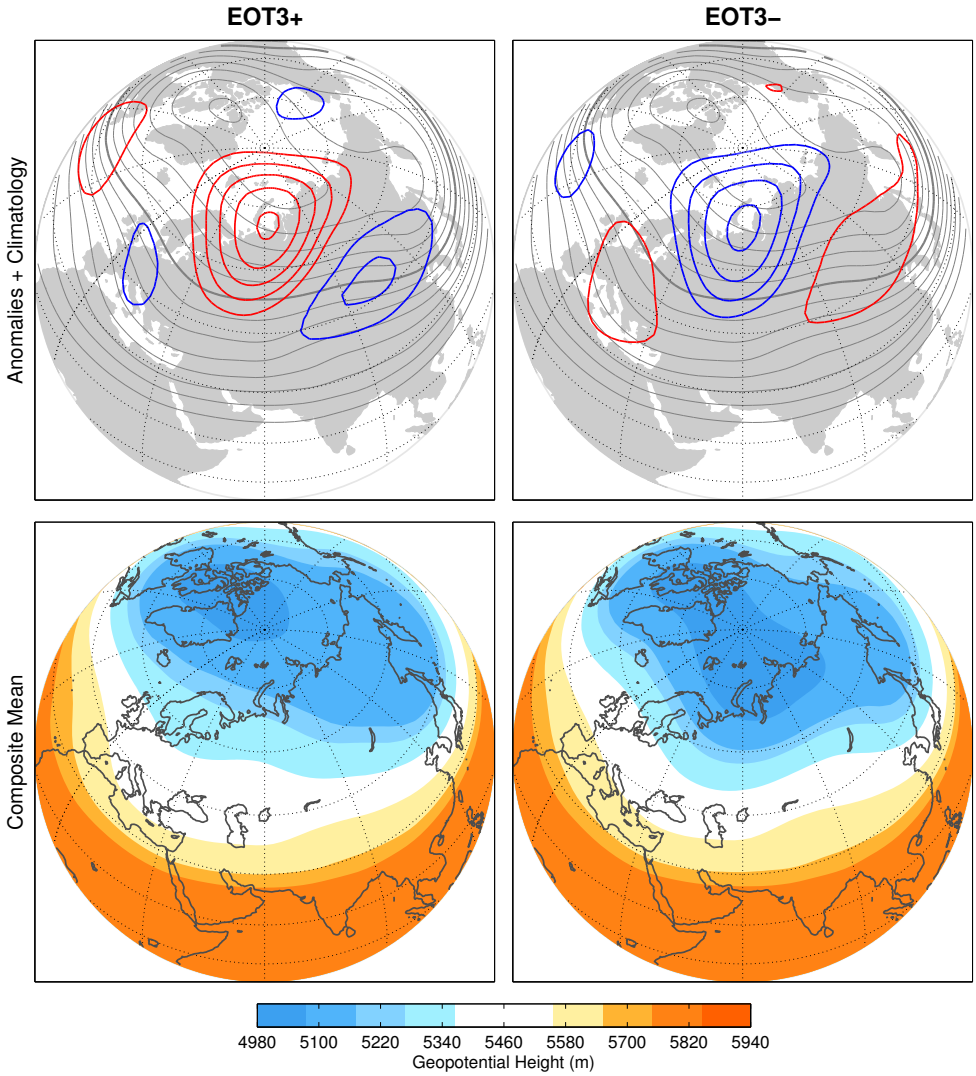

Fig. 5.2: Composite mean of 50 DJFM 500 hPa geopotential height anomalies under (upper left panel) EOT3+ and (upper right panel) EOT3-; Contour interval 10 m. Composite mean of DJFM 500 hPa geopotential height under (lower left panel) EOT3+ and (lower right panel) EOT3-.

In Chapter 4, regression maps illustrated the SAT pattern associated with EOT3. Composites of SAT are shown in Fig. 5.3. In the positive polarity of the Eurasian pattern, the continent is anomalously cold from the Baltic Sea to the Pacific coastline. As was shown earlier, the core of the negative temperature anomalies lie just north of the Altai and Sayan mountain ranges of eastern Eurasia. The full SAT composite (lower left panel, Fig. 5.3)

shows cold air temperatures over northeastern Siberia pulled southwestward toward central Siberia. Temperatures to the east of high elevations (black contour, Fig. 5.3) are also below normal. The EOT3- composites exhibit a warm continent. The full composite (lower right panel, Fig. 5.3) shows more moderate temperatures across western and central Siberia. The coldest temperatures over the continent, in the far northeast, are largely unaffected by the Eurasian pattern. The differences in the composite mean patterns between the opposing polarities of EOT3 are generally small, indicating the strength of the climatological mean temperature gradient across Eurasia.

Figure 5.4 shows the change in precipitation relative to normal between the opposing polarities of EOT3 of SLP. Figure 5.5 shows climatological wintertime monthly-mean precipitation for reference. During EOT3+ months, precipitation is suppressed over northwestern Russia in the center of the positive anomalies in EOT3 of SLP. The decrease amounts to 30% of climatological normal monthly-mean precipitation over northwestern Russia (left panel). Under EOT3- conditions, precipitation over northern Eurasia is enhanced by up to 30% at some locations around northwestern Russia (right panel, Fig. 5.4). This reflects the deepened climatological trough and the associated increase in flow from the North Atlantic.

The composites shown here depict the positive phase of EOT3 as an expansion of the Siberian High with reduced upper level zonal winds, a cold continent, and reduced precipitation. In the negative phase, conditions are characterized by an extended Icelandic Low, increased zonal flow aloft, positive SAT anomalies across the continent and increased precipitation over northwestern Russia.

Composites were also formed for snow cover extent (not shown). No large differences were found. Changes in observed snow cover frequency between EOT3+ and EOT3- were of the order 20% and were confined to southern Eurasia. Previous studies have shown that snow cover is pervasive over the continent in wintertime (Bamzai, 2003), with 100% coverage extending from northwestern Russia to the Pacific coastline. The changes in precipitation observed in the composites shown in Fig. 5.4 suggest that the influence of EOT3 may be stronger with respect to snow depth. Unfortunately, a satisfactory observational data set for Eurasia was not available for use in this thesis. However, Popova (2007) performed rotated EOF analysis on 66 years of February mean snow depth data over northern Eurasia.

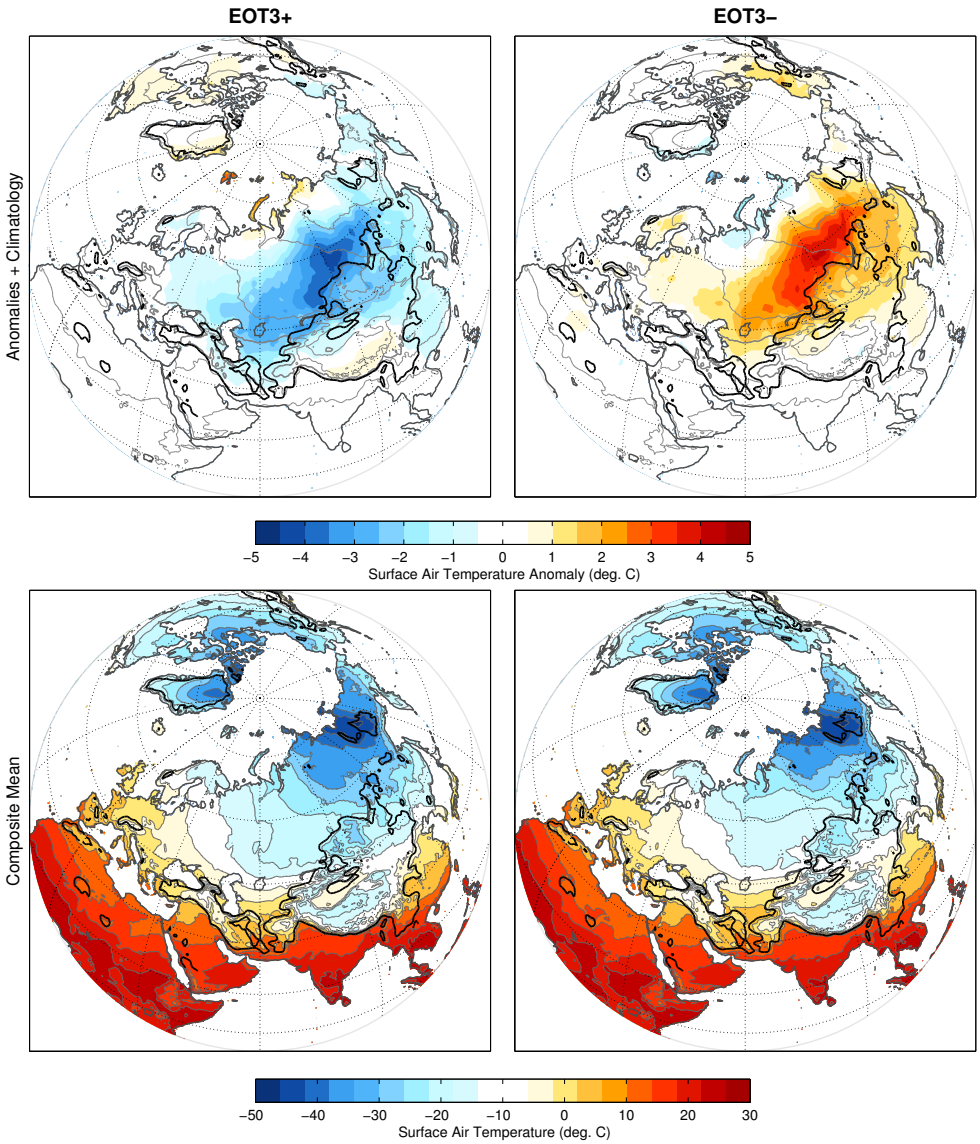

Fig. 5.3: Composite mean of 50 DJFM SAT anomalies under (upper left panel) EOT3+ and (upper right panel) EOT3-; Climatological SAT shown in black contours, interval 10°C, bold reference contour 0°C. Composite mean of DJFM SAT under (lower left panel) EOT3+ and (lower right panel) EOT3-; Contour interval 5°C, bold reference contour 0°C. 1500 m topographic isoline shown in black.

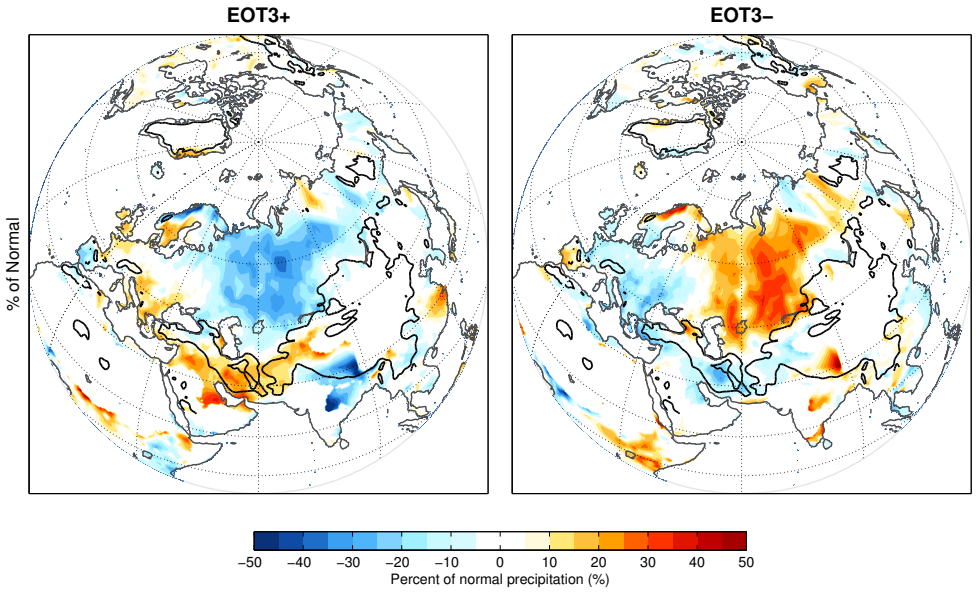

Fig. 5.4: Composite mean percent change from normal of 50 DJFM precipitation anomalies under (left panel) EOT3+ and (right panel) EOT3-; plotting of percent change from normal suppressed at locations receiving less than 1 mm/mon.

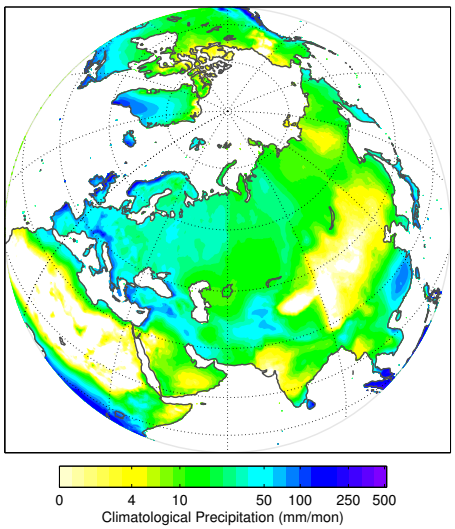

Fig. 5.5: Climatological wintertime (DJFM) monthly-mean precipitation.

Table 5.1: Temporal correlation coefficients calculated for wintertime-mean EOT1-3 and two indices of wintertime-mean Eurasian snow cover extent (DJFM and NDJFM).

	DJFM	**NDJFM**
EOT1	0.42	0.39
EOT2	0.01	0.00
EOT3	0.23	0.25

The leading rotated EOF from her analysis describes a broad positive snow depth anomaly across northwestern Russia and central Siberia, consistent with the precipitation anomalies observed in the EOT3 composites. The leading PC from her analysis exhibits a positive trend throughout the late 20th century, suggesting an inverse relationship with the time series associated with EOT3. The author's data were not available for testing with the time series associated with EOT3.

Indices of wintertime Eurasian snow extent were compiled using data from the Rutgers University Global Snow Laboratory, and correlated with the indices of the leading three wintertime EOTs of SLP. Results are shown in Table 5.1. They suggest that the largest influence on wintertime Eurasian snow cover extent comes from EOT1. EOT3 is also correlated with wintertime mean snow cover extent, but to a lesser degree.

5.2 Cold-Air Outbreaks

The SAT composites shown in the previous section demonstrate the strong influence of EOT3 on temperature in monthly-mean data. Compositing analysis was also performed on daily-mean temperature from station data across Eurasia to investigate the influence of EOT3 on shorter time scales of variability. For each station, a threshold temperature was selected to highlight the coldest 10% of temperatures the daily-mean temperatures. Days with a daily-mean temperature lower than the threshold were flagged as cold days. The number of cold days in the opposing polarities of EOT3 were counted and analyzed.

Results for 22 Eurasian stations are shown in Table 5.2. For each station, the ratio of cold days occurring in contrasting polarities of EOT3 is shown in graphical form in Fig. 5.6. The pattern displayed by the points is consistent with the composites shown in Fig. 5.3. Anomalously cold conditions are more common across the continent in EOT3+ and more common in the Russian Arctic in EOT3-. Some of the most robust results are observed in the center of the cold anomalies shown in the aforementioned composites; for example, cold conditions were observed more than 5 times more often during EOT3+ in Irkutsk, Russia, and Novosibirsk, Russia. The opposite is the case around Svalbard, where cold days were observed about 4 times more often during EOT3-. While the counts for stations in central Europe and Japan are less statistically significant, they do display a pattern consistent with results determined using monthly-mean data.

The results for Seoul, South Korea, Beijing, Guiyang, and Guangzhou, China indicate more cold days during EOT3+. These results are suggestive of the cold-air outbreaks over East Asia described by Lau and Lau (1984). Takaya and Nakamura (2005a) demonstrated a strong relationship between the intensity of the Siberian High and associated cold surges to midlatitude East Asia. Thus, it is expected that the stronger Siberian High associated with EOT3+ would influence the buildup of colder air over the continent and more cold-air outbreaks toward East Asia.

A similar composite analysis was performed using Asian 49 years of dust storm data from Zijiang and Guocai (2003). 86% of severe dust storms in the northern China record occurred during spring (MAM). Thus, the first three EOTs from the MAM EOT analysis shown in Chapter 4 were used as a basis for compositing dust storm events. No robust results were obtained in this analysis.

5.3 Geopotential height variance

The influence of the Eurasian pattern on monthly timescales has been established through the compositing of monthly-mean anomalies for SLP, 500 hPa geopotential height, SAT, and precipitation. Those results indicate large scale changes in the circulation pattern and associated changes in surface climate. Here we investigate whether the Eurasian pattern systematically influences variability on timescales shorter than a month.

Table 5.2: Number of days with daily average temperature below threshold value (°C) at Eurasian stations 1958-2008. # Days, the total number of days in the station's record; Threshold, the temperature below which the day is counted as an event; Total Events, the total number of events; EOT3+ and EOT3-, the number of days that fall in a month within the indicated polarity. Threshold chosen to isolate approximately the coldest 10% of total days.

Station	**# Days**	**Threshold**	**Total Events**	**EOT3+**	**EOT3-**
Irkutsk, RUS	4300	-25	405	176	32
Novosibirsk, RUS	4367	-24	436	197	24
Lensk, RUS	3869	-38	354	65	16
Beijing, PRC	3818	-5	477	150	78
Seoul, ROK	4357	-7	396	117	45
Sapporo, JPN	4511	-7	481	121	85
Nagano, JPN	3059	-3	377	136	69
Guiyang, PRC	3810	1	389	166	70
Guangzhou, PRC	3818	9	428	145	95
Kathmandu, NPL	2042	9	307	39	123
Kabul, AFG	1804	-5	171	70	32
Tashkent, UZB	4195	-4	390	158	84
T'bilisi, GRG	464	-1	56	32	6
Moscow, RUS	4412	-15	435	112	71
Smolensk, RUS	4399	-15	442	128	53
Riga, LAT	4427	-10	444	117	61
Warsaw, POL	3728	-7	403	64	94
Oslo, NOR	3460	-13	328	54	79
Ny Ålesund, SVB	1038	-20	105	10	47
Hopen, SVB	3272	-24	321	27	114
Mys Zhelania, RUS	3236	-30	391	44	117
M. Karmakuly, RUS	4258	-24	508	82	160

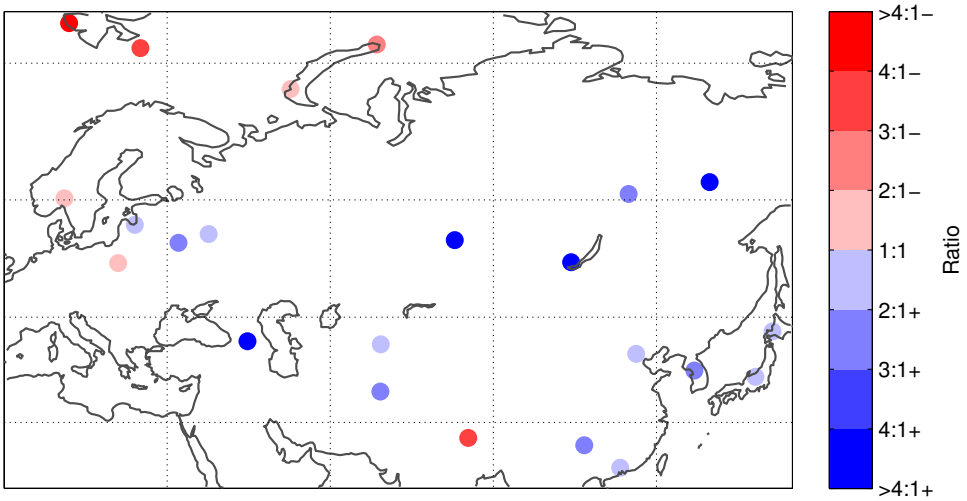

Fig. 5.6: Ratio of cold daily mean temperature events observed in opposing polarities of EOT3 of monthly-mean SLP. Dots correspond to locations listed in Table 5.2.

Daily-mean 300 hPa geopotential height data constructed from 6-hourly output of the NCEP-NCAR Reanalyses were filtered in accordance with the method discussed in Chapter 2, producing 6-day high pass (HP) and low pass (LP) filtered data. The former will be used to represent variability associated with weather in this analysis, and the latter is used to represent fluctuations associated with variability of intermediate and long timescales.

Filtered 300 hPa geopotential height variance for days within the months of EOT3+ and EOT3- is shown in Fig. 5.7. HP variance patterns (upper panels) show a large scale reduction in variability over the Eurasian supercontinent during EOT3+, while the variance pattern over the Atlantic and Pacific remains unchanged. The composite difference field (upper right panel) illustrates the coherent decrease in HP variance extending from the North Atlantic to the Pacific coastline. Thus, when the Siberian High is strong and expansive the weather over Eurasia is relatively quiescent. When the Siberian High is weak and the Icelandic Low extends into the Barents Sea, synoptic disturbances are more common over the continent, and a well defined storm track appears across Eurasia from Scandinavia to northeastern China. The LP variance patterns (lower panels) exhibit more subtle changes that are not as focused over the Eurasian sector.

For the sake of comparison, the same analysis was performed using EOT1 as the basis for compositing.[1] Results are shown in Fig. 5.8. The HP variance maps (upper panels) show that the differences in variance associated with EOT3 is nearly the same as those for EOT1-. Maps depicting LP variance in EOT1+ and EOT1- (lower panels) indicate more dramatic changes between the opposing polarities that are largely restricted to the Atlantic sector.

EOT1 and EOT3 have a qualitatively similar influence on HP variance in that they reduce variability in their polarity characterized by positive SLP anomalies at higher latitudes and/or a weakening of the westerlies. The reductions are slightly larger in the case of EOT1, but the structure of the patterns is similar. The LP variance maps for EOT1 are substantially different. Consistent with results of (Rennert, 2007), variances are larger over Baffin Bay in association with EOT1-. However, EOT3 does not show a pronounced Eurasian signature.

5.4 Summary

The influence of the Eurasian pattern on weather and monthly-mean climate over Eurasia has been discussed using composites of various meteorological fields to illustrate changes associated with shifts in the standardized expansion coefficient time series for EOT3 of NH SLP. They portray a picture of Eurasian variability characterized by an amplification and northwestward expansion of the Siberian High in EOT3+ and weakening and contraction in EOT3-. In the SAT field, the changes in SLP produce cold (warm) anomalies over the continent in EOT3+ (EOT3-). The prevalence of cold anomalies in EOT3+ is observed both in monthly-mean data and daily-mean station data. However, the anomalies are not strong enough to produce a pronounced shift or distortion of the SAT isotherms.

Aloft, EOT3+ is associated with reduced zonal flow across Eurasia and EOT3- is marked by a deepening of the mean trough observed over northwestern Russia. The changes in the surface and the upper level circulation influence the direction of the steering flow over Eurasia, impacting the tracks of synoptic disturbances over the region, causing changes in

[1]We define the positive phase of EOT1 the one in which the Icelandic Low is accentuated. This follows the definition of the opposing polarities of the NAO and NAM.

precipitation and HP variance over the continent. During EOT3+, precipitation and HP variance are diminished over the continent. Under EOT3- conditions, a coherent storm track in HP variance extends across Eurasia, enhancing precipitation.

The changes in meteorological fields described here represent substantial wintertime impacts across Eurasia. Although the continent is generally cold and dry, deviations about the mean state are widespread and, in some cases, large in magnitude. Extreme cold was shown to be associated with EOT3+ at locations throughout much of Eurasia. Furthermore, differences in precipitation observed between the opposing polarities of EOT3 amount to almost a factor of 2 in the core of the Eurasian pattern in SLP.

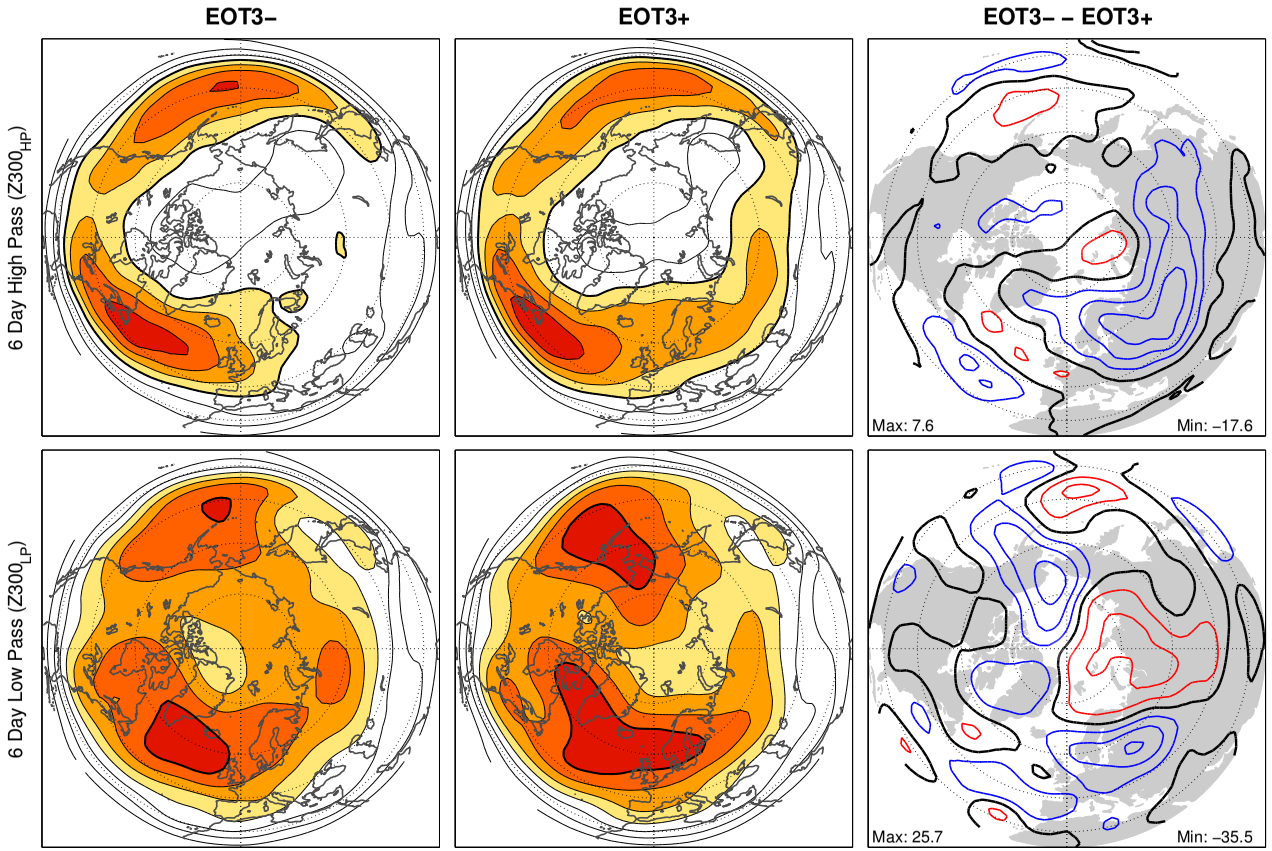

Fig. 5.7: Composite mean variance calculating using filtered daily-mean 300 hPa geopotential height data within 50 months for (left panels) EOT3+ and (middle panels) EOT3- of monthly-mean SLP; Contour interval (upper panels, 6 day high pass filtered heights) 10 hPa^2 and (lower panels, 6 day low pass filtered heights) 25 hPa^2, bold reference contour (upper panels) 40 hPa^2 and (lower panels) 200 hPa^2. Composite difference shown in right panels; Contour interval (upper right panel) 2 hPa^2 and (lower right panel) 10 hPa^2.

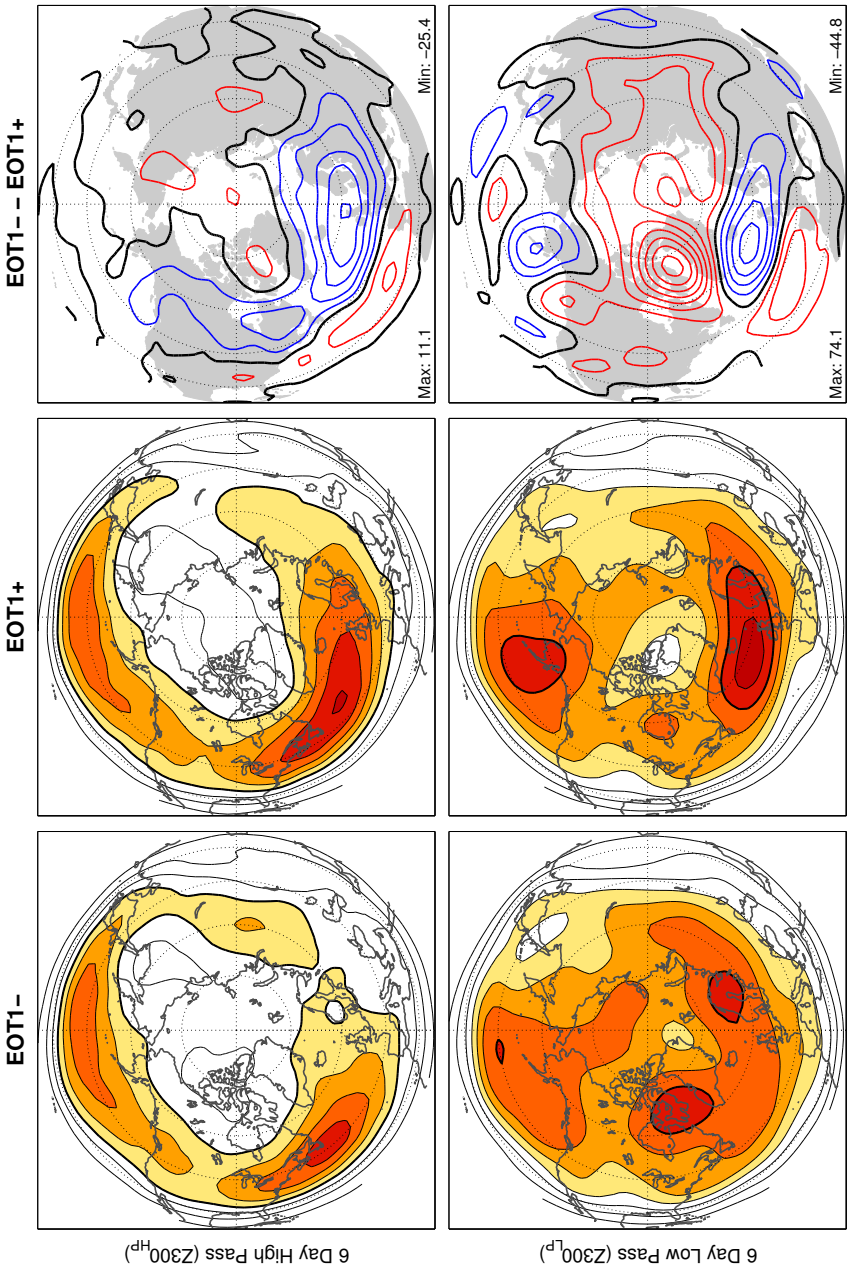

Fig. 5.8: Display same as Fig. 5.7, except for EOT1 of monthly-mean SLP.

Chapter 6

THE EURASIAN PATTERN IN PENTAD-MEAN DATA

Thus far, the Eurasian pattern has been documented solely on the basis of monthly-mean data. Much of the atmosphere's low frequency variability occurs on time scales longer than a few weeks, and monthly-mean data adequately capture the essence of those variations. Quadrelli and Wallace (2004) showed that the two leading patterns of NH SLP variability account for a third of hemispheric variance on monthly timescales, and up to three-quarters of variability when the data are averaged to 5-year means. However, averaging data over periods of a month or longer limits our ability to investigate the time evolution of patterns on shorter timescales. Pentad-mean data contains information about the circulation that is removed when averaging temporally to the monthly timescale. Here we repeat the EOT analysis described in Chapter 2 using wintertime pentad-mean data derived from consecutive, non-overlapping five day averages of the daily-mean SLP field. Results are described and utilized to investigate the time evolution of the leading two EOTs, which correspond to the NAO and the Eurasian pattern. Projection indices are formed to investigate whether the Eurasian pattern exhibits significant skewness.

6.1 Results of EOT analysis applied to pentad-mean SLP data

Figure 6.1 shows regression patterns associated with the first three EOTs of wintertime pentad-mean SLP data. EOT1 (left panel) resembles the NAO and explains 10% of the domain variance. Compared to the pattern associated with EOT1 of monthly-mean SLP, EOT1 of pentad-mean SLP is more limited in longitudinal extent with large amplitudes confined to the North Atlantic sector. Whereas the northern center of action in EOT1 of monthly-mean SLP extends eastward over the Arctic coastline of Eurasia, the northern center in EOT1 of pentad-mean SLP does not.

EOT2 (center panel, Fig. 6.1) is generally similar to the Eurasian pattern defined by

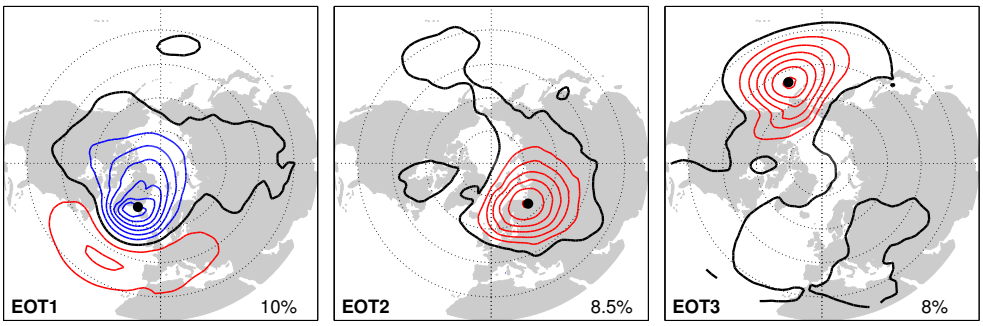

Fig. 6.1: First three spatial patterns (EOT) associated with the Empirical Orthogonal Teleconnection analysis of wintertime (DJFM) pentad-mean SLP anomalies from NCEP-NCAR reanalyses 1958-2008. Contour interval is 2 hPa.

EOT3 of wintertime monthly-mean SLP and explains 8.5% of the domain variance. The primary center of EOT2 is shifted slightly westward relative to EOT3 of monthly-mean SLP. It resembles the loading pattern of the Eurasian pattern during fall and spring, when the pattern does not extend to the Pacific coastline (Fig. 4.8). EOT5 (not shown) is centered over eastern Eurasia, and its existence may explain why EOT2 of pentad-mean SLP does not extend farther to the east. EOT3 (right panel, Fig. 6.1) is closely related to the PNA pattern observed in the 500 hPa geopotential field (Wallace and Gutzler, 1981) and explains 8% of the domain variance. Cumulatively, the leading three patterns explain $\sim 12\%$ less variance than their monthly-mean counterparts. This is consistent with the results of Quadrelli and Wallace (2004), who showed that the prominence of the leading patterns of NH SLP variability is directly proportional to the relative length of the data averaging period. Having determined the pentad-mean patterns that correspond to variability over the North Atlantic and northern Eurasia, we now employ their standardized expansion coefficient time series to investigate their temporal evolution.

6.2 Evolution of the Eurasian pattern

Throughout this thesis, the Eurasian pattern has been described in terms of its mature phase structure and impacts. To investigate the development and decay of the pattern, we create composites defined by the 100 largest positive and negative expansion coefficients in

the time series associated with the pentad-mean EOT2. In order to ensure that the events are unique, we require that the center pentads be at least 2 pentads apart from the 99 other pentads in the composite. Composite means were calculated for lags of -5, -4, -3, -2, -1, 0, 1, 2, 3, 4, and 5 pentads. The full evolution of the Eurasian pattern was found to occur within a few pentads, so only lags of -1, 0, and +1 are shown.

Fig. 6.2 shows composite means for SLP anomalies, 500 hPa geopotential height anomalies, and the full field corresponding to each variable for the positive phase of EOT2. At lag -1 pentad (-5 days), positive SLP anomalies are observed over northwest Russia. By lag 0 the SLP anomalies have increased from a peak of 10 hPa to 21 hPa above normal. 5 days later at lag +1 pentad, the anomalies decreased to a peak of 8 hPa and have spread slightly westward. In the full SLP field, this evolution is characterized in terms of an expansion and strengthening of the Siberian High over western Eurasia. As the high recedes towards its climatological position at lag +1 pentad, the Icelandic Low remains weakened. The 500 hPa height anomalies follow a similar progression, but also exhibit downstream development; a new center appears north of the Tibetan plateau at lag 0 and remains at lag +1 pentad. Anomalies at the surface and 500 hPa shift appear to shift slightly westward throughout their evolution.

At lag 0, a strong ridge replaces the trough present over Scandinavia at lag -1 pentad. A folding of the 5460 contour is evident over northwestern Russia in the full 500 hPa height composite at lag 0. This signature has been associated with cyclonic wave-breaking of Rossby waves and associated with blocking of the zonal flow (Pelly and Hoskins, 2003). This suggestions an association between the Eurasian pattern and upper-level blocking over northwest Russia. The lag +1 pentad 500 hPa height map shows a return toward a climatology with a trough over northern Europe.

Fig. 6.3 shows the composite means for events in the negative phase of EOT2. The symmetric evolution of SLP anomalies (far left panels) is similar to those of EOT2+, but the magnitude of the anomalies are slightly smaller and area associated with a gentler anomalous height gradient. The full field composite of EOT2- shows the extension of the Icelandic Low to the east beginning at lag -1 pentad, maturing to a deep low center at lag 0, and a reduction in area and increase in central pressure by lag +1 pentad. At 500 hPa,

the anomalies develop and decay in the form of a wave-like pattern emanating from the North Atlantic exhibiting downstream development. At lag -1 pentad, the opposite signed anomalies over Svalbard and western Europe are of similar magnitude. By lag 0, a new center has developed over southern Siberia. At lag +1 pentad, the western Europe anomaly has weakened and the anomaly over southern Siberia has maintained its amplitude and increased in areal extent. The full 500 hPa geopotential field composites (far right panels) illustrate a deepening of the climatological trough over Europe and western Eurasia. At lag +1 pentad, the intensity of the trough is weakened toward the climatology.

The evolution of the opposing polarities of EOT2 is consistent with our interpretation of the Eurasian pattern. In its negative phase, the Icelandic Low extends an deepens in situ over the Barents Sea while the climatological trough aloft intensifies, bringing stronger zonal flow inland from the west. In its positive phase, the Siberian High expands westward toward eastern Europe, and a large amplitude ridge forms aloft, blocking the zonal flow entering Scandinavia. The wave-breaking signature seen in the composite 500 hPa height field is an interesting result, offering further evidence that fluctuations of the Siberian High are linked to blocking over northwest Russia.

Previously, Dole and Gordon (1983) found three preferred regions of in which anomalies tend to persist beyond the timescale associated with synoptic variability: the North Atlantic (ATL), the North Pacific (PAC), and Northern Soviet Union (NSU). Later, Dole (1986) determined that positive anomalies in each region are frequently associated with blocking ridges and negative anomalies with intensified westerly flow. The positive and negative composite mean patterns and EOFs shown by Dole for the NSU region strongly resemble EOT2 shown in Fig. 6.1. Chen and van den Dool (2003) found an asymmetry in the teleconnection pattern associated with the center of climatological-mean 500 hPa geopotential height variance over northwestern Russia. Whereas negative anomalies in the primary center of action appeared to be associated with a wave-train stretching from the North Atlantic across Eurasia, large positive anomalies over northwestern Russia were aligned with negative secondary centers to the south, structurally analogous to an "omega block." Takaya and Nakamura (2005b) investigated the geographical dependence of blocking with the intensification of the Siberian High. They showed composites of the 20 strongest events of

positive upper-level geopotential height anomalies at grid points across Eurasia and found that blocking originating over western Russia was strongly associated with intraseasonal amplification of the Siberian High.

Using an approach similar to the investigation presented at the end of Chapter 5, here we compare the evolution of pentad-mean EOT2 with that of EOT1. Figures 6.4 and 6.5 show the composite evolution of EOT1 in its negative and positive phase, respectively. The negative phase is characterized by blocking over Greenland (Fig. 6.4). The familiar wave-breaking signature described previously is apparent in the 500 hPa geopotential height field over Baffin Bay (middle panel, far right). Woollings et al. (2008) offered an interpretation of the NAO that hypothesizes that this phenomenon is a reflection of variations in the frequency of occurrence of upper-level Rossby wave-breaking events over the North Atlantic. At the surface, the negative phase of EOT1 depicts a surface high replacing the climatological Icelandic Low, displacing the mean feature to the south, east of Labrador (middle panel, far left).

The positive phase of EOT1 is characterized by an intensification of the Icelandic Low and strengthening of the subpolar jet over the North Atlantic (Fig. 6.5). The evolution of EOT1 and EOT2 have several characteristics in common. The evolution of the 500 hPa anomalies exhibits downstream development. In EOT1- and EOT2+, slight retrogression of the strong positive anomaly at 500 hPa is observed from lag 0 to lag +1 pentad. Although the anomalies associated with the two patterns exhibit a similar evolution, the mean state they develop over is different. EOT1 involves a strengthening and weakening of the center of the climatological Icelandic Low. EOT2 is related to shifts in the geopotential height gradient between the Icelandic Low and Siberian High.

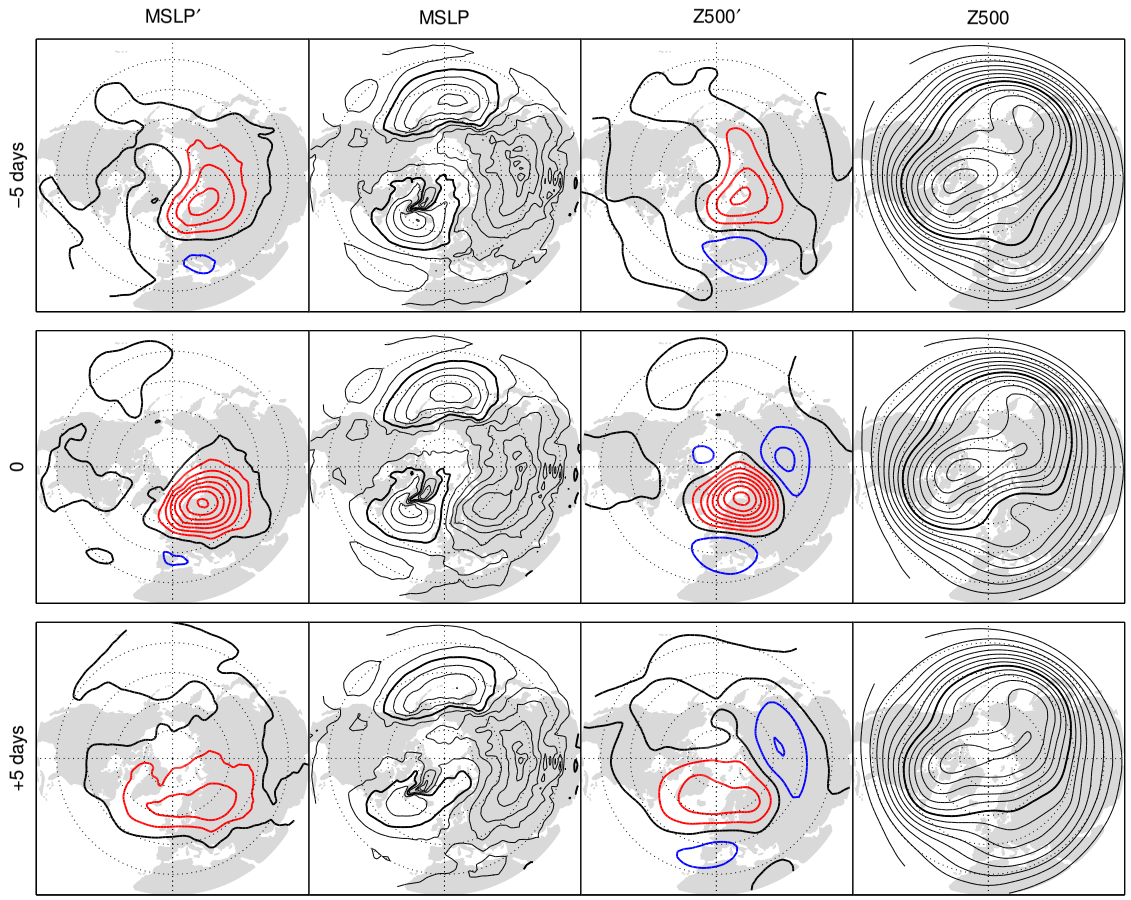

Fig. 6.2: Composite mean evolution of 50 pentad-mean SLP and 500 hPa geopotential height anomalies for EOT2+ of pentad-mean SLP. Lags of -1, 0, +1 pentads (5 days) are shown. The display includes anomalies of (first column) SLP and (third column) 500 hPa geopotential height and the full (second column) SLP and (fourth column) height fields. Contour interval is (first column) 3 hPa, (second column) 4 hPa, (third column) 30 m, (fourth column) 60 m. Bold reference contours are (second column) 1012 hPa and (fourth column) 5400 m.

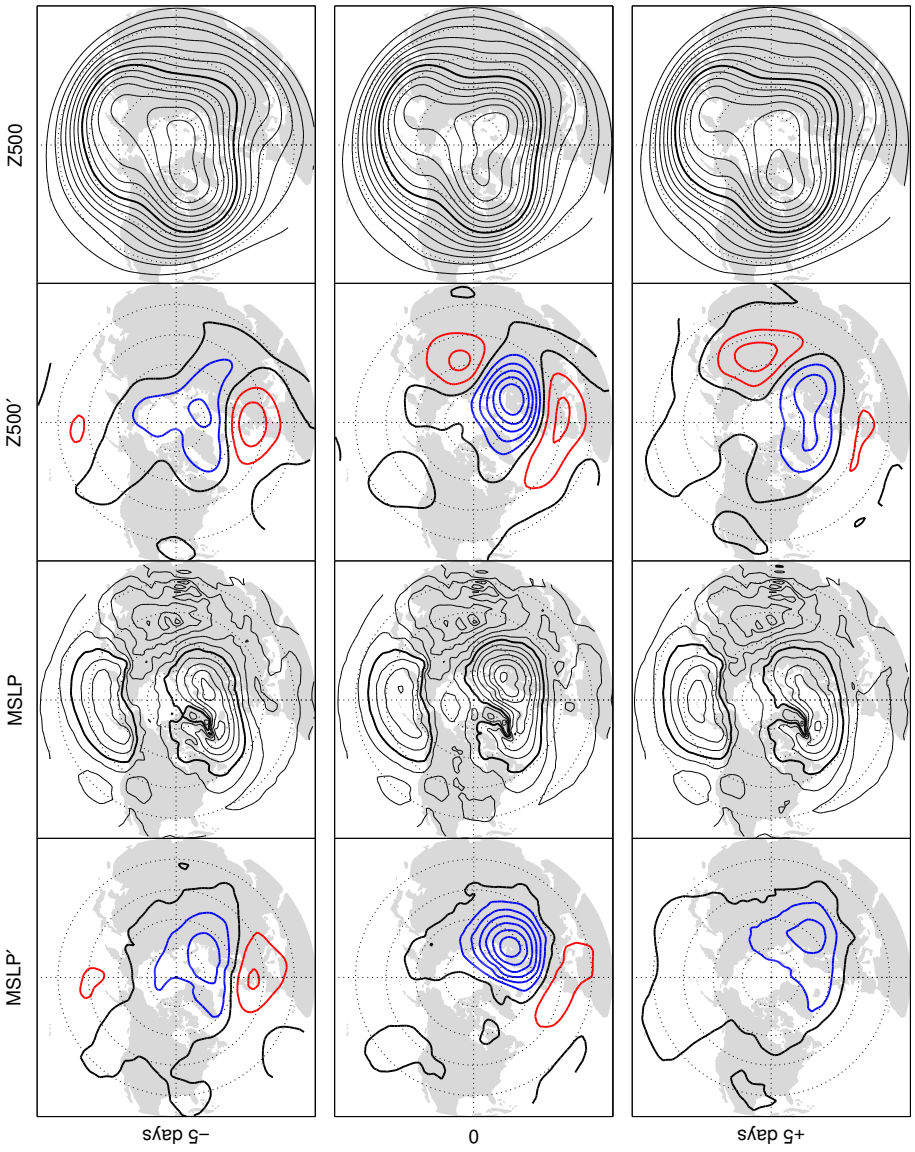

Fig. 6.3: Display same as Fig. 6.2, except for EOT2- of pentad-mean SLP.

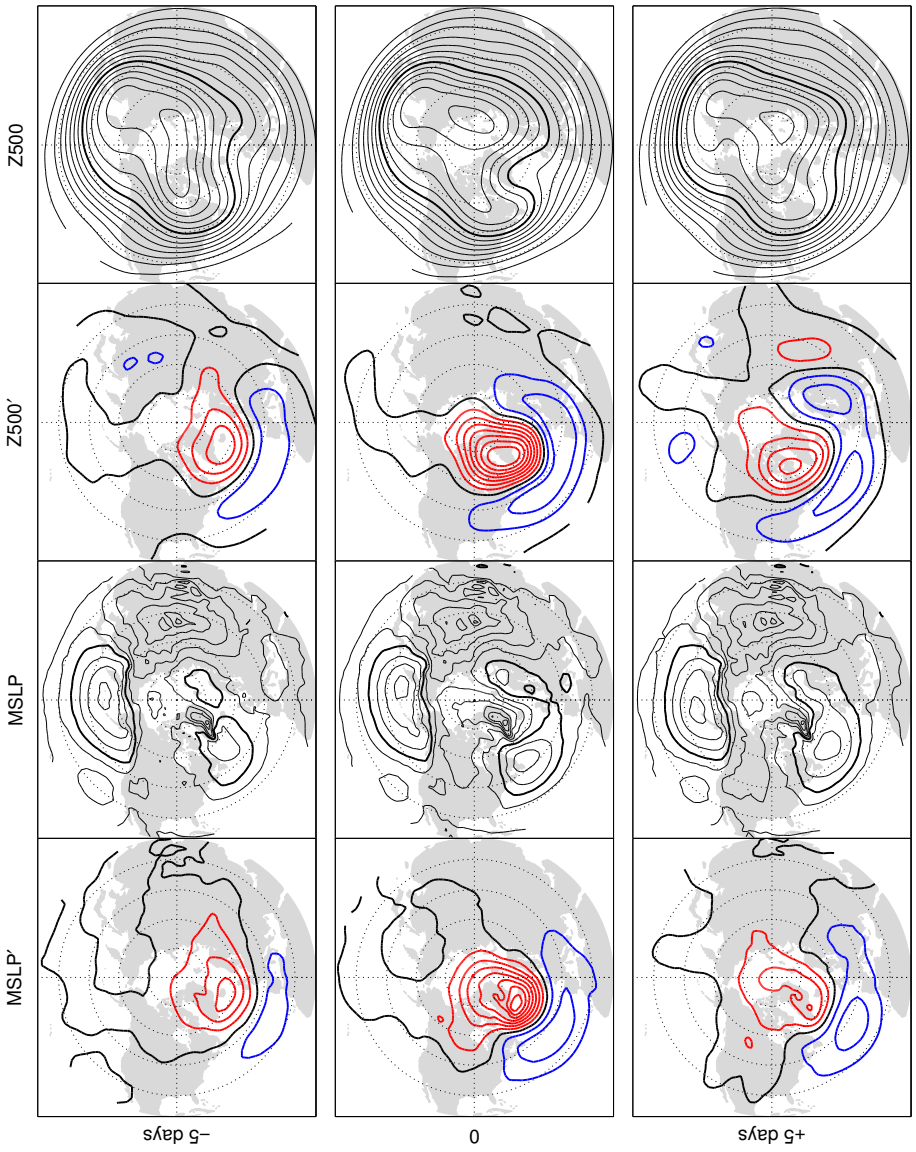

Fig. 6.4: Display same as Fig. 6.2, except for EOT1- of pentad-mean SLP.

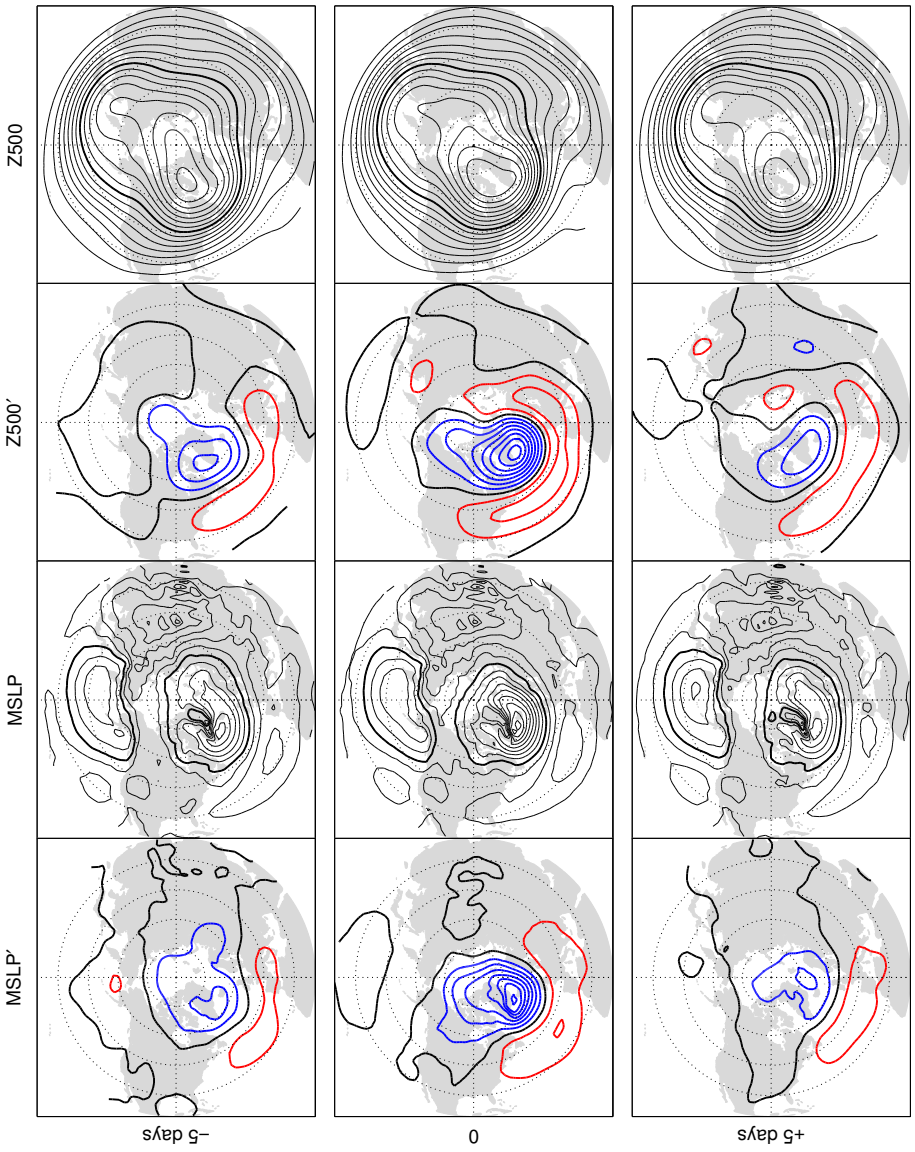

Fig. 6.5: Display same as Fig. 6.2, except for EOT1+ of pentad-mean SLP.

6.3 Skewness of the index of the Eurasian pattern

Woollings et al. (2009) have found evidence of skewness in the NAO, presenting a careful description of negative skew in NAO indices on time scales ranging from daily-mean to monthly-mean, in indices defined at the surface and 500 hPa, and in a wind-based index. γ, the moment coefficient of skewness, is defined as:

$$\gamma = \frac{\mu_3}{\sigma^3} \tag{6.1}$$

where μ_3 is the third moment about the mean, μ

$$\mu = \frac{1}{N}\sum_{i=1}^{N} x_i \tag{6.2}$$

$$\mu_3 = \frac{1}{N}\sum_{i=1}^{N} (x_i - \mu)^3 \tag{6.3}$$

and σ is the standard deviation.

$$\sigma = \sqrt{\frac{1}{N}\sum_{i=1}^{N} (x_i - \mu)^2} \tag{6.4}$$

Using EOF1 of 500 hPa to define a daily projection index for the NAO, Woollings and his coauthors found a γ value of -0.23. They verified this result by demonstrating similar coefficients of skewness calculated utilizing an index constructed from rotated EOF1 of 500 hPa, a 10-day low pass filtered variant of their daily index, a monthly-mean index extending back to 1821, and an index based on rotated EOF1 of 500 hPa zonal winds. Woollings et al. (2009) interpreted the skewness of the NAO as a suggestion of regime behavior, with two distinct states corresponding to blocked and zonal flow. Figures 6.2 and 6.3 suggest a similar upper level configuration of the flow field over northwestern Russia. While the regime behavior interpretation of Woollings et al. (2009) may not apply to the Eurasian pattern, confirming the skewness of the index of this pattern would provide another example of the behavior hypothesized by Woollings et al. (2008). It also would suggest the possibility of a continuum of blocking-related patterns over the North Atlantic sector.

Here we present a brief investigation of skewness in the NAO and the Eurasian pattern.

We define indices by projecting area-weighted SLP anomalies onto the regression pattern associated with EOT1 of monthly-mean NH SLP and EOT3 of monthly-mean NH SLP. Four projection indices are formed out of SLP anomalies representing various time averaging periods: 1) unfiltered daily-mean anomalies, 2) consecutive, non-overlapping five day means of daily SLP anomalies, 3) 10-day low pass filtered anomalies (obtained via the application of a fourth-order Butterworth filter with a cutoff frequency near 1/10 days^{-1} to daily-mean anomalies), and 4) monthly-mean anomalies. Each index is normalized by its standard deviation and skewness is calculated in the usual manner (6.1).

Table 4.1 demonstrated a correspondence between specific pairs of SLP and 500 hPa height based EOTs. Hence, another test of robustness was made by repeating the same analysis representing the NAO and the Eurasian pattern with EOT1 and EOT3 of monthly-mean NH 500 hPa geopotential height. Projection indices related to the 500 hPa patterns were formed with area-weighted 500 geopotential height anomalies. Table 6.1 displays results for the SLP-based and 500 hPa-based analyses. It has been noted that monthly-mean data may not be optimal for identifying skewness in these patterns due to the smaller sample size and the fact that the patterns evolve on shorter timescales (Woollings et al., 2009). Thus, we will focus primarily on the daily, pentad, and 10-day low pass filtered data, which have more temporal degrees of freedom.

The NAO results are consistent with the findings of Woollings et al. (2009), which are derived from ECMWF ERA-40 reanalysis data, confirming the strong skewness of the NAO defined at 500 hPa. Similar to Woollings et al. (2009), we found that SLP-based indices produced coefficients of skewness half as large as their 500 hPa counterparts. Woollings and his colleagues calculated a skewness value of -0.39 using a pseudo-station data index formed from the difference of pentad-mean SLP anomalies at two grid points in the ERA-40 data. We performed the same analysis using pentad-mean data from similar grid points in the NCEP-NCAR reanalysis and obtained a skewness of -0.38. It is unclear why such a disparity exists between the EOF-based index and the pseudo-station index. It could be that using the EOF pattern to define a projection index requires a more rigorous conformity to the NAO pattern than a pseudo-station index.

Table 6.1: Skewness of the NAO and the Eurasian pattern calculated using indices derived from their respective projection onto daily-mean (X), pentad-mean (X_5), 10-day low pass filtered (X_{10}), and monthly-mean (X_{30}) SLP and 500 hPa geopotential height ($Z500$) anomalies from the NCEP-NCAR Reanalyses 1958-2008. The NAO is defined as EOT1 of monthly-mean NH SLP and EOT1 of monthly-mean NH 500 hPa geopotential height. The Eurasian pattern is defined as EOT3 of monthly-mean NH SLP and EOT3 of monthly-mean NH 500 hPa geopotential height.

	SLP	SLP_5	SLP_{10}	SLP_{30}	$Z500$	$Z500_5$	$Z500_{10}$	$Z500_{30}$
γ_{NAO}	-0.09	-0.13	-0.16	-0.01	-0.33	-0.35	-0.38	-0.13
γ_{EUR}	0.16	0.21	0.23	0.40	0.17	0.19	0.21	0.32

Having confirmed the results of Woollings et al. (2009), we present new results related to the Eurasian pattern (second column, Table 6.1). In general, positive skewness is evident in indices defined at the surface and 500 hPa. Skewness of the Eurasian pattern increases from 0.16 in the daily-mean index to 0.23 in the index formed from 10-day low pass filtered SLP anomalies, and by a similar amount in 500 hPa indices.

Similar behavior is observed with respect to the NAO. As the averaging period is lengthened, the influence of high frequency fluctuations is removed, resulting in an increase in the skewness of both patterns. The sign of the skewness of both patterns indicates a preference for stronger or more frequent anomalous anticyclones than anomalous cyclones near the primary center of each pattern. Differences between the skewness of the patterns are also evident in Table 6.1. The magnitude of skewness of the Eurasian pattern is consistent whether defined at the surface or 500 hPa. The SLP-based NAO shows reduced coefficient of skewness values relative to the 500 hPa-based NAO. Further, the monthly-mean indices of the Eurasian pattern indicate increased skewness compared to the timescales less than a month. The monthly-mean NAO indices show an opposite trend, with decreased skewness relative to the other indices.

All of the Eurasian pattern indices investigated demonstrate appreciable positive skewness. The results described are robust with respect to the level at which the pattern is defined, as well as changes in the timescale of the data. Further investigation related to possible regime behavior of the Eurasian pattern is beyond the scope of this thesis. However, the documentation of skewness in the pattern is interesting in and of itself.

6.4 Summary

Using pentad-mean data, the structure and time evolution of the Eurasian pattern has been explored. Our results extend the results of the composite analysis of monthly-mean SLP and 500 hPa data to timescales less than a month, giving more detail about the evolution of the pattern. In the positive phase of the Eurasian pattern, the Siberian High expands westward and is accompanied by the development of a pronounced upper-level ridge. The a blocking signature associated with cyclonic Rossby wave-breaking was demonstrated in the lag 0 composite mean 500 hPa map. This adds to a preexisting body of research that

associates the amplification of the Siberian High with blocking events over northwest Russia.

When the index of the Eurasian pattern is in its negative polarity, enhanced zonal flow is observed over northern Eurasia. This state is linked to an eastward extension of the Icelandic Low and deepening of the climatological trough observed over eastern Europe. The evolution of the NAO was shown to set the development of the Eurasian pattern in context. Similarities were noted in the development and decay of SLP and 500 hPa anomalies related to both patterns. Differences were described with respect to the mean state over which the patterns develop.

Motivated by the recent work of Woollings et al. (2009), the skewness of the NAO and the Eurasian pattern were investigated. Results confirmed the strong skewness of the NAO shown by Woollings and coauthors and demonstrated robust skewness in the Eurasian pattern. These results suggest that both patterns may be described in terms of the regime perspective first introduced by Woollings et al. (2008). Under this interpretation, the NAO is considered as a weighted average of two regimes, one characterized by blocked zonal flow and the other unblocked zonal flow. The same wave-breaking signature was shown in composites of the NAO and Eurasian pattern, but the signature over western Eurasia was noticeably weaker than the signature evident in composites over the North Atlantic. This suggests that wave-breaking events over Eurasia are less frequent or less vigorous. Woollings et al. (2009) presented evidence in favor of a regime interpretation of the NAO, but further investigation is required to determine whether and to what extent the Eurasian pattern may also be depicted in this manner.

Chapter 7

SUMMARY

In this thesis we have investigated the structure and impacts associated with the third leading pattern of wintertime NH SLP variability, which is the dominant pattern of variability over Eurasia. The pattern has been appeared in previous studies, but authors have been hesitant to attach any physical significance to it. Using a multifaceted analysis scheme and data from several different sources, we have shown this pattern to be a robust feature of the NH wintertime circulation. Motivated by a desire to better characterize the monthly-mean circulation during NH winter, as well as the need to synthesize the various previous descriptions of teleconnection patterns over Eurasia, our methodology employed four objective techniques in hopes of yielding a pattern resilient with respect to the analysis method employed or data record utilized. The use of each method for the purpose of identifying patterns of climate variability has been well established in the literature, affording us the opportunity to compare the results of the various methods in a novel application.

The first three analyses presented are variations on eigenanalysis, now a common tool in climatological research. EOF3 of hemispheric SLP was shown to exhibit a primary center of action stretching over a broad portion of northern Eurasia and secondary centers over the North Atlantic and Arctic. REOF3 is among the rotated EOFs derived from a varimax rotation of a subset of conventional EOFs, and is characterized as a regionalized realization of EOF3. The leading EOF of a sectoral EOF analysis over Eurasia was shown to have strong similarities with REOF3. The method of EOTs was the fourth employed in the core of our analysis. Analogous to stepwise multiple linear regression, it selects successive grid points in the SLP field whose time series explain the largest fraction of the temporal variance at all points. EOT3 of SLP was found to display spatial characteristics similar to the EOF-based patterns, especially with respect to the primary center of action over northwestern Russia. EOT3 can be characterized as a compromise between the hemispheric pattern of EOF3 and

the highly regionalized REOF3.

All four patterns demonstrated over Eurasia were shown to be similar and to have highly correlated time series. Results were cross validated by repeating EOT analysis on even and odd years within the original data set. They were also reproduced in two independent data sets. EOT3 was selected to represent the robust Eurasian pattern throughout the remainder of the thesis. Its horizontal scale is large, stretching over the entire northern portion of Eurasia from the Baltic Sea to the Sea of Okhotsk. Linear regression was employed to demonstrate the Eurasian pattern's signature in upper-level geopotential height fields. This revealed a wavelike structure above 700 hPa, characterized by a positive anomaly centered slightly to the north of the surface center of action and negative centers over the Himalayas and western Europe. This vertical structure was contrasted with the two leading patterns of NH SLP variability for its striking differences near the surface. The largest temperature anomalies associated with the Eurasian pattern are located well to the north of the corresponding features in the geopotential height field. This was shown to be consistent with previous descriptions of continental teleconnections.

The EOT analysis was repeated using 500 hPa geopotential heights, and it was shown that a strong relationship exists between specific surface patterns and upper level patterns. This was result was found to be robust at other levels. Set in context with the strong relationship between higher order REOFs and EOTs (Table 3.6), this suggests that other reproducible, physically meaningful patterns may exist. For example, EOT4 of SLP resembles the Eastern Atlantic (EA) pattern described by Wallace and Gutzler (1981). Wettstein and Wallace (2009) related the EA pattern to a latitudinally shifting mode of storm track variability and an extension or retraction of the subpolar jet over the North Atlantic sector.

While the structure of EOT3 is clearly useful for describing variation in surface climate across northern Eurasia, it may also be of interest to investigators who wish to study Arctic variability. For example, the dipole configuration of EOF3 of SLP over the Arctic has been described in previous work (Overland and Wang, 2005). The gradient aligned across the pole shown in EOF3 suggests implications for Arctic temperature, winds, and concomitant sea ice motion. EOT3 also exhibits an anomalous pressure gradient across portions of the Arctic.

The patterns described in Chapter 3 should not be interpreted as a pure dynamical mode of variability, but rather as summarizing the dominant features of climate variability over northern Eurasia. That is to say, while the existence of the Eurasian pattern yielded by our analyses is clear to the extent that it is reproducible, its dynamical origins await further investigation. Such a task is beyond the reach of this thesis.

Having demonstrated the robustness of our results, the pronounced influence of the Eurasian pattern during winter epitomize their physical significance. Although the pattern explains a smaller fraction of SLP variance than either of the first two EOTs, it competes with the leading two modes for variance explained in SAT and global mean temperature (Table 7.1). Compared to EOT 4-6, the leading three modes are clearly distinguished by their ability to explain variability in global mean temperature. Each of the leading three EOTs plays a strong role in modulating the strength of zonal flow at high latitudes, the dynamical impetus of the COWL pattern. It was shown that EOT3 has the strongest relationship with a time series depicting the contrast in mean temperature between the NH land and ocean.

Regressions and composites demonstrated the influence of the Eurasian pattern on SAT across the northern portion of the supercontinent, characterized by cold monthly-mean anomalies under the positive polarity of the pattern and warm anomalies during the neg-

Table 7.1: Fraction of NH SLP, NH SAT, and global mean temperature (SAT_{GL}) variance explained by the first six EOTs of NH SLP. SLP and SAT variance explained values are determined by summing the product of a grid point's variance and its r^2 value with the EOT of interest, divided by the sum of the variance at all grid points. r^2 for global mean temperature is calculated simply by squaring the correlation between the EOT time series and the global mean temperature time series.

	EOT1	**EOT2**	**EOT3**	**EOT4**	**EOT5**	**EOT6**
SLP	18.5	10.9	9.8	7.4	6.9	6.5
SAT	11.7	3.6	7.1	1.6	3.0	4.9
SAT_{GL}	8.0	7.9	8.4	0.0	2.3	2.7

ative polarity. These anomalies were linked largely to advection of the climatological SAT gradient, which was shown to be aligned perpendicular to the anomalous winds over both regions of large anomalies: Svalbard and central Siberia.

The pattern's influence on precipitation was established via composites of precipitation relative to normal, which showed EOT3+ to be drier than normal over the continent and EOT3- to be wetter than normal. Deviations of up to 60% of the mean rainfall between the opposing polarities of the pattern were identified over northwestern Russia. The reduction of precipitation during the positive polarity of EOT3 was determined to be consistent with a weakening of the storm track across the continent during winter. The reduction in high frequency variance was demonstrated to be of the same order as the reduction associated with the negative polarity of the NAO (EOT1). It was also suggested that changes in precipitation associated with the Eurasian pattern are consistent with the leading rotated PC of Eurasian snow depth shown by Popova (2007). Those results suggest that EOT3- would be associated with increased snowfall, which is consistent with its association with increased precipitation.

Results of a brief investigation of the Eurasian pattern's time evolution were presented using pentad-mean data. A symmetric development and decay of anomalies was evident in a sequence of composite means. Downstream development of anomalies at 500 hPa was noted in both polarities of the pattern. Similar behavior has been previously documented with respect to the NAO (Rennert, 2007). A signature associated with Rossby wave-breaking and blocking of the zonal flow (Pelly and Hoskins, 2003) was seen in the composite evolution of the pattern's positive polarity. Through the recent work of Woollings et al. (2009), this led to the identification of modest skewness in the Eurasian pattern when defined at the surface and at 500 hPa.

Several of the questions examined throughout this thesis led naturally to questions that were beyond the purview of our investigation. The few examples listed here help to indicate some of the avenues left to future exploration:

- *Is the Eurasian pattern a natural mode of climate variability?*

- *If so, what are the physical mechanisms that contribute to its origin and structure?*

- *Does the pattern affect the variability of Arctic sea ice?*
- *Does Eurasian snow cover play a role in explaining the pattern's dominance during NH autumn and spring?*
- *What sort of interdecadal variability does the pattern exhibit?*
- *Does the skewness of the Eurasian pattern indicate regime behavior, as has been hypothesized with respect to the NAO?*

Overall, this thesis has identified a robust Eurasian pattern of wintertime SLP variability, described its three dimensional structure, and demonstrated its pronounced impacts on surface weather and climate across the supercontinent. In doing so, it has improved the description of Eurasian SLP variability during winter and offered a multifaceted approach toward confirming the robustness and physical significance of higher order patterns of variability.

BIBLIOGRAPHY

A. Ångström. Teleconnections of Climatic Changes in Present Time. *Geogr. Ann.*, 17:242 – 258, 1935.

A. S. Bamzai. Relationship between snow cover variability and Arctic oscillation index on a hierarchy of time scales. *Int. J. Climatol.*, 23:131 – 142, 2003.

A. G. Barnston and R. E. Livezey. Classification, Seasonality and Persistence of Low-Frequency Atmospheric Circulation Patterns. *Mon. Wea. Rev.*, 115:1086–1126, 1986.

A. G. Barnston and H. M. van den Dool. Toward Understanding the Causes of Low-Frequency Variability: The Interannual Standard Deviation of Monthly Mean 700-mb Height. *J. Climate*, 6:2083 – 2102, 1993.

J. Bjerknes. Atlantic air-sea interaction. *Adv. Geosci.*, 10:1 – 82, 1964.

M. L. Blackmon, Y.-H. Lee, and J. M. Wallace. Horizontal Structure of 500 mb Height Fluctuations with Long, Intermediate and Short Time Scales. *J. Atmos. Sci.*, 41:961 – 979, 1984.

G. Branstator. Circumglobal Teleconnections, the Jet Stream Waveguide, and the North Atlantic Oscillation. *J. Climate*, 15:1893 – 1910, 2002.

K. A. Brownslee. *Statistical Theory and Methodology in Science and Engineering.* John Wiley and Sons, 2nd edition, 1965.

C. Bueh and H. Nakamura. Scandinavian pattern and its climatic impact. *Quart. J. Roy. Meteor. Soc.*, 113:2117–2131, 2007.

W. Y. Chen and H. van den Dool. Sensitivity of Teleconnection Patterns to the Sign of Their Primary Action Center. *Mon. Wea. Rev.*, 131:2885 – 2898, 2003.

A. Defant. Die Schwankungen der atmospherischen Zirkulation über dem Nordatlantischen Ozean im 25-jährigen Zeitraum 1881 - 1905. *Geogr. Ann.*, 6:13 – 41, 1924.

R. M. Dole. Persistent Anomalies of the Extratropical Northern Hemisphere Wintertime Circulation: Structure. *Mon. Wea. Rev.*, 114:178–207, 1986.

R. M. Dole and N. D. Gordon. Persistent Anomalies of the Extratropical Northern Hemisphere Circulation: Geographical Distribution and Regional Persistence Characteristics. *Mon. Wea. Rev.*, 111:1567–1586, 1983.

D. Dommenget. Evaluating EOF modes against a stochastic null hypothesis. *Clim. Dynam.*, 28:517–531, 2007.

S. J. Eichelberger and D. L. Hartmann. Zonal Jet Structure and the Leading Mode of Variability. *J. Climate*, 20:5149 – 5163, 2007.

S. K. Esbensen. A comparison of intermonthly and interannual teleconnections in the 700 mb geopotential height field during the Northern Hemisphere winter. *Mon. Wea. Rev.*, 112:2016 – 2032, 1984.

F. M. Exner. Über monatliche Witterunganomalien auf der nördliche Erdhälfte im Winter. *Sitz. Kais. Akad. Wiss. Wien*, 122:1165 – 1240, 1913.

F. M. Exner. Monatliche Luftdruck und Temperaturanomalien auf der Erde. *Sitz. Kais. Akad. Wiss. Wien*, 133:306 – 408, 1924.

C. Franzke. Dynamics of Low-Frequency Variability: Barotropic Mode. *J. Atmos. Sci.*, 59: 2897 – 2909, 2002.

C. Franzke and S. B. Feldstein. The Continuum and Dynamics of Northern Hemisphere Teleconnection Patterns. *J. Atmos. Sci.*, 62:3250 – 3267, 2005.

W. Freiberger and U. Grenander. On the Formulation of Statistical Meteorology. *Rev. Intern. Statist. Inst.*, 33:59–86, 1965.

A. Fukuoka. A Study on 10-day Forecast (A Synthetic Report). *Geophys. Mag.*, 22:177 – 208, 1951.

M. Grimmer. The space-filtering of monthly surface temperature anomaly data in terms of pattern, using empirical orthogonal functions. *Quart. J. Roy. Meteor. Soc.*, 89:395–408, 1963.

L. Guttmann. Some necessary conditions for common factor analysis. *Psychometrika*, 19: 149–161, 1954.

D. S. Gutzler, R. D. Rosen, and D. A. Salstein. Patterns of Interannual Variability in the Northern Hemisphere Wintertime 850 mb Temperature Field. *J. Climate*, 1:949–964, 1988.

A. Hannachi. Pattern hunting in climate: a new method for finding trends in gridded climate data. *Int. J. Climatol.*, 27:1–15, 2007.

A. Hannachi. A New Set of Orthogonal Patterns in Weather and Climate: Optimally Interpolated Patterns. *J. Climate*, 21:6724 – 6738, 2008.

A. Hannachi, I. T. Jolliffe, D. B. Stephenson, and N. Trendafilov. In search of simple structures in climate: Simplifying EOFs. *Int. J. Climatol.*, 26:7–28, 2006.

A. Hannachi, I. T. Jolliffe, and D. B. Stephenson. Empirical orthogonal functions and related techniques in atmospheric science: A review. *Int. J. Climatol.*, 27:1119–1152, 2007.

H. H. Hildebrandsson. Quelques recherches sur les centres d'action de l'atmosphere. *Kon. Svenska Vetens. Akad. Handl.*, No. 29:36 pp., 1897.

J. R. Holton and H.-C. Tan. The Influence of the Equatorial Quasi-Biennial Oscillation on the Global Circulation at 50 mb. *J. Atmos. Sci.*, 37:2200 – 2208, 1980.

J. D. Horel. A Rotated Principal Component Analysis of the Interannual Variability of the Northern Hemisphere 500 mb Height Field. *Mon. Wea. Rev.*, 109:2080–2092, 1981.

B. J. Hoskins and T. Ambrizzi. Rossby Wave Propagation on a Realistic Longitudinally Varying Flow. *J. Atmos. Sci.*, 50:1661 – 1671, 1993.

H.-H. Hsu and S.-H. Lin. Global Teleconnections in the 250-mb Streamfunction Field during the Northern Hemisphere Winter. *Mon. Wea. Rev.*, 120:1169 – 1190, 1992.

H.-H. Hsu and J. M. Wallace. Vertical structure of wintertime teleconnection patterns. *J. Atmos. Sci.*, 42:1693 – 1710, 1985.

J. W. Hurrell. Decadal Trends in the North Atlantic Oscillation: Regional Temperatures and Precipitation. *Science*, 269:676 – 679, 1995.

I. T. Jolliffe. *Principal Component Analysis*. Springer, 2nd edition, 2002.

H. F. Kaiser. The Varimax Criterion for Analytic Rotation in Factor Analysis. *Psychometrika*, 23:187–200, 1958.

E. Kalnay and Coauthors. The NCEP-NCAR 40-Year Reanalysis Project. *Bull. Amer. Meteor. Soc.*, 77:437–471, 1996.

R. Kawamura. A Rotated EOF Analysis of Global Sea Surface Temperature Variability with Interannual and Interdecadal Scales. *J. Phys. Oceanogr.*, 24:707 – 715, 1994.

J. W. Kidson. Temporal and Spatial Scales of the Arctic Circulation. *Mon. Wea. Rev.*, 103: 1532–1544, 1975.

Y. Kushnir and J. M. Wallace. Low-frequency variability in the Northern Hemisphere winter: Geographical distribution, structure, and time-scale dependence. *J. Atmos. Sci.*, 46:3122 – 3142, 1989.

J. E. Kutzbach. Empirical Eigenvectors of Sea-Level Pressure, Surface Temperature and Precipitation Complexes over North America. *J. Appl. Meteor.*, 6:791–802, 1967.

J. E. Kutzbach. Large-scale features of monthly mean Northern Hemisphere anomaly maps of sea-level pressure. *Mon. Wea. Rev.*, 98:708 – 716, 1970.

N.-C. Lau and K.-M. Lau. The Structure and Energetics of Midlatitude Disturbances Accompanying Cold-Air Outbreaks over East Asia. *Mon. Wea. Rev.*, 112:1309 – 1327, 1984.

M. E. Linkin and S. Nigam. The North Pacific Oscillation-West Pacific Teleconnection Pattern: Mature-Phase Structure and Winter Impacts. *J. Climate*, 21:1979 – 1997, 2008.

E. N. Lorenz. Empirical Orthogonal Functions and Statistical Weather Prediction. Scientific Report No. 1, Statistical Forecasting Project, M.I.T. Dept. of Meteorology, 1956. Air Force Research Laboratories, Office of Aerospace Research, USAF.

J. M. Mitchell, B. Dzerdzeevkii, H. Flohn, W. L. Hofmeyr, H. H. Lamb, K. N. Rao, and C. C. Wallèn. Climatic change. Tech. Note No. 75, WMO-No. 195, TP. 100, World Meteorological Organization, 1966.

T. D. Mitchell and P. D. Jones. An improved method of constructing a database of monthly climate observations and associated high-resolution grids. *Int. J. Climatol.*, 25:693 – 712, 2005.

K. C. Mo and G. H. White. Teleconnections in the Southern Hemisphere. *Mon. Wea. Rev.*, 113:22 – 37, 1985.

G. R. North, T. L. Bell, R. F. Cahalan, and F. J. Moeng. Sampling errors in the estimation of empirical orthogonal functions. *Mon. Wea. Rev.*, 110:699–706, 1982.

J. E. Overland and M. Wang. The third Arctic climate pattern: 1930s and early 2000s. *Geophys. Res. Lett.*, 32, 2005.

F. Panagiotopoulos, M. Shahgedanova, A. Hannachi, and D. B. Stephenson. Observed Trends and Teleconnections of the Siberian High: A Recently Declining Center of Action. *J. Climate*, 18:1411–1422, 2005.

J. L. Pelly and B. J. Hoskins. A New Perspective on Blocking. *J. Atmos. Sci.*, 60:743 – 755, 2003.

V. Popova. Winter snow depth variability over northern Eurasia in relation to recent atmospheric circulation changes. *Int. J. Climatol.*, 27:1721 – 1733, 2007.

R. W. Preisendorfer, F. W. Zwiers, and T. P. Barnett. Foundations of Principal Component Selection Rules. Rep. SIO Ref. 81-4, Scripps Institute of Oceanography, 1981.

B. Qian, J. Corte-Real, and H. Xu. Is the North Atlantic Oscillation the most important atmospheric pattern for precipitation in Europe? *J. Geophys. Res.*, 105:11901–11910, 2000.

R. Quadrelli and J. M. Wallace. A Simplified Linear Framework for Interpreting Patterns of Northern Hemisphere Wintertime Climate Variability. *J. Climate*, 17:3728–3744, 2004.

K. Rennert. *Relationships Between Wintertime Modes of Atmospheric Variability on Intermediate and Long Timescales*. PhD thesis, University of Washington, 2007.

R. W. Reynolds, N. A. Rayner, T. M. Smith, and D. C. Stokes. An Improved In Situ and Satellite SST Analysis for Climate. *J. Climate*, 15:1609 – 1625, 2002.

M. B. Richman. Rotation of principle components. *Int. J. Climatol.*, 6:293–335, 1986.

C. F. Ropelewski and M. S. Halpert. Global and Regional Scale Precipitation Patterns Associated with the El Niño/Southern Oscillation. *Mon. Wea. Rev.*, 115:1606 – 1626, 1987.

S. C. Scherrer, M. Croci-Maspoli, C. Schwierz, and C. Appenzeller. Two-Dimensional Indices of Atmospheric Blocking and their Statistical Relationship with Winter Climate Patterns in the Euro-Atlantic Region. *Int. J. Climatol.*, 26:233–249, 2006.

A. J. Simmons, J. M. Wallace, and G. W. Branstator. Barotropic Wave Propagation and Instability, and Atmospheric Teleconnection Patterns. *J. Atmos. Sci.*, 40:1363 – 1392, 1983.

D. B. Stephenson, H. Wanner, and S. Brönnimann. The History of Scientific Research on the North Atlantic Oscillation. In J. W. Hurrell, Y. Kushnir, G. Ottersen, and M. Visbeck, editors, *The North Atlantic Oscillation: Climatic Significance and Environmental Impact*, number 134 in Geophysical Monograph Series, pages 37 – 50. American Geophysical Union, 2003.

K. Takaya and H. Nakamura. Mechanisms of Intraseasonal Amplification of the Cold Siberian High. *J. Atmos. Sci.*, 62:4423 – 4440, 2005a.

K. Takaya and H. Nakamura. Geographical Dependence of Upper-Level Blocking Formation Association with Intraseasonal Amplification of the Siberian High. *J. Atmos. Sci.*, 62: 4441 – 4449, 2005b.

L. P. Teisserenc de Bort. Etude sur l'hiver de 1879-80 et recherches sur l'influence de la position des grands centres d'action de l'atmosphere dans les hivers anormaux. *Ann. Soc. Meteor. France*, 31:70 – 79, 1883.

D. W. J. Thompson and J. M. Wallace. The Arctic oscillation signature in the wintertime geopotential height and temperature fields. *Geophys. Res. Lett.*, 25:1297–1300, 1998.

D. W. J. Thompson and J. M. Wallace. Annular Modes in the Extratropical Circulation. Part I: Month-to-Month Variability. *J. Climate*, 13:1000 – 1016, 2000.

D. W. J. Thompson and J. M. Wallace. Regional Climate Impacts of the Northern Hemisphere Annular Mode. *Science*, 293:85–89, 2001.

D. W. J. Thompson, J. M. Wallace, and G. C. Hegerl. Annular Modes in the Extratropical Circulation. Part II: Trends. *J. Climate*, 13:1018 – 1036, 2000.

D. W. J. Thompson, J. M. Wallace, P. D. Jones, and J. J. Kennedy. Removing the signatures of known climate variability from global-mean surface temperature: Methodology and Insights. *J. Climate*, 2009. Submitted.

L. L. Thurstone. *Theory of multiple factors*. Edward Bros., Ann Arbor, 1932.

L. L. Thurstone. *Multiple-factor analysis*. Chicago Press, Chicago, 1947.

K. E. Trenberth and D. A. Paolino. Characteristic Patterns of Variability of Sea Level Pressure in the Northern Hemisphere. *Mon. Wea. Rev.*, 109:1169 – 1189, 1980.

K. E. Trenberth and W. K. Shin. Quasi-Biennial Fluctuations in Sea Level Pressures over the Northern Hemisphere. *Mon. Wea. Rev.*, 112:761–777, 1984.

A. A. Tsonis, K. L. Swanson, and G. Wang. On the Role of Atmospheric Teleconnections in Climate. *J. Climate*, 21:2990 – 3001, 2008.

S. Uppala and coauthors. The ERA-40 re-analysais. *Quart. J. Roy. Meteor. Soc.*, 131: 2961–3012, 2005.

H. M. van den Dool, S. Saha, and Å. Johansson. Empirical Orthogonal Teleconnections. *J. Climate*, 13:1421 – 1435, 2000.

G. van der Schrier, K. R. Briffa, P. D. Jones, and T. J. Osborn. Summer Moisture Variability across Europe. *J. Climate*, 19:2818 – 2834, 2006.

H. van Loon and J. C. Rogers. The Seesaw in Winter Temperatures between Greenland and Northern Europe. Part I: General Description. *Mon. Wea. Rev.*, 106:296 – 310, 1978.

G. T. Walker. Correlation in seasonal variation of climate. *Mem. Ind. Met. Dept.*, 20:117 – 124, 1909.

G. T. Walker. On the meteorological evidence for supposed changes of climate in india. *Mem. Ind. Met. Dept.*, 21:1 – 21, 1910.

G. T. Walker. Correlation in seasonal variation of weather, IX. *Mem. Ind. Met. Dept.*, 25: 275 – 332, 1924.

G. T. Walker and E. W. Bliss. World Weather V. *Mem. R. Meteor. Soc.*, 4:53 – 83, 1932.

J. M. Walker. Pen portrait of sir gilbert walker, CSI, MA, ScD, FRS. *Weather*, 52:217 – 220, 1997.

J. M. Wallace. North Atlantic Oscillation/Annular Mode: Two paradigms-one phenomenon. *Quart. J. Roy. Meteor. Soc.*, 126:791 – 805, 2000.

J. M. Wallace and D. S. Gutzler. Teleconnections in the Geopotential Height Field during the Northern Hemisphere Winter. *Mon. Wea. Rev.*, 109:784–812, 1981.

J. M. Wallace, Y. Zhang, and J. A. Renwick. Dynamic Contribution to Hemispheric Mean Temperature Trends. *Science*, 270:780 – 782, 1995.

J. J. Wettstein. *Storm Track Variability and Interaction with the Background Flow on Daily, Interannual and Climate Change Time Scales.* PhD thesis, University of Washington, 2007.

J. J. Wettstein and J. M. Wallace. Observed Modes of Interannual Storm Track Variability and their Relationship to the Background Flow. *J. Atmos. Sci.*, 2009. Submitted.

J. Wibig. Precipitation in Europe in Relation to Circulation Patterns at the 500 hPa Level. *Int. J. Climatol.*, 19:253–269, 1999.

D. S. Wilks. *Statistical Methods in the Atmospheric Sciences.* Academic Press, 2nd edition, 2006.

T. Woollings, B. J. Hoskins, M. Blackburn, and P. Berrisford. A New Rossby Wave-Breaking Interpretation of the North Atlantic Oscillation. *J. Atmos. Sci.*, 65:609 – 626, 2008.

T. Woollings, A. Hannachi, B. Hoskins, and A. G. Turner. A regime view of the North Atlantic Oscillation and its response to anthropogenic forcing. *J. Climate*, 2009. Submitted.

P. B. Wright. An Index of the Southern Oscillation. Cru rp4, Climatic Research Unit, School of Environmental Sciences, University of East Anglia, 1975.

Z. Zijiang and Z. Guocai. Typical severe dust storms in northern China during 1954 - 2002. *Chinese Sci. Bull.*, 48:2366–2370, 2003.

Appendix A

SENSITIVITY OF SECTORAL EOF RESULTS

Appendix A shows the insensitivity of sectoral EOF results to the size of the sector analyzed by examining the leading pattern obtained from sectoral analyses of varying domain sizes. Figures A.1 through A.4 each exhibit 12 maps depicting the leading EOF of sectoral EOF analyses performed using domains with widths of 180, 150, 120, and 90° longitude centered at 30° intervals. Figure A.5 shows the correlation between the leading principal component from each analysis with the time series associated with the first three EOTs of NH SLP, illustrating the robust regional separation of the patterns. Strong similarities are observed between the curves corresponding to different sector widths. Hence, our results are largely insensitive to the choice of sector size.

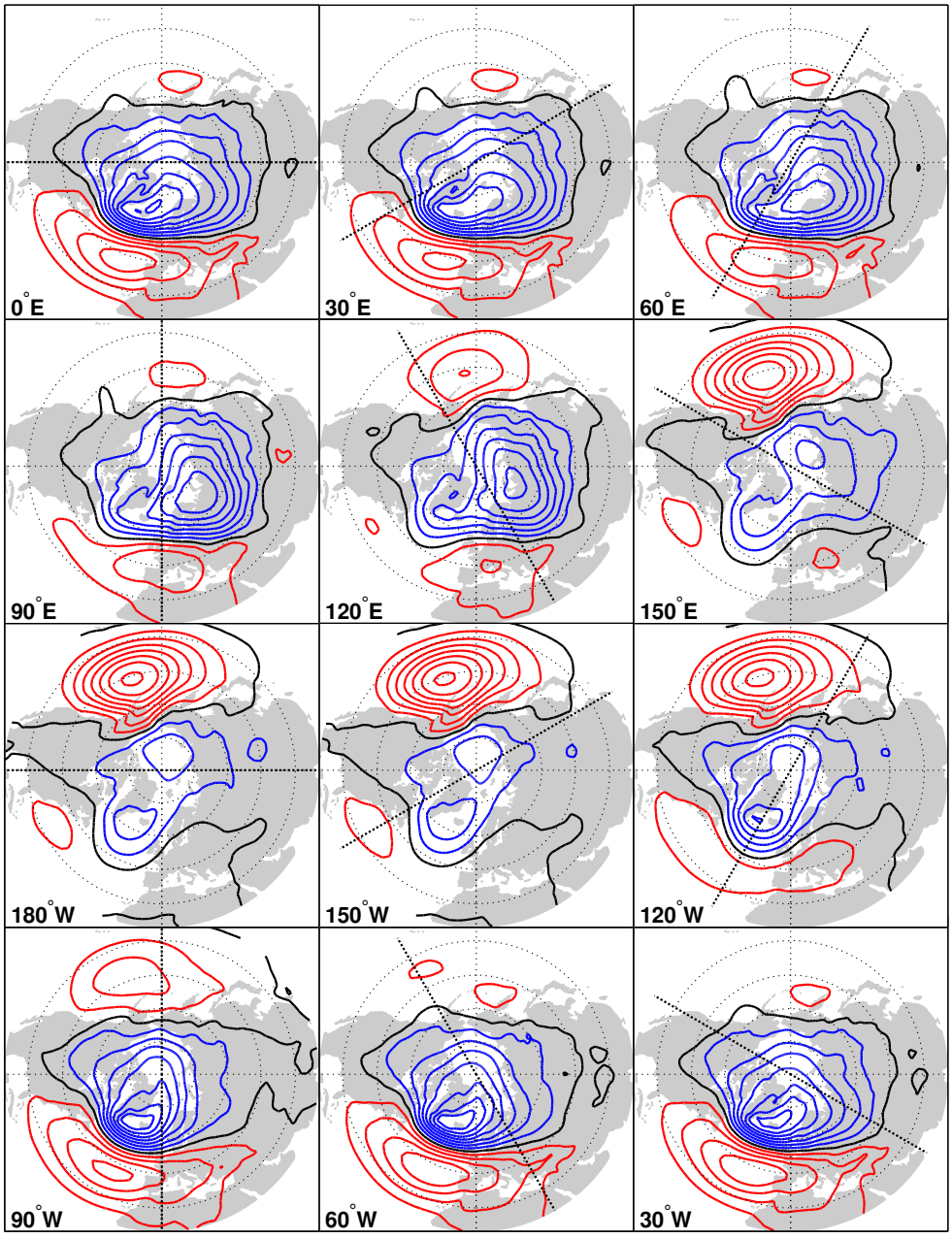

Fig. A.1: Regression maps formed by regressing monthly-mean DJFM SLP anomalies onto the leading principal component yielded from an EOF analysis performed using SLP anomalies over a NH domain of 180° longitude. Analysis domain indicated by dotted lines; center longitude shown in the lower left of each panel.

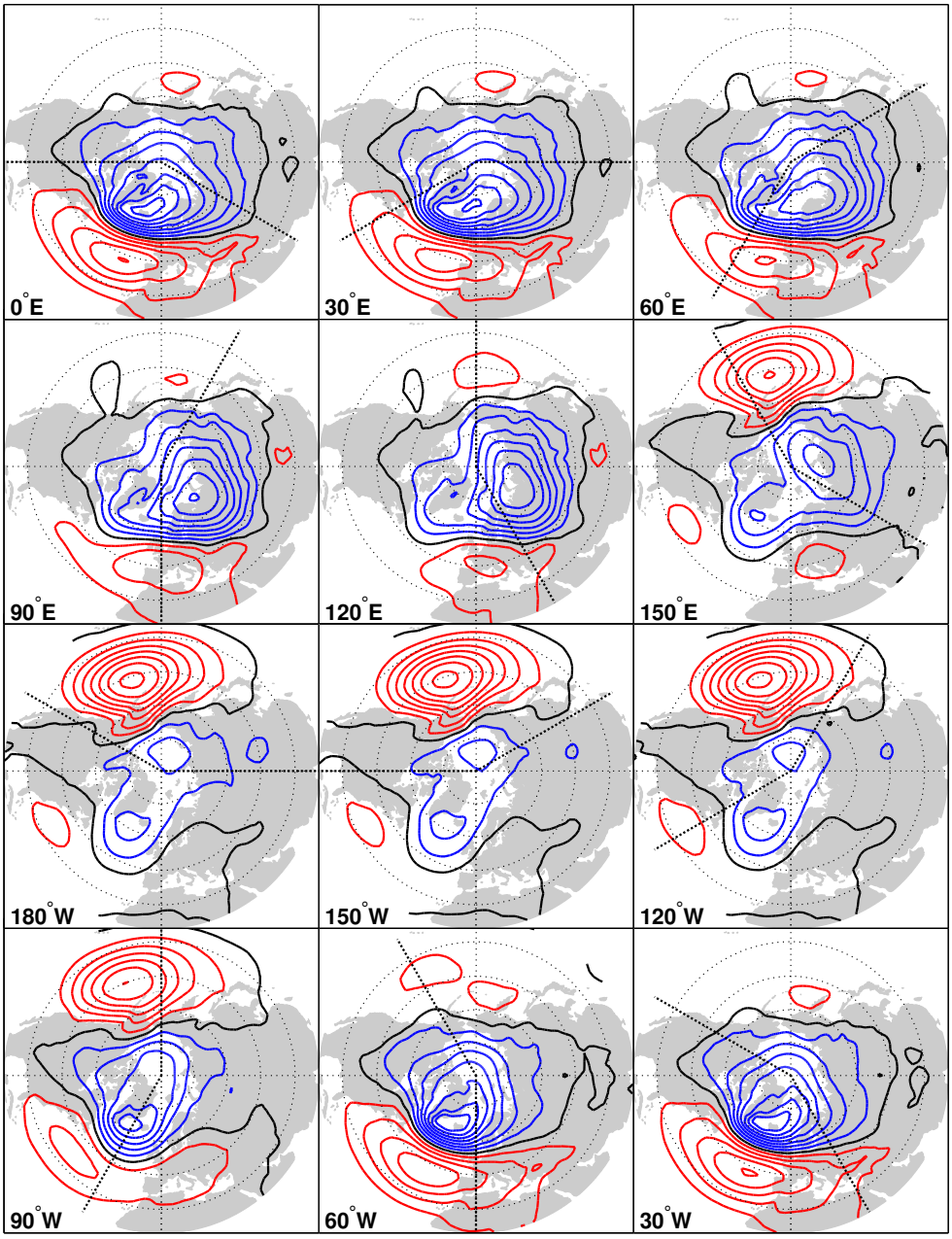

Fig. A.2: Display as in Fig. A.1, except for 150° domains.

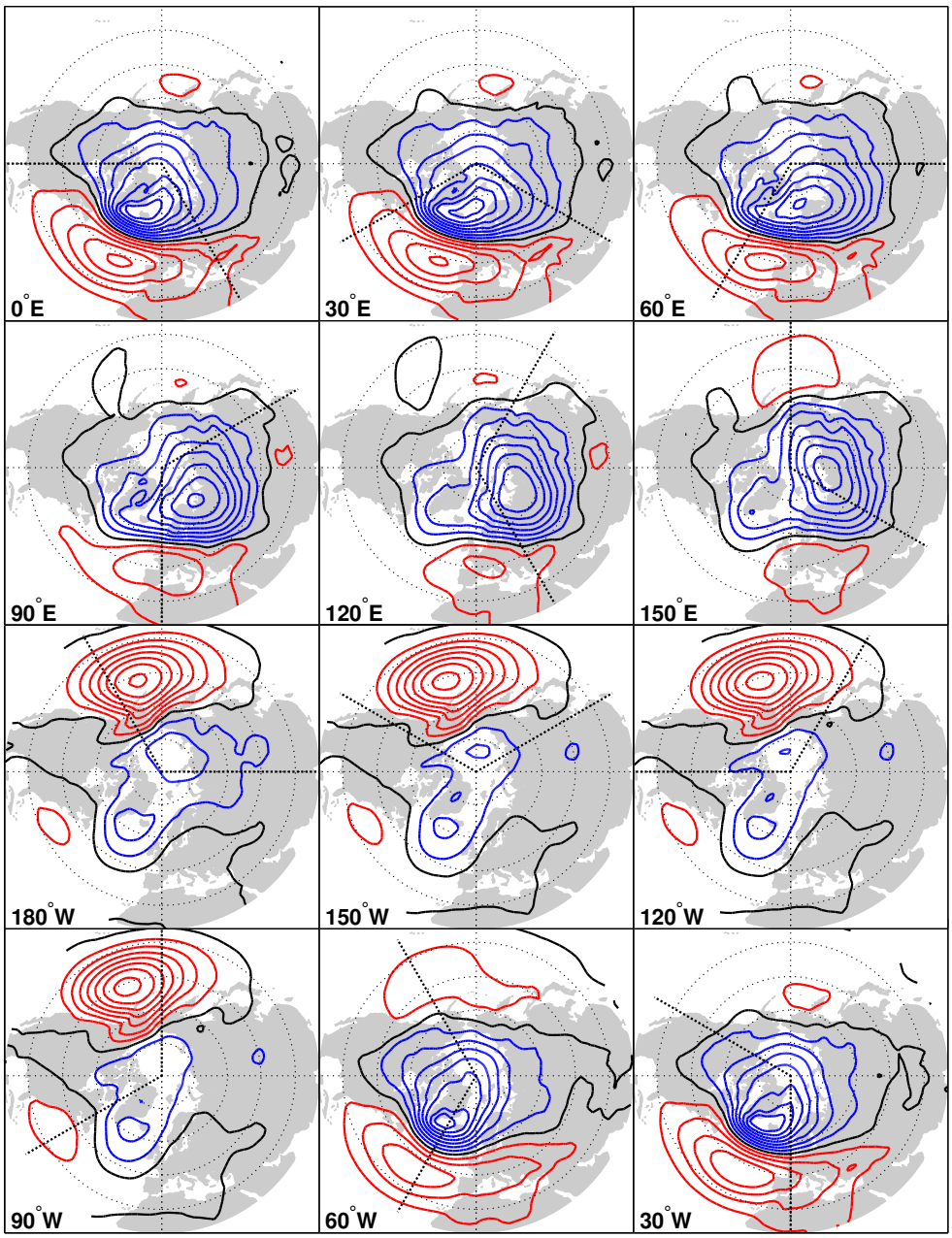

Fig. A.3: Display as in Fig. A.1, except for 120° domains.

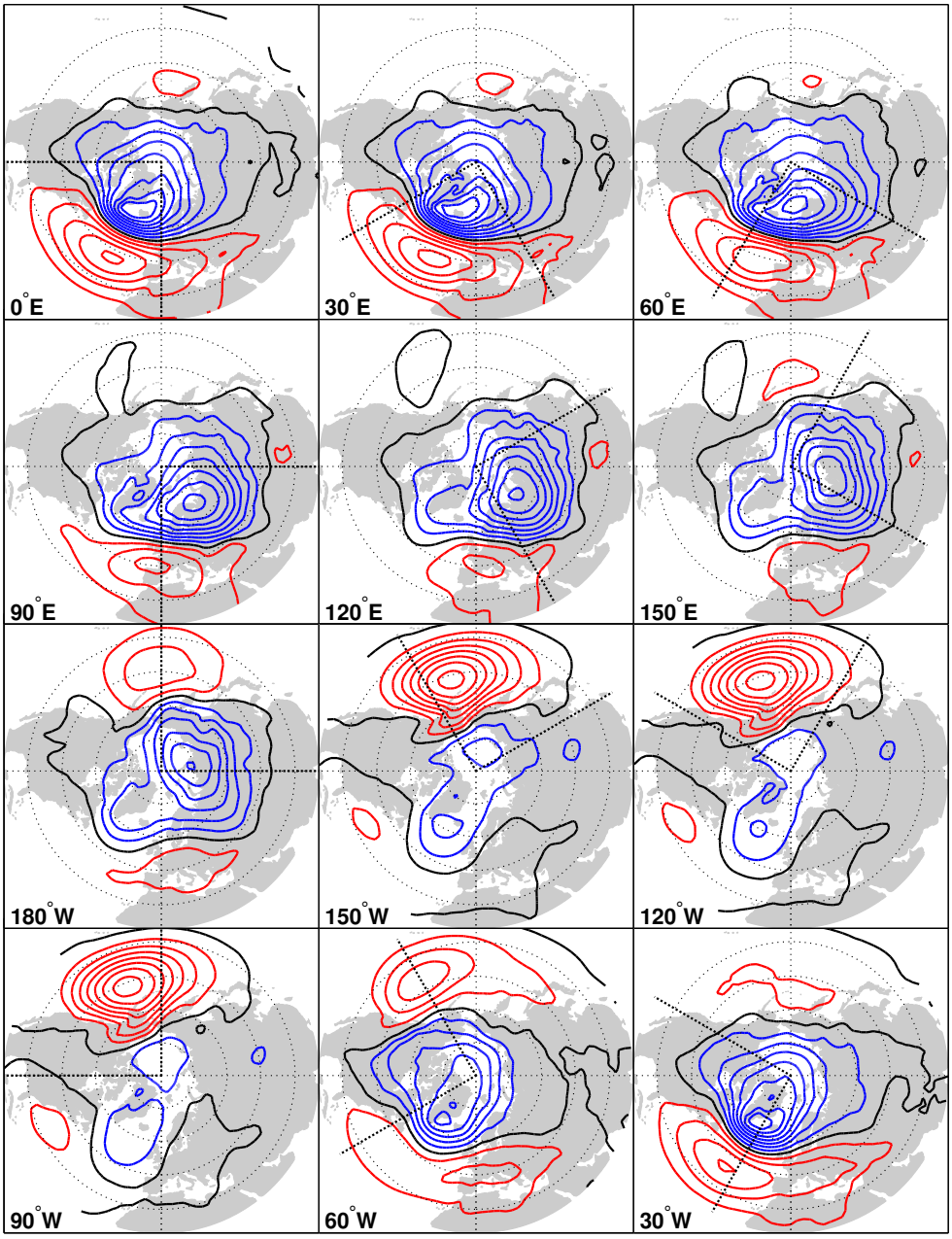

Fig. A.4: Display as in Fig. A.1, except for 90° domains.

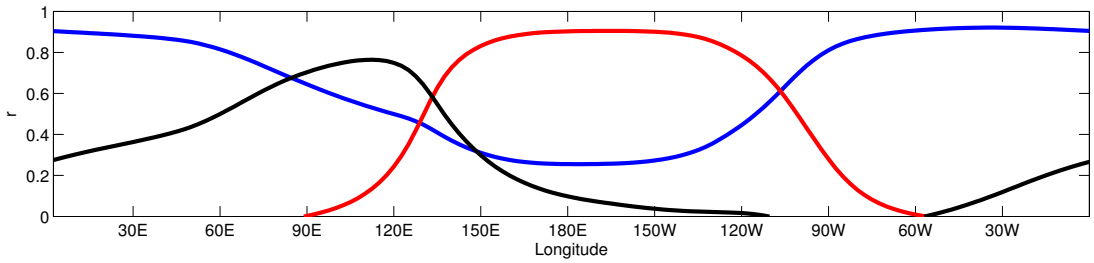

(a) 180° Sectors

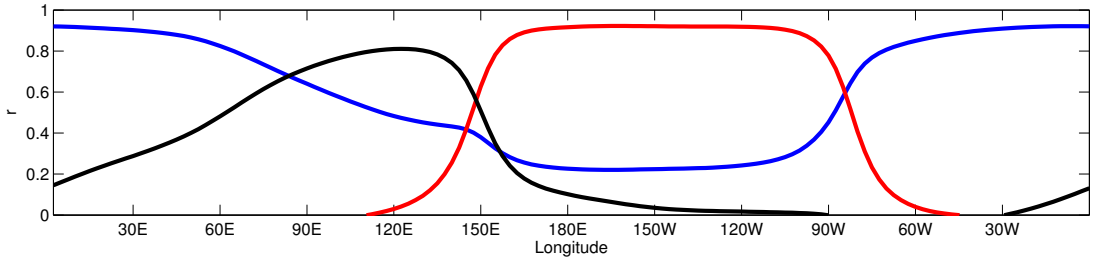

(b) 150° Sectors

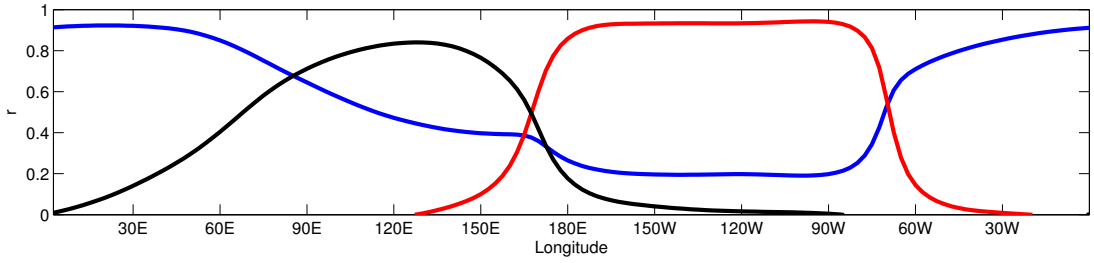

(c) 120° Sectors

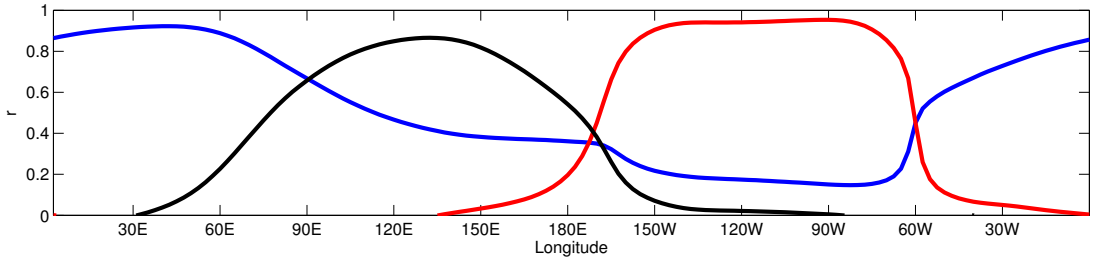

(d) 90° Sectors

Fig. A.5: Correlations between the standardized expansion coefficient time series associated with the leading three EOTs and the leading principal component from an EOF analysis performed on domains of (A.5a) 180°, (A.5b) 150°, (A.5c) 120°, (A.5d) 90° longitude. Ordinate, correlation coefficient; abscissa, central longitude of each domain. EOT1, blue line; EOT2, red line; EOT3, black line.

Appendix B

COMPARISON OF LEADING THREE PATTERNS OF WINTERTIME NH SLP VARIABILITY

This appendix summarizes and compares the leading three patterns of wintertime NH SLP variability obtained by the analyses described in Chapter 2, extending the results shown in the summary section of Chapter 3. Each of the three leading patterns is compared to the corresponding patterns obtained from the other three analyses, as well as a previously described pattern. The first leading pattern is compared to the Arctic Oscillation (AO) described by (Thompson and Wallace, 1998, 2000). The second leading pattern is compared to an index of the Pacific North American (PNA) pattern. This projection index is formed by regressing area-weighted SLP anomalies onto the index defined by Wallace and Gutzler (1981) at 500 hPa and then projecting the regression pattern onto area-weighted SLP anomalies. The third leading pattern is compared to an index representing the strength of the Siberian High, used previously by Panagiotopoulos et al. (2005).

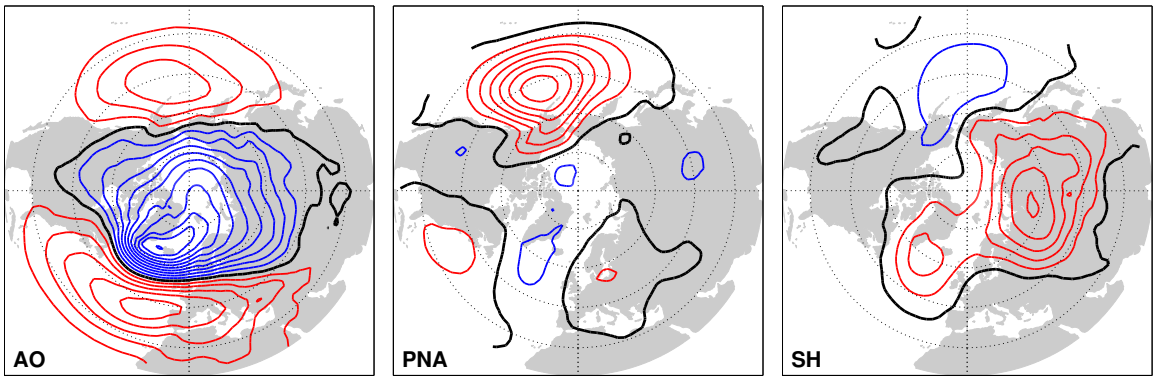

Fig. B.1: SLP loading patterns associated with the Arctic Oscillation (AO), Pacific North American (PNA), and SH (Siberian High) indices. Contour interval is 1 hPa. Zero contour shown in bold black.

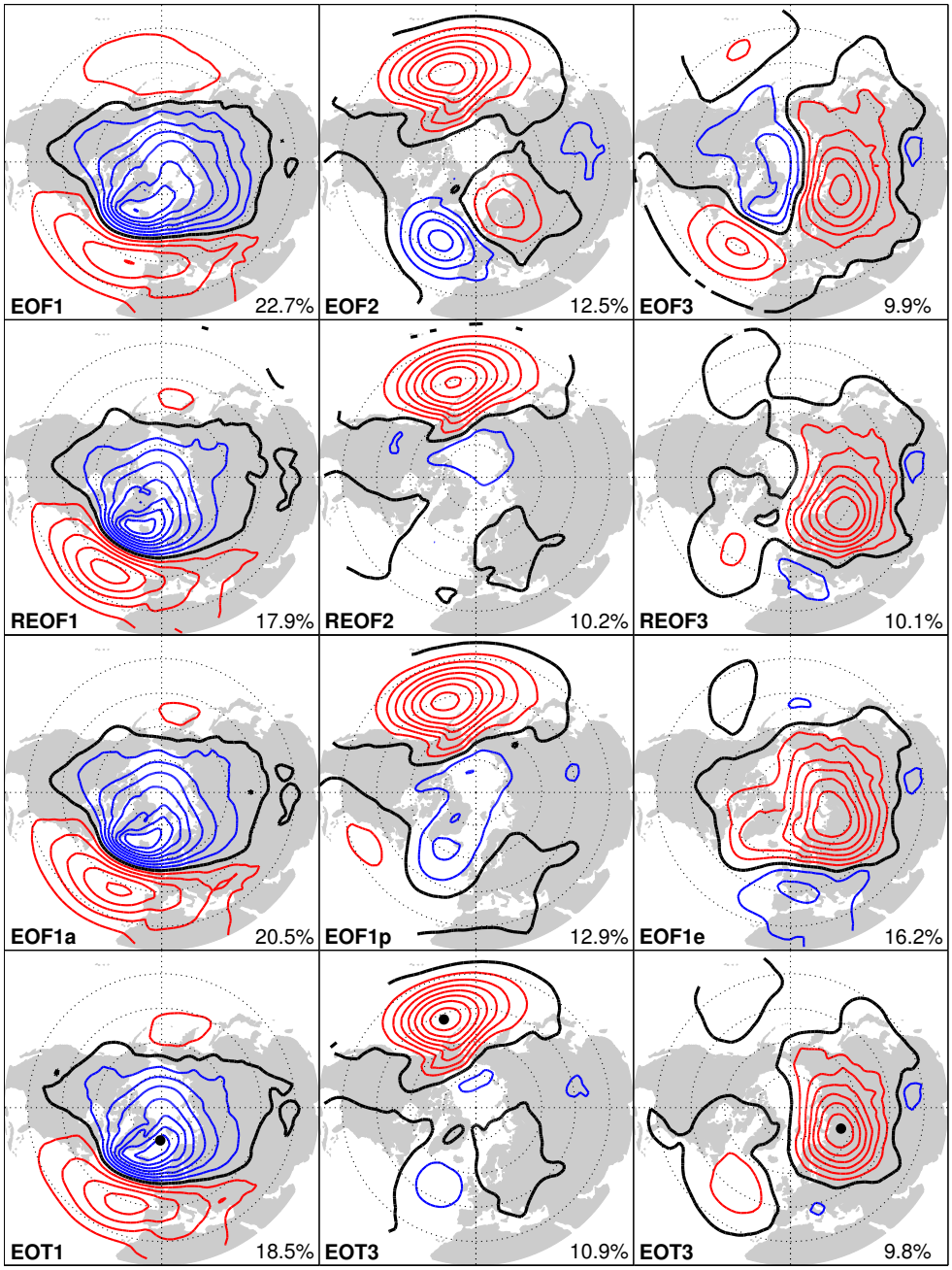

Fig. B.2: Summary of leading three patterns of NH SLP variability obtained from EOF, rotated EOF, sectoral EOF, and EOT analyses described in Chapter 2. Fraction of domain SLP variance explained by each pattern indicated in lower right corner. Contour interval is 1 hPa. Zero contour shown in bold black.

Table B.1: Temporal correlation coefficients between the respective expansion coefficient time series associated with EOF1, Atlantic sector EOF1 (EOF1a), REOF1, EOT1, and a monthly-mean Arctic Oscillation (AO) index.

	EOF1	**EOF1a**	**REOF1**	**EOT1**	**AO**
EOF1	1.00	0.91	0.82	0.88	0.98
EOF1a	0.91	1.00	0.96	0.91	0.90
REOF1	0.82	0.96	1.00	0.81	0.82
EOT1	0.88	0.91	0.81	1.00	0.87
AO	0.98	0.90	0.82	0.87	1.00

Table B.2: Temporal correlation coefficients between the respective expansion coefficient time series associated with EOF2, Pacific sector EOF1 (EOF1p), REOF2, EOT2 and a monthly-mean Pacific North American (PNA) index, defined by projecting SLP anomalies onto the PNA time series defined by Wallace and Gutzler (1981) at 500 hPa.

	EOF2	**EOF1p**	**REOF2**	**EOT2**	**PNA**
EOF2	1.00	0.87	0.75	0.86	0.77
EOF1p	0.87	1.00	0.90	0.94	0.85
REOF2	0.75	0.90	1.00	0.87	0.73
EOT2	0.86	0.94	0.87	1.00	0.87
PNA	0.77	0.85	0.73	0.87	1.00

Table B.3: Temporal correlation coefficient for time series associated with EOF3, Eurasian sector EOF1 (EOF1e), REOF3, EOT3, and an index of mean SLP anomalies in the core of the Siberian High, formed in the same manner as Panagiotopoulos et al. (2005).

	EOF3	**EOF1e**	**REOF3**	**EOT3**	**SH**
EOF3	1.00	0.66	0.81	0.84	0.60
EOF1e	0.66	1.00	0.80	0.84	0.68
REOF3	0.81	0.80	1.00	0.84	0.65
EOT3	0.84	0.84	0.84	1.00	0.66
SH	0.60	0.68	0.65	0.66	1.00

Appendix C

WINTERTIME EOT ATLAS

Appendix C shows a series of figures depicting aspects of the first 12 EOTs of wintertime NH SLP, based on the same 50 years of NCEP-NCAR reanalysis data used throughout this thesis. Several chapters alluded to higher order EOTs. Here we provide a set of figures that document their structure, upper level signature, and correlation with surface air temperature and precipitation.

Figure C.1 reproduces a portion of Fig. 1.1 to show the SLP variance of the total SLP field and the amount of domain variance explained by single grid points before any variance associated with EOTs has been explained.

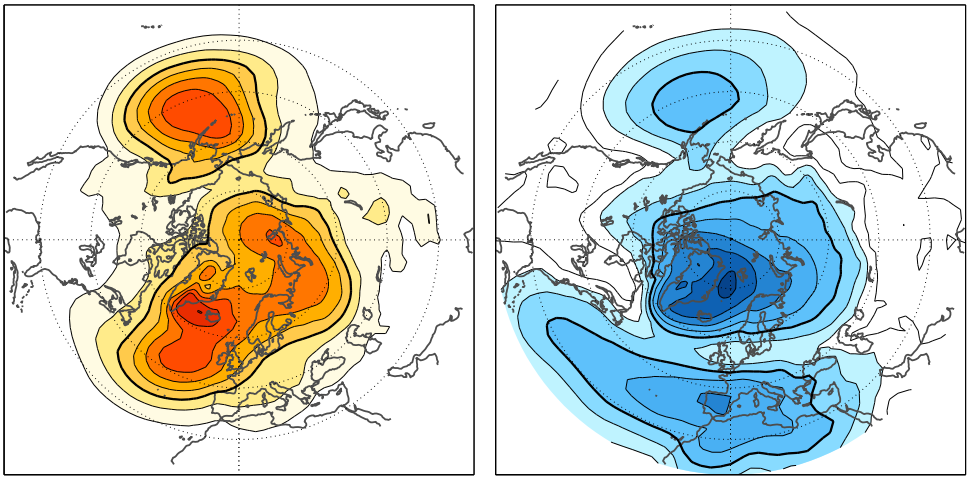

Fig. C.1: (Left) Variance of monthly-mean DJFM SLP, Dec. 1958 – Mar. 2008. Contour interval is 10 hPa^2; bold reference contour is 30 hPa^2. (Right) Domain SLP variance explained by the one-point covariance maps for individual grid points. Contour interval is 2%; bold reference contour is 10%.

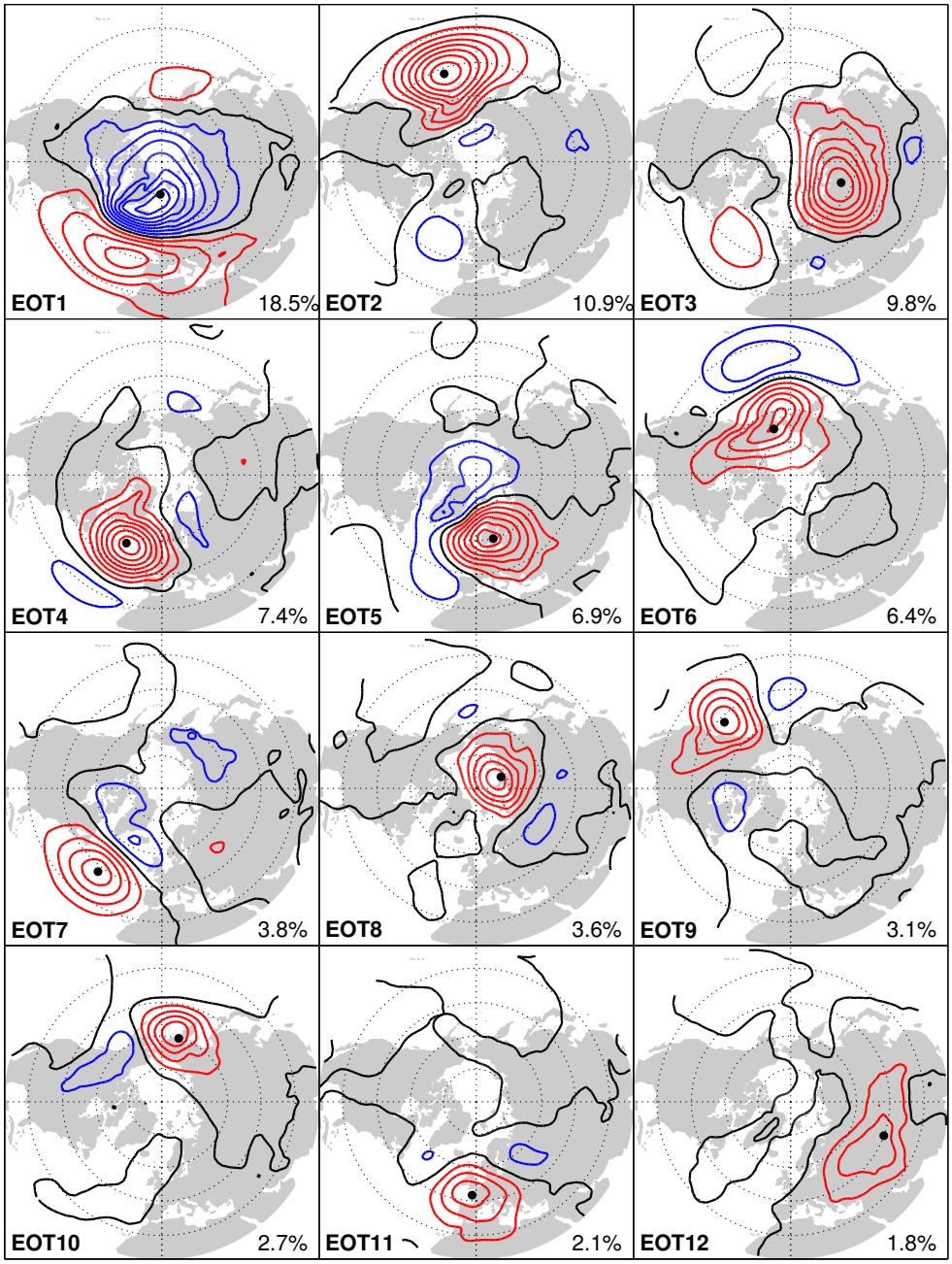

Fig. C.2: First 12 spatial patterns (EOT) associated with the Empirical Orthogonal Teleconnection analysis of monthly SLP anomalies derived from monthly-mean NCEP-NCAR reanalysis data. Contour interval is 1 hPa per std dev anomaly of the respective EOT time series. Domain variance explained by each pattern is shown at the bottom right of each panel. Positive contours are shown in red, negative in blue, and the zero contour in thick black.

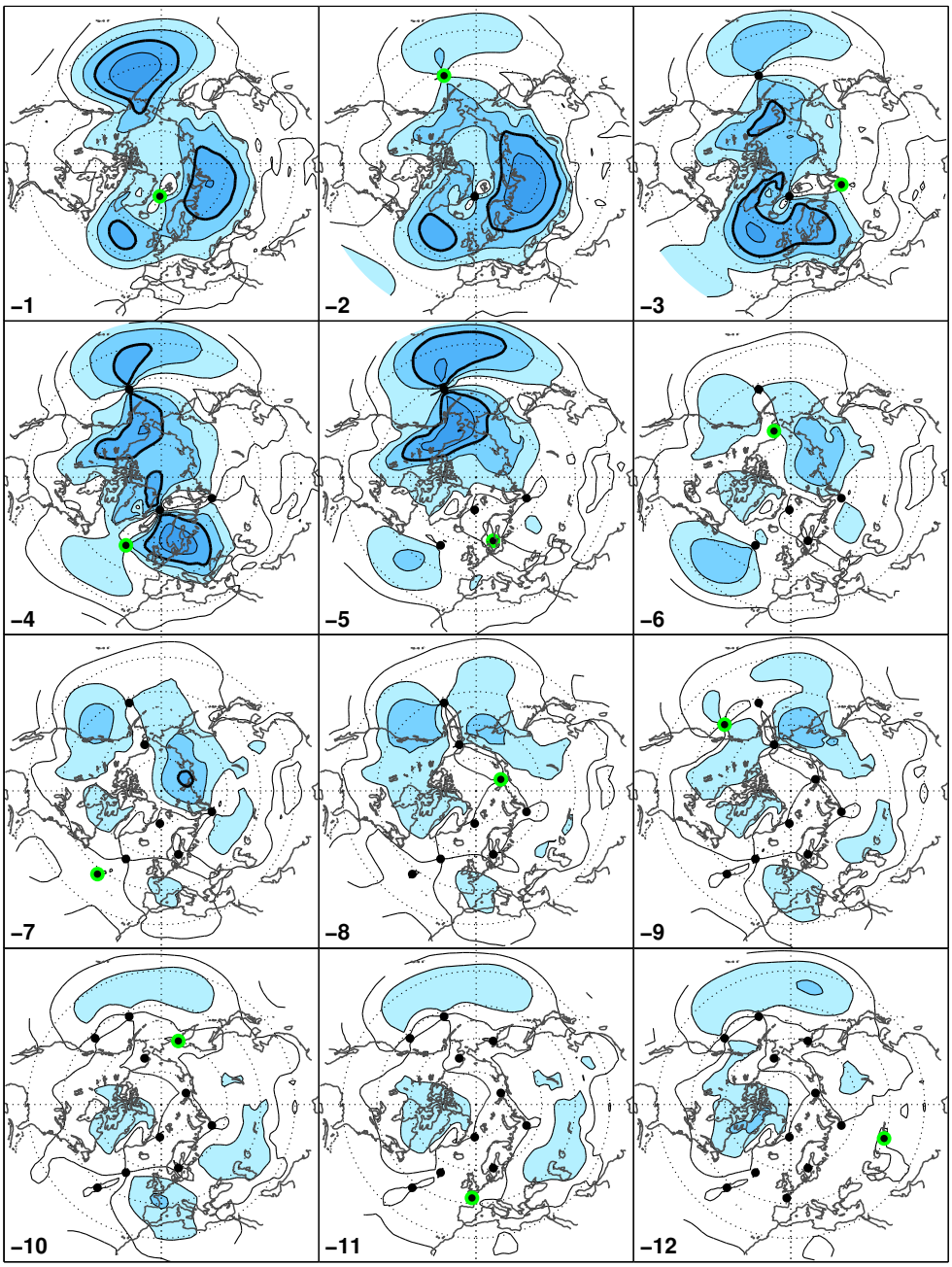

Fig. C.3: Variance explained in X_r after successive EOTs have been removed. Contour interval is 2%. Bold reference contour is 10%. EOT base points shown with black dots. The most recently selected EOT is shown with a black dot outlined in green.

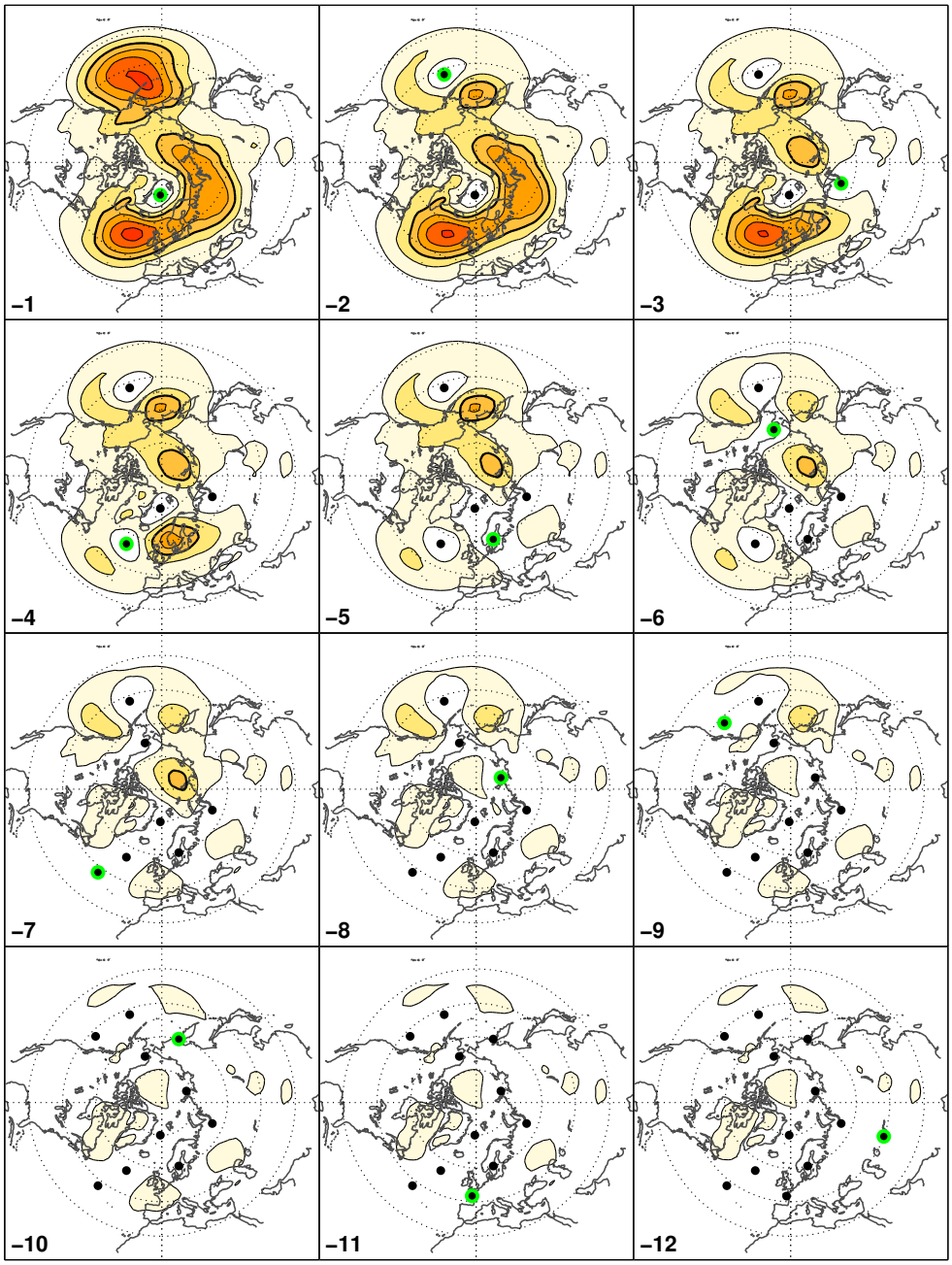

Fig. C.4: SLP variance in X_r after successive EOTs have been removed. Contour interval is 10 hPa^2. Bold reference contour is 30 hPa^2. Display of EOT base points same as in C.3.

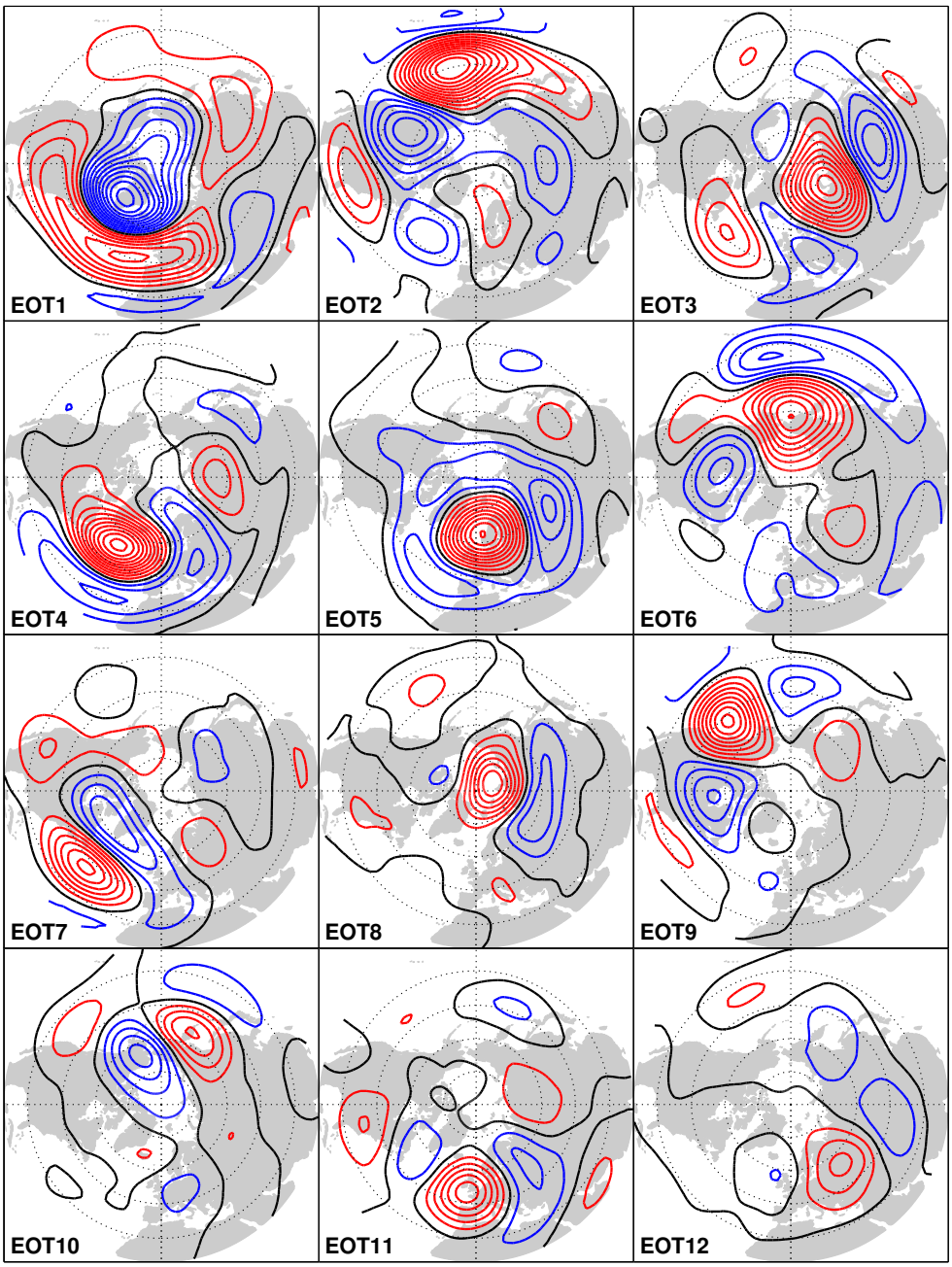

Fig. C.5: 300 hPa geopotential height regressed on the standardized expansion coefficient time series of the first 12 EOTs of NH SLP based on monthly-mean data, Dec. 1958 – Mar. 2008. Contour interval is 10 m per std dev anomaly of the respective EOT time series.

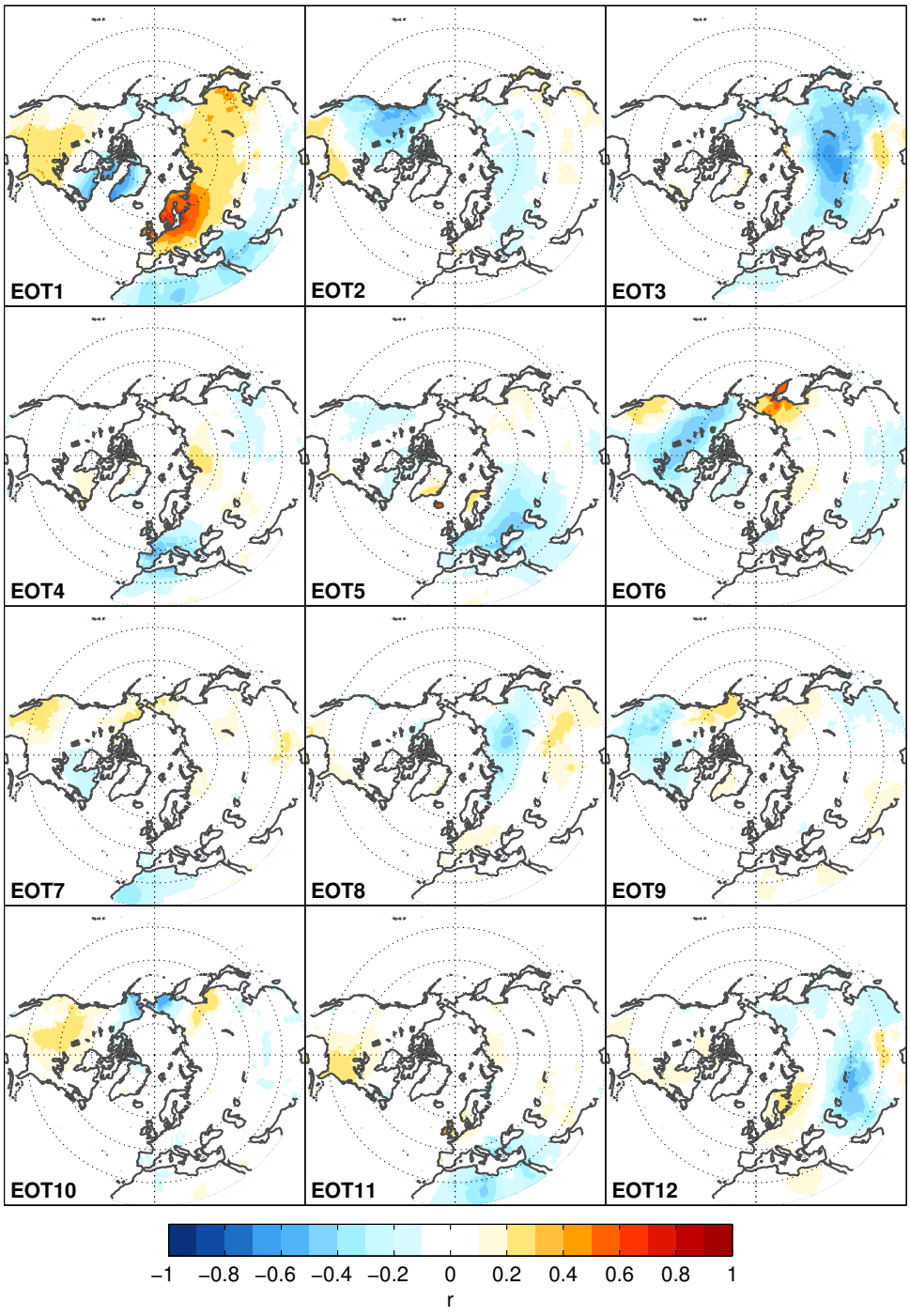

Fig. C.6: Correlation between SAT and the first 12 EOT time series, based on monthly-mean CRU TS 2.1 SAT and EOT analysis of monthly-mean NCEP-NCAR SLP anomalies. Units are correlation coefficient, r.

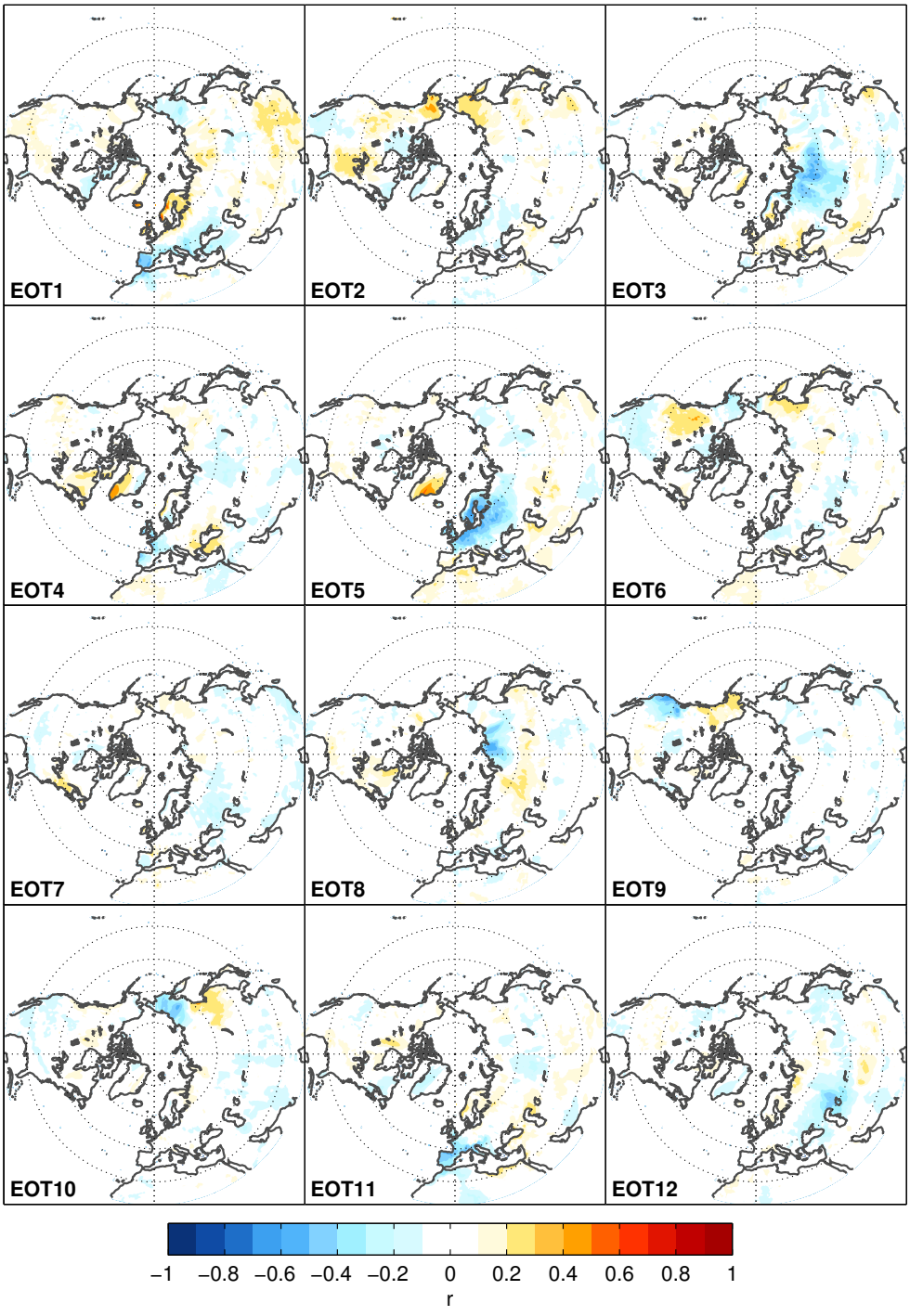

Fig. C.7: Same as C.6, except for monthly-mean precipitation from the CRU TS 2.1 product.